Frequency Stability in Low-Inertia Power Systems

Atinuke Abolaji Ademola-Idowu

A dissertation
submitted in partial fulfillment of the
requirements for the degree of

Doctor of Philosophy

University of Washington

2020

Reading Committee:

Baosen Zhang, Chair

Daniel Kirschen

Brian Johnson

Program Authorized to Offer Degree:

Electrical and Computer Engineering

University of Washington

Abstract

Frequency Stability in Low-Inertia Power Systems

Atinuke Abolaji Ademola-Idowu

Chair of the Supervisory Committee:
Keith and Nancy Rattie Endowed Career Development Professor Baosen Zhang
Electrical and Computer Engineering

The increased penetration of renewable energy resources particularly those connected via inverters to the electric grid like wind and solar, has resulted in the displacement of traditional synchronous generators. This has subsequently led to a decline in the available rotational inertia from these synchronous generators that provides immediate frequency response in the event of a disturbance to the grid. The result is a larger increase in the frequency deviation, rate of change of frequency, and a slower settling time, all of which can lead to frequency instability and an eventual collapse of the grid. This network condition has been termed low-inertia power systems.

The aim of this dissertation is to design control and optimization algorithms that will enable these inverter-based resources participate effectively and optimally in providing frequency control response in a low-inertia power systems by controlling their inverter interfaces.

The first part of this dissertation focuses on optimizing the performance of the popular virtual synchronous machine control structure for inverter-based resources, by developing an algorithm to optimally design the inertia and damping gain coefficient of its frequency control loop. This enables these inverter-based resources to participate efficiently in the inertia

response portion of primary frequency control, by producing active power proportional to frequency measurements, in response to a power imbalance or disturbance to the grid, just like a synchronous generator.

The second part of this dissertation focuses on designing a novel inverter-based resource control strategy termed inverter power control, which is based on model predictive control, to directly determine the optimal active-power set-point for the inverter-based resources in the event of a power imbalance or disturbance in the system. This proposed control framework alleviates a fundamental drawback of the virtual synchronous machine approach that constrains the inverter-based resources to behave like synchronous machines when responding to a frequency event thereby limiting the potentials of these fast acting and flexible inverter-based resources.

TABLE OF CONTENTS

LIST OF FIGURES

Figure Number Page

ACKNOWLEDGMENTS

The process of acquiring my doctoral degree has been a journey made possible by the amazing people in my life and those I have had the privilege of meeting along the way. It has indeed taken a village to get me to this point.

I would like to thank my advisor, Prof. Baosen Zhang, for his guidance all through this process, particularly, his encouragement to be a better researcher and not settle for mediocrity. His keen insight and uncanny ability to solve complex problems were instrumental in shaping the direction of my research.

I want to thank my dissertation committee members, Prof. Daniel Kirschen and Prof. Brian Johnson, for their helpful suggestions during this period as the classes I took under them formed the foundation for my research. I also want to thank the Graduate School Representative, Professor Zelda Zabinsky, whom I was fortunate to have as part of my committee, as well as, my qualifying examination committee members, Prof. Richard Christie and Prof. Linda Bushnell, for their thoughtful notes and discussions. I am also grateful to Prof. Nathan Kutz for his guidance and willingness to devote time to translating a class project, taken under him, to a full-fledged research paper. I also want to thank all the professors that have added to my learning experience and shaped me as an academic all through my time at the University of Washington (UW).

I was fortunate to receive fundings to support my education during this period. Thanks to the Nigerian government for the Presidential Special Scholarship for Innovation and Development fellowship, as I would not have been able to begin this process without their support. I also

want to thank the UW Clean Energy Institute for funding and supporting my research through their fellowship program. I appreciate the help from the administrative staff at the UW Electrical Engineering department, as they were always there to guide me through available funding resources and other opportunities.

During my program, I had the opportunity of doing some internships. Thanks to my Mentors at the National Renewable Energy Laboratory, Andrey Bernstein and Emiliano Dall'Anese, for their support and guidance through the internship process and introducing me to the field of robust optimization. I am also grateful to my mentor at Doosan GridTech, Tess Williams, for teaching me the importance of networking and looking at the big picture of projects, as well as other team members such as Bina Ansari, Troy Negaard, Farshid Shariatzadeh, who made my stay there memorable.

I have also been privileged to work alongside exceptional colleagues. Thanks to Renewable Energy Analysis Lab (REAL) ladies Ahlmahz Negash, Kelly Kozdras, Abeer Almaimouni, Anna Edwards, Yuanyuan Shi, Mareldi Ahumada, Jacqueline Baum, Nina Vincent, Trisha Ray, Pan Li, and Yao Long. It has been great having the support of these ladies not only academically and professionally but also through their friendship. Special thanks to Abeer who has been a dear friend all through this period, from our research collaboration to restaurant sampling, and for constantly encouraging me to be a fast ramping gas generator compared to my usual slow ramping nuclear generator (inside power systems joke). Special thanks also to Yuanyuan whom I started this PhD program with and have prepared for all the milestone examinations together, even to scheduling dissertation writing sessions. I am grateful to Ryan Elliot for the insightful power systems dynamics discussions. Thanks to my other labmates Yury Dvorkin, Chase Dowling, Yize Chen, Daniel Olsen, Hao Wang, Jesus Contreras, Ryan Elliott, Lane Smith, Daniel Tabas, Chanaka Keerthisinghe, Rahul Mallik, Soham Dutta, Minghui Lu, Gord Stephen, Ryan Hay, Kevin Morrissey, Nam Song, for the insightful power systems, controls and optimization conversations as well as lab lunches and other social events; you have all indeed made my stay at UW memorable.

I am thankful to my friends that have supported me and the communities I have been a part of here in Seattle. Thanks to my friends Febisola Akin-Deko, Isaac Nwokocha, Ziad Shehadeh, Victoria Nwobodo, Omoye Uduehi, Segun Modupe, and many more for their support and care. Special thanks to Tola Adeoye, Simone Fobi and Iretiayo Akinola, who have shown me the true meaning of friendship and have been by my side all through the ups and downs of the Ph.D. process, from helping me prepare for milestone examinations to paper reviews and discussions, both academically and personal. I was fortunate to be a part of the UW Graduate Christian Fellowship and Church on the Ave. Thanks to Pastors Ashley Van-Dragt, Geoff Van-Dragt, and Calvin Chen for their warm welcome that has made me feel at home here in Seattle, as well as, the friends I have made here that have helped me grow. I am also grateful to have met Linda and Tom Ackerman who have been like family to me. Special thanks to my small group members, Elizabeth Clark, Emily Ahn, and Ebenezer Gopikrishnan, for the thoughtful discussions and space to explore my faith.

None of this would be possible without my family. To my parents, for their unconditional love and support, prioritizing my education, and encouraging me to pursue my goals. To my siblings Seun, Ademola, and Sola who never fail to make me laugh and put a smile on my face, I could not have asked for better siblings. Also to my cousin Yemisi who has indeed been a big sister to me.

DEDICATION

To my parents

Chapter 1

INTRODUCTION

1.1 Motivation

There has been a significant growth of installed renewable energy sources (RES) in the electric power grid. It is projected that RESs will surpass other forms of electricity generation by 2050, not only in the US [1] but also around the world [3]. The bulk part of this increase is projected to come from solar and wind energy sources, both onshore and offshore, as seen for the US case in Fig. 1.1, where wind and solar are projected to surpass nuclear and coal by 2021 and natural gas by 2045 [1].

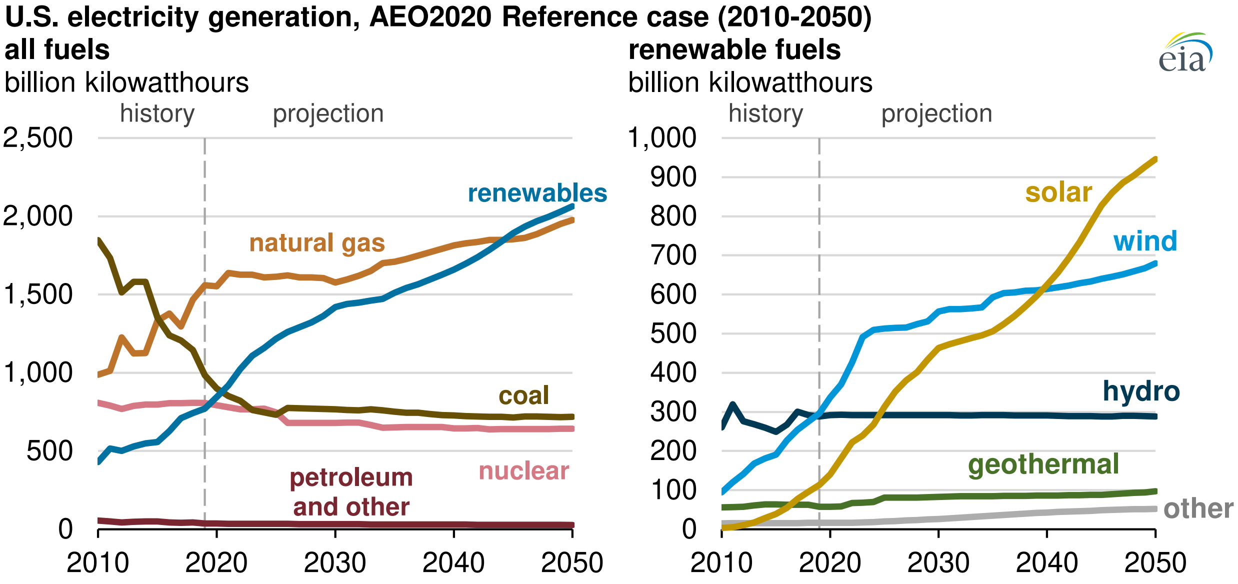

Figure 1.1: Energy outlook 2050 for the United States by EIA [1].

While this development is welcomed from a sustainability perspective, it has undoubtedly introduced some engineering and operational challenges to the running of the electric grid which was designed to have only synchronous machine electricity generation, unidirectional electricity flow and predictable/controllable power output [4, 5]. One of the challenges include difficulties in performing electric market functions and unit commitment due to the variable nature of resources such as wind and solar, that can affect generation scheduling and also impact load forecasting [6, 7]. Another challenge which mostly affects the distribution network is voltage stability, where some buses might experience over-voltage issues due to bi-directional power flow [8, 9]. At the transmission level, the challenge is mostly with frequency stability where both variations in output from wind and solar, and also the lack of physical inertia of these resources results in fluctuations in system frequency and marked frequency decline, which in severe cases could result in a black-out [10].

The majority of RESs are asynchronous in nature and connected to the grid via power electronics devices called inverters or sometimes converters, and can be interconnected to the electric grid through varying configurations [11, 12]. Although the wind RES has a rotating mass and can be either synchronous or asynchronous in nature depending on the turbine type used, it is typically decoupled from the grid due to its wide frequency fluctuations and as such connected via power electronics to the grid [13]. We adopt the term inverter-based resources (IBR) used by the North American Electric Reliability Corporation (NERC) "to represent resources asynchronously connected to the grid and are either completely or partially interfaced with the grid through power electronics" [14]. These IBRs have little to no physical inertia which contributes to frequency stability issues.

Traditionally the first-stage primary frequency control in the electric grid, called the inertial response [15], is provided by conventional generating sources such as coal, nuclear, and gas, which are connected via synchronous machines with huge rotating mass to the grid. In the event of a power imbalance or disturbance to the grid, these machines by virtue of their inertia absorb or release the kinetic energy stored in their rotating masses thereby arresting frequency deviation and reducing the rate of change of frequency (ROCOF). As the grid transitions from a network with dynamics fully governed by synchronous machines to a mixed-source network with dynamics governed by both synchronous machines and IBRs, there will be an accompanying decline in the available rotational inertia system wide [16], leading to larger frequency deviations and faster ROCOFs as shown in Fig.1.2. This network condition has been termed low-inertia power systems [17]. Based on the projected increase in these IBRs and subsequent retirement of synchronous machines, these frequency events are expected to be more pronounced.

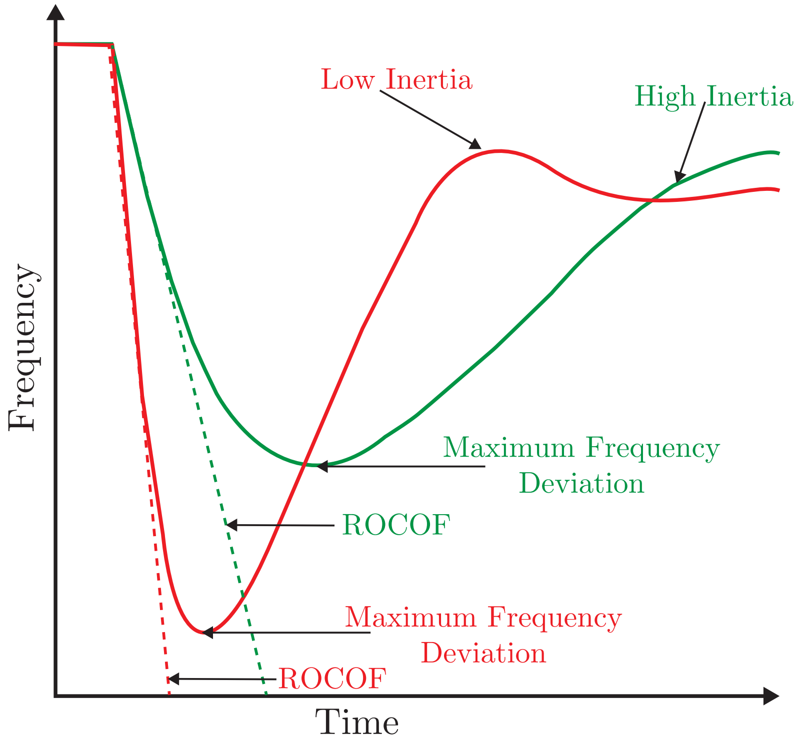

Figure 1.2: Effect of inertia on maximum frequency deviation and ROCOF.

Varying techniques have been proposed in literature and practice to combat this low-inertia issue such as the use of synchronous condensers [18, 19] which provide the physical mass without providing active power, load shedding [20, 21], demand response [22, 23], and more recently, leveraging the fast actuation capabilities of the IBRs (coupled with energy storage systems) in injecting active power into the grid by virtue of the speed of its power electronic circuits. Several control strategies have been proposed based on this later technique and has been a subject of active research (see [17, 24, 25] and the references within). Of the varying control strategies proposed for IBRs, droop control [26–30] and virtual synchronous machines (VSMs) [31–33] are the most popular as they function by mimicking the frequency-power dynamic response of a synchronous machine.

1.2 Contributions

The aim of this dissertation is to design control and optimization algorithms that will enable IBRs to participate effectively and optimally in providing frequency control response in a low-inertia power systems. The contributions of this dissertation will be broadly categorized into two:

- The first part focuses on optimizing the performance of the popular VSM control strategy for IBRs, by developing an algorithm to optimally design the inertia and damping gain coefficients of the VSM. The VSM can then mimic the frequency response behavior of traditional synchronous machines by injecting active power proportional to frequency measurements using these optimized gains, thus enabling the IBR participate efficiently in the inertia response portion of primary frequency control. To achieve this, we first show that minimizing the $\mathcal{H}_2$ norm of the system, which is typically easier to compute, can be used as a proxy to minimizing standard time domain frequency response objective such as maximum frequency deviation or frequency nadir, ROCOF and settling time. We then design this $\mathcal{H}_2$ norm objective function to explicitly trade-off between competing objectives such as maximum frequency deviation and settling time through the use of a regularization term. Specifically, we formulate the design problem as a constrained and regularized $\mathcal{H}_2$ norm minimization problem, and develop an efficient gradient algorithm for this non-convex problem.

- The second part of this dissertation focuses on designing a novel IBR control strategy based on model predictive control, to directly determine the optimal active-power set-point for the IBRs in the event of a power imbalance or disturbance in the system. This proposed control framework alleviates a fundamental drawback of the VSM approach that constrains the IBRs to behave like synchronous machines when responding to a frequency event which results in limiting the potentials of the fast acting and flexible IBRs. Also, in contrast to existing IBR control methods, this proposed control strategy explicitly takes the hard constraints in power and energy into account. To achieve this:

- We first focus on developing the novel control framework which we call Inverter Power Control (IPC) in a network with a single IBR, where we assume all IBRs can be aggregated into one. We reformulate the system dynamics typically governed by the swing equation to a modified form with the inverter control angle as the input, such that we can utilize model predictive control to determine the optimal active-power set-point using the inverter angle as control variable. We also integrate an observer to estimate the states and disturbance in the system which arises due to power imbalance, model mismatches, noise and limited communication, thereby making the controller robust.

- With the control framework setup in-place, we further extend the capabilities of this IPC, including its ability to handle hard constraints, to a multiple IBR system which we call Multi-IPC (MIPC). Under this MIPC control framework, we relax the assumption of having only a single IBR to having multiple IBRs connected at different nodes across the network. We also extend the controller's configuration such that it can function under a centralized and a distributed control scenario. Under the centralized control, a single MIPC central node coordinate and control the IBRs in the network to provide the fast frequency response while under the distributed control structure, each IBR runs the MIPC and utilizes state information from neighboring generators, by leveraging on an observer to estimate the unmeasured states and disturbances.

1.3 Dissertation Outline

The remaining chapters of this dissertation are organized as follows:

- Chapter 2: **Review of Frequency Control in Power Systems** gives more details into the concept of low-inertia, its impact on frequency stability, previously proposed methods in literature to combat this problems and other foundational concepts relied on to solve this problem.
- Chapter 3: **Optimal Design of Virtual Inertia and Damping Gain Coefficients** focuses on developing an efficient algorithm to optimally select the virtual inertia and damping gain coefficients, and to compute the gradient for this non-convex problem.
- Chapter 4: **Inverter Power Control in Low-Inertia Power Systems** develops the mathematical framework for the proposed novel inverter power controller and benchmarking its performance to an optimally tuned VSM approach.
- Chapter 5: **Multi-Inverter Power Control in Low-Inertia Power Systems** extends the functionality of the IPC designed in the previous chapter to cater to a multiple IBR scenario and a distributed control structure.
- Chapter 6: **Conclusion and Future Works** summarizes the key take-aways of this dissertation and potential extensions of the research work.

Chapter 2

REVIEW OF FREQUENCY CONTROL IN POWER SYSTEMS

2.1 Frequency Stability in Power Systems

Frequency stability in a power systems network is the ability of the system to maintain the grid frequency within an acceptable range as defined by system's operation guidelines [34]. This is to ensure the operational security of the power systems as frequency deviation outside the pre-specified range can lead to the triggering of protective devices such as the under- and over- frequency load shedding devices which can results in cascading failures and potentially a system wide blackout [15]. Large deviations in frequency occurs as a result of either the loss of a huge generator or load, or a transmission line fault connecting a major load area, ultimately resulting in an imbalance between the power generated and the power demanded.

In its most basic form, the frequency dynamics of an electric grid is governed by [35]:

$$\frac{df_{\text{grid}}}{dt} = \frac{P_{\text{generated}} - P_{\text{demand}}}{M_{\text{T}}} = \frac{\triangle P}{M_{\text{T}}} \tag{2.1}$$

where f_{grid} is the effective synchronous frequency of the network, $\frac{df_{\text{grid}}}{dt}$ is the rate of change of frequency (ROCOF) and M_T is the total inertia constant of the network. This total inertia constant M_T is obtained by summing up the normalized inertia coefficient of each generator that has a physical rotating mass in the system. From (2.1), it can be observed that the ROCOF and therefore the grid frequency f_{grid} depends on the difference between the power generated and demanded, denoted as $\triangle P$, and the magnitude of M_{T}. In the event of a disturbance to the network, each rotating mass either releases its stored kinetic energy or absorbs excess energy from the network in a bid to stop the frequency decline or incline. In relation to (2.1), the objective of frequency control during a disturbance is to minimize the maximum frequency deviation Δf_{grid} and slow down the ROCOF $\frac{df_{grid}}{dt}$ as shown in the negative power imbalance example of Fig. 2.1.

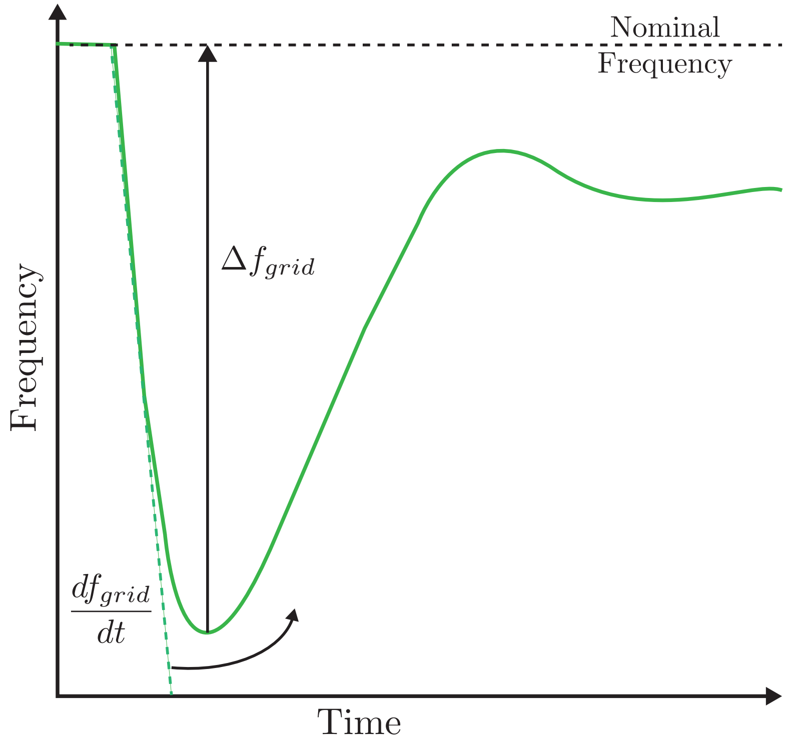

Figure 2.1: Frequency deviation and ROCOF in the event of a negative power imbalance disturbance to the grid.

2.2 Low inertia Power Systems

With the continuous integration of more renewable energy sources (RESs) particularly those connected via power electronics to the grid such as wind and solar, more and more traditional synchronous machines like coal and nuclear are being retired. This also translates to a decrease in the total inertia in the system ($< M_{\mathrm{T}}$) in (2.1), resulting in a faster ROCOF and larger frequency deviation in the event of a power imbalance. With the projected steady increase in RES [1, 3], this concept which has been termed low-inertia power systems that was once considered a theoretical issue is gradually becoming prominent and has begun to manifest in some places around the world. In South Australia, a frequency collapse occurred on September 28th, 2016 [10] and investigations into the cause showed that during a disturbance to the system due to severe weather conditions, there was also reduction in wind output and not enough reserve to pick up the slacks. This has led to various grid operators, such as Texas grid [36], Irish grid [37], Australian grid [38] and Nordic grid [39], developing road maps for dealing with low-inertia issues.

Several approaches have been proposed to mitigate this issues and some of them are reviewed in the following subsections.

2.2.1 Synchronous Condenser

Synchronous condensers are essentially rotating synchronous machines without a prime mover, that is, connected to the grid but not supplying active power. Since it is a rotating machine, it has the physical inertia needed and can therefore participate in the inertia portion of primary frequency control by releasing or absorbing kinetic energy [18]. In relation to (2.1), integrating more synchronous condensers to the grid helps to increase the magnitude of M_{T}. The use of synchronous condensers in the grid is not new concept as it has been used for reactive power compensation and voltage control in the past [40]. The emergence of power electronics devices such as Static VAr Compensators (SVCs) [41] and STATCOMs [42] which are cheaper, faster and require less maintenance have since replaced the synchronous condensers. Several research works in [18, 19, 43–45] have shown the advantages of utilizing synchronous condensers to mitigate low-inertia issues while grid operators in countries like Australia [46], and Denmark [19] have included using synchronous condensers as part of their strategy for improving frequency response in the future grid. While this approach shows a lot of potentials, it still maintains the same drawback such as being expensive to run, as it does not produce active power but has to be left spinning, and other strategies which cost less have shown promises in solving the low-inertia issues [44].

2.2.2 Demand Response and Load Shedding

Another potential way of reducing the magnitude of $\triangle P$ in (2.1) is to reduce or increase the power demanded P_{demand} by implementing some demand response scheme or a pre-specified load shedding schedule.

Demand response involves utilizing self-regulating loads such as air conditioners, water heaters, refrigerators and electric vehicles that can be controlled using a thermostat [47]. The initial consideration for demand response was to delay or avoid building new transmission lines and scheduling generators to cater to peak load demand by load shifting [48]. With the possibility of having autonomous demand response which responds to system signals such as frequency rather than price signals [49], the prospects of using it in low-inertia situations is promising according to research works [22,50] and is among the methods being considered in Britain [23,51].

Load shedding on the other hand involves disconnecting a portion of the total load in some systemic order to maintain balance with the philosophy that it is better to disconnect in a controlled manner than to allow cascaded failure [21]. This method is typically considered as a last resort against frequency collapse and some research works have proposed intelligent ways of achieving this systemic load shedding such as adaptively activating the under-/over-load frequency shedding relays using some combinatorial algorithms [52] or utilizing wide area measurements to trigger these relays [53]. This has led to load shedding being considered in mitigating low-inertia issues [54–56].

Major drawbacks of the demand response approach are the communication infrastructure required and the feasibility of coordinating the varying resources which could be a lot especially when considering thermostatically controlled residential devices [57]. For load shedding, the drawback is that loads considered low-priority will be the first to get disconnected from the network thus rendering some parts of the control area without power.

2.3 Frequency Control using Inverter-Based Resources (IBR)

Recent research efforts on mitigating the low-inertia issue has been centered mostly on utilizing the RESs and energy storage systems, especially those connected to the grid via power electronics termed inverter-based Sources (IBR), to provide fast frequency response [34, 58]. This can be achieved by injecting or absorbing active power based on some function of the grid frequency. In relation to (2.1), this approach reduces the magnitude of $\triangle P$ by increasing or decreasing $P_{\text{generated}}$.

IBRs can be interconnected with other IBRs and small scale generators to form a network commonly known as microgrids. These can either function in an island mode (in either ac or dc configuration) or can be integrated to the main electric grid (in ac configuration) consisting of synchronous machines [12]. The interconnection of this microgrid to the electric grid also depends on their mode of operation and can be classified as grid following, grid forming or grid supporting inverters [12,59]. In the grid following mode, the IBRs operate as an active and reactive power source with its frequency and voltage magnitude determined by its interconnection with the grid that can enable it function in parallel to other inverters and generators. In the grid forming mode, the IBRs operates as a voltage source that directly controls its frequency and voltage magnitude while its active and reactive power output is determined by its interconnection with the grid. The grid supporting mode combines the attributes of the grid following and grid forming configurations thus making its operations similar to a synchronous generator. It achieves this by using the droop control or other control structures to implement a relationship between frequency and active power, and voltage and reactive power.

Adopting the grid-supporting configuration, from the network point of view, the grid-connected IBRs is seen as producing a constant power according to a set reference point and maintained by internal control loops such that it remains synchronized to the grid. For system analysis, the inverter can be modeled as a voltage source behind a reactance, much like a synchronous machine [60]. The difference is that while the internal emf angle is the electrical equivalent of the rotor angle [15], the internal voltage angle in the inverter model is set by the internal closed loop control based on the active-power set-point [61]. Some control strategies either change the modulation index directly or change the active power set-point. The former case is mostly used in microgrid systems consisting of only IBRs while the later case is mostly used in mixed source network and is the configuration adopted in this dissertation because it does not require modifications to the normal operations of the inverter.

In the event of a power imbalance in the network reflected by a frequency deviation, an IBR does not have a "natural" response to frequency deviation as synchronous machines does since they are made of power electronics components and have no rotating mass [11]. Therefore, an additional control loop, preferably one that does not alter the normal inverter operation, is needed to enable the IBRs participate in frequency control by changing its power set-point based on frequency measurements [62]. This is possible because the control responses of an inverter are digital and can thus be programmed with various functions within the limit of the inverter's capacity [12].

The two most popular frequency control strategy for IBRs are *droop control* and *virtual inertia control* reviewed below:

2.3.1 Droop Control

This control strategy is similar to the speed droop control in synchronous machines and implements a linear proportional relationship between the frequency deviation and the active-power output of the IBR [15, 59]. This additional layer of control runs on each IBR thus allowing them to run autonomously as they rely only on local frequency measurements as measured by the phase locked loop (PLL) [63, 64]. The droop control is governed by the equation $\omega = \omega^0 - k(P - P^0)$ where ω^0 is the nominal/reference frequency, P is the active power output of the IBR, P^0 is the IBRs reference active power and k is the proportional droop constant [65]. This droop control configuration can also be used in voltage control by implementing a proportional control between voltage and reactive power [66]. Research works in [29, 30, 67] advocate instead for a droop between the angle and power such that $\delta = \delta^0 - k(P - P^0)$ with results showing that this droop type leads to increased stability, smaller frequency deviations and faster dynamic response. This droop constant can be optimized over and has been a subject of much research [68–70].

The drawback of the droop control is that droop based systems tend to have slow transient responses, active power regulation and no inertia control response [33, 71].

2.3.2 Virtual Inertia Control

This control strategy act as a second order oscillator to provide inertia and damping to the grid and are broadly categorized as virtual synchronous machines (VSM) as they essentially emulates the inertia control of a conventional synchronous machine [72,73]. There are various topological configuration of this VSM [24] such as the synchroconverter which tries to mimic the behavior of an actual synchronous machine by running the full dynamics [74], the swing-equation based topology which uses the swing equation to determine the inertia emulation [32, 75] and the frequency-power response topology which produces power proportional to frequency measurements using inertia and damping gain coefficients [33, 76]. The latter topology is the most popular and will be adopted in this dissertation. Research works in [28, 44] show that the VSM control strategy performs better than the droop control due to the added inertia component and [77] shows conditions under which the VSM and droop are equivalent. Detailed analysis of the VSM configurations can be found in [25, 33, 78] and the references contained. The inertia and damping gain coefficients used in the VSM control strategy can be optimized using a number of techniques [2, 79, 80]. One of the drawback of the VSM approach as highlighted in [17, 62] is the constraining of IBRs to respond like a second oscillator in line with the behavior of synchronous machines. This results in a limited degree of freedom which limits the performance resulting in a trade-off between the frequency deviation and ROCOF, and the settling time. To mitigate this drawback, works in [81–83] have proposed an adaptive approach that changes the parameter based on the measured frequency deviation and ROCOF values. However, it is difficult to find an optimal rule to update these parameters in real-time.

2.4 *Wide Area Measurements in Frequency Control*

As described above, the droop and VSM control typically rely on the local frequency measurement obtained by using PLLs. While the use of local measurement is advantageous in terms of not requiring any communication infrastructure, it does pose some challenges to achieving proper control in the network. One of the challenges is that, local measurements do not give a true picture of the network states, that is, it is not situation aware [84,85]. It is possible for a local measurement to show a moderate frequency deviation in part of the network while the actual situation might be two or more areas swinging widely against each other in a scenario known as inter-area oscillations [86]. The use of this measurements therefore prevents the controllers from taking optimal and coordinated actions with other controllers. It has been shown in several research works that the use of local signals in devices like power system stabilizers (PSS) [85,87], flexible AC trans-mission systems (FACTS) [88,89] and even static var compensators (SVC) [90] result in undamped inter-area oscillations which can lead to instabilities in the network. This has led to some research works in [84,91] advocating for the use of global measurements sometimes in conjunction with local measurements to achieve desirable control actions. These global measurements are more generally known as wide area measurements (WAMS) and can be obtained from supervisory control and data acquisition (SCADA) or phasor measurement unit (PMU) measurements.

SCADA measurements are state estimates of the system states, such as bus voltage magnitude and angles, transmitted every 2-4 seconds, assuming the system is in quasi-steady state [92, 93]. Due to this slow sampling rate alongside its asynchronous transmission, it is unable to provide to provide transient dynamic details of the network. It is therefore suitable for steady state analysis after-the-fact and not suitable for real time protection and control. PMU measurements on the other hand are more suitable real-time control, operations and protections as they are real-time measurements of system states with about 30-60 samples per seconds, time-synchronized geographically (using a GPS receiver) [92, 94, 95]. The measurements typically obtainable from PMUs are the positive sequence real-time line current magnitude and phase, and real-time bus voltage magnitude and phase, from which frequency and rate of change of frequency can be calculated. In some upgraded versions of PMU, it is possible to obtain these measurements from the individual phases [96].

In order to use these PMU measurements for control applications, especially frequency control, estimating the rotor angle and speed is required. While most research works, for example in [97–99], implicitly assume the availability of these states, they in reality cannot be obtained directly and estimating them has been a subject of various research.

2.4.1 Rotor Angle Estimation

Research works into estimating the rotor angle of synchronous machines from PMU data can be broadly categorized into two: analytical computations based on using mathematical properties of the machine and network, and using artificial neural networks. Under the analytical category, [100] proposed computing the rotor angle from stator reactances obtained from the observed damper currents, known machine parameters, and PMU measurements. Similarly, [101] proposes computing the rotor angle purely from terminal PMU measurements by exploiting the structure of the flux linkage equations to obtain approximate formulas for the rotor angle. In [102], a sliding mode approach was used to reconstruct the rotor angle and quadratic-axis transient voltage from frequency measurements from PMUs with the model taking into account the transient voltage dynamics and insensitive to bounded uncertainties affecting the dynamics of the synchronous generator. Research work in [103] proposes a new estimation method using nonlinear extended recursive three-step smoother to estimate the states and the unknown inputs, such as rotor angle, field voltage, speed and mechanical power input, of the synchronous machine using data potentially from PMUs. Under the neural network category, [104] proposes the use of two neural networks trained on voltage and current phasors date obtained from PMU to estimate the cos and sin of the rotor angle after which the actual rotor angle can be recovered by simple post-processing.

2.4.2 Rotor Speed Estimation

Estimating the speed or frequency from PMU is more straightforward from the frequency measurements of the PMU. In [105, 106], the use of Kalman filter for dynamic state estimation, consisting of both rotor angle and speed, in a multi-machine system using PMU data with both small and large disturbances was explored. Extensions to this dynamic state estimation using varying filters was also carried out in [107, 108] using extended Kalman filter, in [109, 110] using unscented Kalman filter and [111] using extended particle filter. Estimation of rotor speed only using PMU data was carried out in [112] using a linear and model-independent rotor-speed estimation problem based on a concept of the frequency divider formula.

2.5 Conclusion

Going forward in this dissertation, we leverage on the knowledge gained from these reviewed techniques to design efficient control algorithms for the inverter interfaces through which RESs and energy storage systems can be integrated to the electric grid such that the drawback of integrating these IBRs to the grid due to its lack of physical inertia can be mitigated.

Chapter 3

OPTIMAL DESIGN OF VIRTUAL INERTIA AND DAMPING GAIN COEFFICIENTS

3.1 Introduction

3.1.1 Motivation

In a traditional electric power system network with only conventional generators, the rotating synchronous machines connected to the network possesses kinetic energy as a result of their rotating mass and releases it as an immediate response in the event of a power imbalance to reduce the rate of frequency decline [15]. As the electric power grid transitions from this traditional state to a mix of conventional generators and inverter-based renewable energy resources (IBRs), this immediate response capability by the synchronous machine is reduced. This results in an increased rate of change of frequency (ROCOF) and consequently, a higher frequency deviation which results in a low frequency nadir, that is, the maximum frequency deviation [113]. The ROCOF, frequency nadir and settling time/frequency are important frequency response metrics in the power systems network.

3.1.2 Literature Review

To combat this problem, various techniques that utilize IBRs and energy storage systems (ESS) have been proposed. One of such techniques is called De-loading. This provides a reserve margin in the wind turbine or Photo-voltaic (PV) by operating on a reduced power level as compared to its maximum power extraction point [25]. Other techniques include designing the inverter to behave like a synchronous generator as in the case of a synchroconverter [24,114], using a swing equation based approach that computes the swing equation every control cycle to emulate inertia [32,75] or emulating the inertia by monitoring the ROCOF and frequency deviation, and producing power proportional to that change as in the case of the VSM [24]. In the later case, for a variable speed wind turbine such as a doubly fed induction generator, a suitable controller can be used to release the kinetic energy stored in the rotating blades based on the ROCOF and frequency deviation [25, 115]. A similar controller can be used for an ESS with the difference being the source of the energy.

The components of interest in the design the controller for the VSM is the gain blocks mimicking the inertia and damping coefficients values. There is a need for these values to be optimally selected depending on the current system operating conditions and the units committed to enable the inverters efficiently participate in the inertia response. A variant of this problem was considered in [80] and [2] where the focus was instead on the placement of the virtual inertia though the same reasoning applies to the problem being considered. The difference is that in [80] the optimal virtual inertia and damping placement was computed with explicit time-domain constraints on the frequency response metrics, while in [2], the optimal virtual inertia placement was considered using the $\mathcal{H}_2$ norm as performance metrics to measure the network coherency. The shortcomings of the first approach is its approximations as it is difficult to explicitly define the time-domain requirements and computational burden, while the second approach does not optimize over the damping coefficient, utilizes a more involved gradient derivation process and does not providing a means of trading-off between competing system objectives. We improve on this later shortcoming by augmenting the $\mathcal{H}_2$ norm objective with a tuning parameter that gives control over the frequency performance metrics and can be adjusted to determine the inertia and damping coefficient values for any frequency performance requirements we deem more important.

3.1.3 Contributions

The contributions of this chapter are as follows:

- We provide a systematic and efficient way of optimally designing the virtual inertia and damping coefficient of a VSM that emulates the inertia response of a synchronous machine based on the ROCOF and frequency deviation.

- We show that the $\mathcal{H}_2$ norm problem can be used as a proxy to capture the important frequency response metrics by minimizing the control effort required to provide the frequency response.
- We derive a tuning parameter to augment the $\mathcal{H}_2$ norm problem thereby giving us control over how much of the requirements we want to satisfy as the $\mathcal{H}_2$ norm performance metric cannot by itself simultaneously satisfy the essential time domain frequency performance requirements: slow ROCOF, small frequency nadir and fast settling time.
- We also derive an explicit computationally efficient gradient for the non-convex gain optimization problem.

The proposed method is validated on a test system with the simulation result in time domain showing that the defined objective and the expected trade-off is satisfied.

The remaining section are organized as follows: Section 3.2 summarizes the modeling of the electric power systems and the VSM. Section 3.3 describes the frequency response requirements in the power systems and objective functions that can quantify these requirements. Section 3.4 presents the optimization problem and the proposed gradient for the computation. Section 3.5 shows the application of the algorithm to a test case.

3.2 Modeling

3.2.1 Power System Model

In a power systems network, the electromechanical dynamics of a synchronous generator is governed by the swing equation [15]:

$$\begin{aligned} \frac{d\delta_i}{dt} &= \triangle\omega_i \\ m_i \frac{d\triangle\omega_i}{dt} + D_i \frac{d\delta_i}{dt} &= P_{m,i} - P_{e,i}, \quad \forall i \in \{1, \cdots, n\}. \end{aligned} \tag{3.1}$$

where δ_i is the rotor angle of the i^{th} generator, $\triangle\omega_i$ is the rotor speed deviation of the i^{th} generator, m_i is the i^{th} generator inertia constant, d_i is the i^{th} generator damping coefficient,

$P_{m,i}$ is the mechanical input power of the i^{th} generator, $P_{e,i}$ is the electric power output from the i^{th} generator and n is the number of generators.

The swing equation in (3.1) can be linearized around an operating point to obtain a model suitable for analyzing the response of the generators when subjected to disturbances. This model can be represented in first order state space form as in (3.2):

$$\begin{bmatrix} \triangle\dot{\boldsymbol{\delta}} \\ \triangle\dot{\boldsymbol{\omega}} \end{bmatrix} = \underbrace{\begin{bmatrix} \mathbf{0} & \boldsymbol{I} \\ -\boldsymbol{M^{-1}L} & -\boldsymbol{M^{-1}D} \end{bmatrix}}_{\boldsymbol{A}} \begin{bmatrix} \triangle\boldsymbol{\delta} \\ \triangle\boldsymbol{\omega} \end{bmatrix} + \underbrace{\begin{bmatrix} \mathbf{0} \\ \boldsymbol{M^{-1}} \end{bmatrix}}_{\boldsymbol{B}} \triangle\boldsymbol{P} \tag{3.2}$$

where $\boldsymbol{M} = \text{diag}(\boldsymbol{m_i})$ and $\boldsymbol{D} = \text{diag}(\boldsymbol{d}_i)$. $\triangle\boldsymbol{P}$ represents an imbalance between the mechanical and electrical power. Under assumptions constant impedance load and DC power flow, $\triangle\boldsymbol{P_i}$ can be simplified to:

$$\triangle\boldsymbol{P_i} = \sum_{j\neq n} \boldsymbol{L_{ij}}(\triangle\boldsymbol{\delta_i} - \triangle\boldsymbol{\delta_r}) = \sum_{j\neq n} \boldsymbol{L_{ij}} \triangle \boldsymbol{\delta_{ir}} \tag{3.3}$$

where $\triangle\boldsymbol{\delta_r}$ is the reference angle which is the angle of designated swing generator. For ease of notation, we drop the subscript r and use $\triangle\boldsymbol{\delta_i}$ to represent the relative angle. Under the assumptions made, $\boldsymbol{L}$ is the network susceptance matrix (shunt admittance ignored) given by $\boldsymbol{L_{ii}} = \sum_{i\neq j} b_{ij}$ and $\boldsymbol{L_{ij}} = -b_{ij}$.

3.2.2 Virtual Synchronous Machines (VSM)

As discussed earlier, the main idea behind a VSM, is to emulate the inertia response by controlling the inverter to respond to changes in frequency [24]. A review of this technique can be found in [31, 32, 116]. The change in output power produced by the inverter in response to the frequency change functions as described in Fig.3.1 and is governed by $\triangle\boldsymbol{P} = \tilde{\boldsymbol{m}} \triangle \dot{\boldsymbol{\omega}} + \tilde{\boldsymbol{d}} \triangle \boldsymbol{\omega}$, where $\tilde{\boldsymbol{m}}$ and $\tilde{\boldsymbol{d}}$ are the virtual inertia and damping gain coefficients. The choice of these values determine how efficiently the inverter responds and should therefore be optimally selected to achieve the frequency response performance metrics specified by the operators.

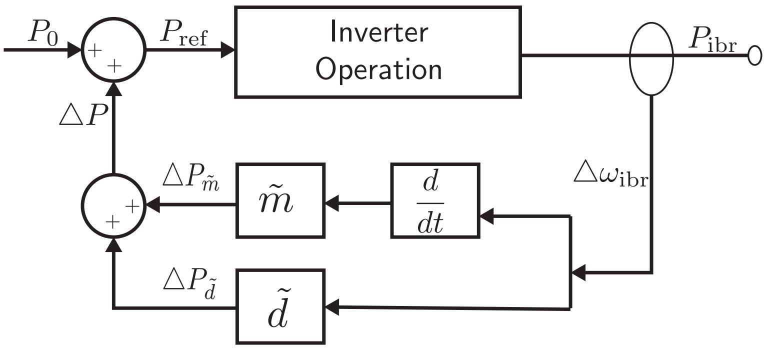

Figure 3.1: Block Diagram of the frequency control loop of a VSM which utilizes frequency deviation and ROCOF measurement to produce active power for inertia emulation.

3.3 Performance Metrics

When an event occurs in a power system network, frequency stability is maintained through the primary, secondary and tertiary frequency controls. The automatic inertia response which releases the rotational kinetic energy in the machines and the proposed virtual inertia response falls under the primary control and occurs in the first few seconds (∼10s) of an event [34]. In a power systems network, the major frequency performance metrics evaluated to determine the sufficiency of the available frequency controls are the ROCOF, frequency nadir and settling time/frequency [34]. It is desired to have a slow ROCOF, low frequency nadir and fast settling time/frequency. To quantify these, we consider the rotating kinetic energy produced by the generators during an event, this can be represented as the quadratic function $\boldsymbol{z} = \boldsymbol{\frac{1}{2}} \triangle \dot{\boldsymbol{\omega}}^{\boldsymbol{T}} \boldsymbol{M} \triangle \dot{\boldsymbol{\omega}}$ and in matrix form as in equation (3.4):

$$\boldsymbol{z} = \underbrace{\begin{bmatrix} \boldsymbol{0_n} & \boldsymbol{M}^{\boldsymbol{\frac{1}{2}}} \end{bmatrix}}_{\boldsymbol{C}} \begin{bmatrix} \triangle\boldsymbol{\delta} \\ \triangle\boldsymbol{\omega} \end{bmatrix} \tag{3.4}$$

We want to minimize this energy released in the event of a disturbance while ensuring that the system is stable. This can be used as a performance metric when trying to emulate this behavior in an IBR with VSM controller. A minimized energy requirement connotes a reduced area under the frequency curve. A suitable and well developed control performance metrics that captures this objective is the $\mathcal{H}_2$ norm (commonly interpreted as the impulse-to-energy gain) [2] [117]. Depending on the system structure, the system objectives might be competing as in our case. For example, consider a second order mechanical system (mass-spring-damper system), for a given damping value, a lower mass results in a higher overshoot but faster settling time while a higher mass results in a smaller overshoot but a slower settling time.

To provide a means of trading-off between these competing system objectives or explicitly controlling the frequency performance requirements, consider the swing equation in (3.1), which can be re-written to obtain the ROCOF (and by extension, the maximum frequency deviation) as:

$$\frac{d \triangle \omega_i}{dt} = \frac{1}{m_i}(\triangle P_i - d_i \triangle \omega_i). \tag{3.5}$$

If our goal is to slow down or minimize the ROCOF ($\frac{d\triangle\omega_i}{dt}$) in (3.5), then we maximize m_i such that it is larger than $(\triangle P_i - d_i \triangle \omega_i)$. Conversely, if in a certain scenario a faster settling time is required, that is a higher frequency due to inverse proportionality, then as explained earlier for a second order system where $m_i \propto \frac{1}{\omega_i^2}$, m_i has to be minimized in order to maximize ω_i, thereby minimizing $\triangle\omega_i$. Since these two requirements depend on m in opposite ways, the tuning control is therefore set as $\beta\|\boldsymbol{m}\|_2^2$ where the sign of β varies depending on which of the objectives we intend to satisfy the most.

3.4 Problem Formulation

3.4.1 Optimization Problem

The total objective function will be a combination of the two objective described in section 3.3. The first is the $\mathcal{H}_2$ norm which seeks to strike a balance between two competing objectives: minimizing frequency nadir and ROCOF, and minimizing the settling time, while the second represented by $\beta\|\tilde{\boldsymbol{m}}\|_2^2$ gives preference on the control over these competing objective. The design variables $\tilde{\mathbf{m}}$ and $\tilde{\mathbf{d}}$ are components of the matrix $\boldsymbol{A}, \boldsymbol{B}$ and $\boldsymbol{C}$ in (3.2) and

(3.4) as they are meant to mimic the frequency response behavior of synchronous machines. The $\mathcal{H}_2$ norm of a linear system with impulse response $\boldsymbol{G}(t) = \boldsymbol{C}e^{\boldsymbol{A}t}\boldsymbol{B} + \boldsymbol{D}$ is computed using [118]:

$$\begin{aligned} \|\boldsymbol{G}\|^2_{\mathcal{H}_2} &= \mathrm{Tr}\left[\int_0^{+\infty} \boldsymbol{G}(t)^T \boldsymbol{G}(t) dt\right] = \mathrm{Tr}\left[\boldsymbol{B}^{\boldsymbol{T}}\boldsymbol{Q}\boldsymbol{B}\right] \\ \|\boldsymbol{G}\|^2_{\mathcal{H}_2} &= \mathrm{Tr}\left[\int_0^{+\infty} \boldsymbol{G}(t) \boldsymbol{G}(t)^T dt\right] = \mathrm{Tr}\left[\boldsymbol{C}\boldsymbol{P}\boldsymbol{C}^{\boldsymbol{T}}\right] \end{aligned} \tag{3.6}$$

such that the $\mathcal{H}_2$ norm objective of the system with a mix of synchronous machines and IBRs running the VSM controller becomes:

$$\boldsymbol{J} = \|\boldsymbol{G}\|^2_2 = \mathrm{Tr}(\boldsymbol{C}(\tilde{\boldsymbol{m}})\boldsymbol{P}\boldsymbol{C}(\tilde{\boldsymbol{m}})^{\boldsymbol{T}}) \tag{3.7a}$$

$$\boldsymbol{J} = \|\boldsymbol{G}\|^2_2 = \mathrm{Tr}(\boldsymbol{B}(\tilde{\boldsymbol{m}})^{\boldsymbol{T}}\boldsymbol{Q}\boldsymbol{B}(\tilde{\boldsymbol{m}})) \tag{3.7b}$$

where $\boldsymbol{P}$ and $\boldsymbol{Q}$ are the observability and controllability gramian and satisfy the Lyapunov equation in (3.8a) and its dual in (3.8b) respectively.

$$\boldsymbol{A}(\tilde{\boldsymbol{m}}, \tilde{\boldsymbol{d}})\boldsymbol{P} + \boldsymbol{P}\boldsymbol{A}(\tilde{\boldsymbol{m}}, \tilde{\boldsymbol{d}})^{\boldsymbol{T}} + \boldsymbol{B}(\tilde{\boldsymbol{m}})\boldsymbol{B}(\tilde{\boldsymbol{m}})^{\boldsymbol{T}} = \mathbf{0} \tag{3.8a}$$

$$\boldsymbol{A}(\tilde{\boldsymbol{m}}, \tilde{\boldsymbol{d}})^{\boldsymbol{T}}\boldsymbol{Q} + \boldsymbol{Q}\boldsymbol{A}(\tilde{\boldsymbol{m}}, \tilde{\boldsymbol{d}}) + \boldsymbol{C}(\tilde{\boldsymbol{m}})^{\boldsymbol{T}}\boldsymbol{C}(\tilde{\boldsymbol{m}}) = \mathbf{0} \tag{3.8b}$$

The optimization problem can then be formulated as:

$$\begin{aligned} \underset{\tilde{\mathbf{m}},\tilde{\mathbf{d}}}{\text{minimize}} \quad & J_T(\tilde{\mathbf{m}}, \tilde{\mathbf{d}}) = \left\|\boldsymbol{G}(\tilde{\boldsymbol{m}}, \tilde{\boldsymbol{d}})\right\|^2_2 + \beta\|\tilde{\boldsymbol{m}}\|^2_2 && \text{(3.9a)} \\ \text{subject to} \quad & \underline{\tilde{\mathbf{m}}} \leq \tilde{\mathbf{m}} \leq \overline{\tilde{\mathbf{m}}} && \text{(3.9b)} \\ & \underline{\tilde{\mathbf{d}}} \leq \tilde{\mathbf{d}} \leq \overline{\tilde{\mathbf{d}}} && \text{(3.9c)} \\ & \boldsymbol{A}(\tilde{\boldsymbol{m}}, \tilde{\boldsymbol{d}})\boldsymbol{P} + \boldsymbol{P}\boldsymbol{A}(\tilde{\boldsymbol{m}}, \tilde{\boldsymbol{d}})^{\boldsymbol{T}} + \boldsymbol{B}(\tilde{\boldsymbol{m}})\boldsymbol{B}(\tilde{\boldsymbol{m}})^{\boldsymbol{T}} = \mathbf{0} && \text{(3.9d)} \\ & \boldsymbol{A}^{\boldsymbol{T}}(\tilde{\boldsymbol{m}}, \tilde{\boldsymbol{d}})\boldsymbol{Q} + \boldsymbol{Q}\boldsymbol{A}(\tilde{\boldsymbol{m}}, \tilde{\boldsymbol{d}})^{\boldsymbol{T}} + \boldsymbol{C}(\tilde{\boldsymbol{m}})^{\boldsymbol{T}}\boldsymbol{C}(\tilde{\boldsymbol{m}}) = \mathbf{0} && \text{(3.9e)} \\ & \boldsymbol{P} \succ \mathbf{0}; \quad \boldsymbol{Q} \succ \mathbf{0} && \text{(3.9f)} \end{aligned}$$

The upper and lower bound limit on $\tilde{\mathbf{m}}$ and $\tilde{\mathbf{d}}$ in (3.9b) and (3.9c) are determined by the RES source or ESS considered. For wind RES, this is determined by the wind turbine rotor speed which is proportional to the wind speed, and for a battery ESS, it is determined by the capacity and state of charge. These value typically vary depending on the time of the day and operating conditions but we assume that they are fixed for the optimization period which is in seconds.

The constraints on the Lyapunov equation and its dual in (3.9d) and (3.9e) makes the problem non-convex and difficult to solve using existing algorithms. This non-convexity can be observed in the multiplication of matrix $\boldsymbol{A}$ and $\boldsymbol{P}$, and $\boldsymbol{A^T}$ and $\boldsymbol{Q}$ which consists of the design and unknown variables. Despite the non-convexity of the objective function, it is smooth [119] and therefore an explicit gradient can be derived and the optimal values of the coefficient obtained using:

$$\boldsymbol{\alpha}^{k+1} = \text{Proj}_{\mathcal{C}}[\boldsymbol{\alpha}^{k} - \gamma \bigtriangledown \boldsymbol{J}\ (\boldsymbol{\alpha}^{k})] \tag{3.10}$$

where $\boldsymbol{\alpha} = [\tilde{\mathbf{m}},\ \tilde{\mathbf{d}}]^T$ and $\mathcal{C}$ is the set of feasible $\tilde{\boldsymbol{m}}$ and $\tilde{\boldsymbol{d}}$ values. A projected gradient descent technique can be used for the optimization since the constraints on $\tilde{\boldsymbol{m}}$ and $\tilde{\boldsymbol{d}}$ form a boxed constraint.

3.4.2 Gradient Computation

Inspired by [120], a computationally efficient gradient of the objective function in (3.9) is obtained as follows:

Let $\boldsymbol{\alpha}$ be a vector of unknown $\tilde{\boldsymbol{m}}$ and $\tilde{\boldsymbol{d}}$ variable in matrix $\boldsymbol{A(\tilde{m}, \tilde{d}), B(\tilde{m})}$ and $\boldsymbol{C(\tilde{m})}$. Taking the derivative of (3.7a) w.r.t $\boldsymbol{\alpha}$, we have:

$$\frac{\boldsymbol{\partial J}}{\boldsymbol{\partial \alpha}} = \text{Tr}\left(\frac{\boldsymbol{\partial P}}{\boldsymbol{\partial \alpha}}\boldsymbol{(C^T C)}\right) + \text{Tr}\left(\boldsymbol{P}\frac{\boldsymbol{\partial (C^T C)}}{\boldsymbol{\partial \alpha}}\right) \tag{3.11}$$

Re-arranging (3.8b) and substituting into (3.11):

$$\frac{\partial \boldsymbol{J}}{\partial \boldsymbol{\alpha}} = \mathrm{Tr}\bigg(\frac{\partial \boldsymbol{P}}{\partial \boldsymbol{\alpha}} \,.\, -\left(\boldsymbol{A}^T\boldsymbol{Q} + \boldsymbol{Q}\boldsymbol{A}\right)\bigg) + \mathrm{Tr}\left(\boldsymbol{P}\frac{\partial(\boldsymbol{C}^T\boldsymbol{C})}{\partial \boldsymbol{\alpha}}\right) \tag{3.12a}$$

$$= -2\mathrm{Tr}\left(\frac{\partial \boldsymbol{P}}{\partial \boldsymbol{\alpha}}\boldsymbol{Q}\boldsymbol{A}\right) + \mathrm{Tr}\left(\boldsymbol{P}\frac{\partial(\boldsymbol{C}^T\boldsymbol{C})}{\partial \boldsymbol{\alpha}}\right) \tag{3.12b}$$

Taking the derivative of (3.8a) w.r.t $\boldsymbol{\alpha}$, post multiplying by $\boldsymbol{Q}$ and taking the trace of the resulting equation:

$$-2\mathrm{Tr}\left(\frac{\partial \boldsymbol{P}}{\partial \boldsymbol{\alpha}}\boldsymbol{Q}\boldsymbol{A}\right) = 2\mathrm{Tr}\left(\frac{\partial \boldsymbol{A}}{\partial \boldsymbol{\alpha}}\boldsymbol{P}\boldsymbol{Q}\right) + \mathrm{Tr}\left(\frac{\partial(\boldsymbol{B}\boldsymbol{B}^T)}{\partial \boldsymbol{\alpha}}\boldsymbol{Q}\right) \tag{3.13}$$

Finally, substituting (3.13) into (3.12b) gives the gradient:

$$\frac{\partial \boldsymbol{J}}{\partial \boldsymbol{\alpha}} = 2\mathrm{Tr}\left(\frac{\partial \boldsymbol{A}}{\partial \boldsymbol{\alpha}}\boldsymbol{P}\boldsymbol{Q}\right) + \mathrm{Tr}\left(\frac{\partial(\boldsymbol{B}\boldsymbol{B}^T)}{\partial \boldsymbol{\alpha}}\boldsymbol{Q}\right) + \mathrm{Tr}\left(\boldsymbol{P}\frac{\partial(\boldsymbol{C}^T\boldsymbol{C})}{\partial \boldsymbol{\alpha}}\right) \tag{3.14}$$

The gradient of $\beta\|\tilde{\mathbf{m}}\|_2^2$ is given as $2\beta\tilde{\mathbf{m}}$. The overall gradient of the objective function $J_T(\boldsymbol{\alpha})$ will therefore be:

$$\boldsymbol{\nabla} \boldsymbol{J}_{\boldsymbol{\alpha}} = 2\mathrm{Tr}\left(\frac{\partial \boldsymbol{A}}{\partial \boldsymbol{\alpha}}\boldsymbol{P}\boldsymbol{Q}\right) + \mathrm{Tr}\left(\frac{\partial(\boldsymbol{B}\boldsymbol{B}^T)}{\partial \boldsymbol{\alpha}}\boldsymbol{Q}\right) + \mathrm{Tr}\left(\boldsymbol{P}\frac{\partial(\boldsymbol{C}^T\boldsymbol{C})}{\partial \boldsymbol{\alpha}}\right) + 2\beta\tilde{\mathbf{m}} \tag{3.15}$$

3.5 Case Study

The optimization problem in (3.9) is implemented using a modified 12 bus three-area test case [2] [35] shown in Fig. 3.2. The network is reduced to an equivalent network by removing the static load buses (3, 7 and 11) using the Krons reduction method. Also, the available inertia and load damping at the remaining buses are reduced to model a scenario of high penetration of RES. We assume that there are inverter-connected RES at each bus which implies that in the matrix representation of the swing equation in (3.2), $\boldsymbol{m_T} = \mathbf{m} + \tilde{\mathbf{m}}$ and $\boldsymbol{d_T} = \mathbf{d} + \tilde{\mathbf{d}}$ where $\mathbf{m}$ and $\mathbf{d}$ are the inertia and damping coefficients of the synchronous generator respectively, while $\tilde{\mathbf{m}}$ and $\tilde{\mathbf{d}}$ are the virtual inertia and damping coefficients of the VSM frequency control loop in Fig. 3.1 to be designed.

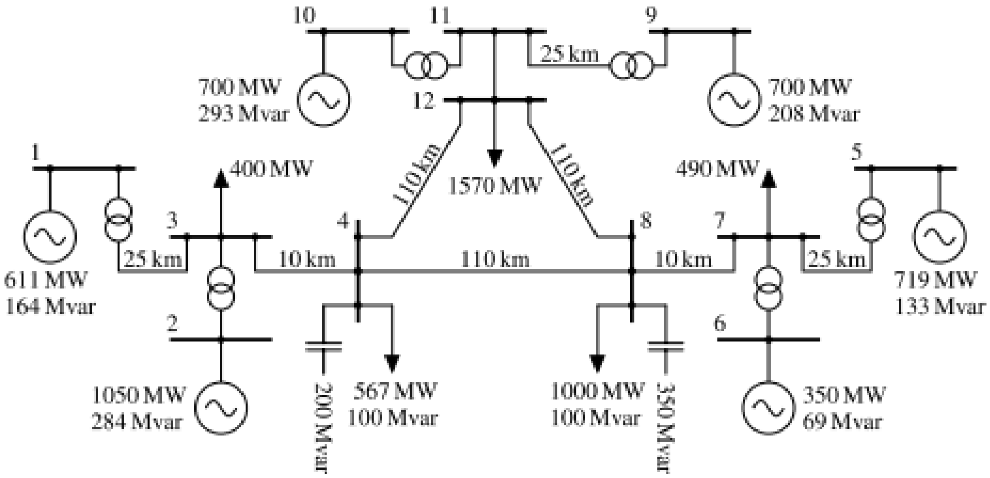

Figure 3.2: Schematic diagram of a 12-bus, 6-generator three-area test case system with IBRs running the VSM algorithm assumed to be connected at each generator node [2].

The disturbance to the system is a partial loss in capacity of the generator at bus 6 which is modeled as a step input to that bus. The minimum inertia and damping at each bus is taken to be the modified inertia and damping of the actual generators at buses while the maximum inertia and damping at each bus is taken to be four times the modified inertia and damping of the actual generators at buses. To verify the effectiveness of the proposed algorithm in the result analysis, the optimal result is compared with assigning the relevant extrema values to the inertia and damping, that is, maximum damping and minimum inertia $(\boldsymbol{d}_{max}, \boldsymbol{m}_{min})$ which gives a faster response time but bigger overshoot, and maximum damping and inertia $(\boldsymbol{d}_{max}, \boldsymbol{m}_{max})$ which gives a slower response time but smaller overshoot. The other combinations give poor results as such will not be used in the analysis.

3.5.1 Disturbance Location Unknown

Fig. 3.3 and 3.4 show the total inertia and damping coefficient distribution across the nodes when the disturbance location is not known beforehand and therefore equally likely to occur at any node. These total coefficients $(\boldsymbol{m_T}$ & $\boldsymbol{d_T})$ are a sum of the actual synchronous machines coefficients ($\boldsymbol{m}$ & $\boldsymbol{d}$) and the virtual coefficients of the VSM ($\tilde{\boldsymbol{m}}$ & $\tilde{\boldsymbol{d}}$), and varies across the network due to the ability to optimize the virtual coefficients. The total inertia and damping coefficients across the network from each node are $\sum m_{T,i} = 173.54$ and $\sum d_{T,i} = 112.50$ respectively. It can be observed that the damping coefficient is maximally assigned to avoid oscillations in the system while the inertia is strategically assigned to ensure that the overall frequency control objective is minimized. Fig. 3.5 and Fig. 3.6 show the frequency response at the disturbed node 6, for clearer viewing, and at all the nodes respectively which results from the inertia and damping placement in Fig. 3.3 and 3.4. From these frequency responses, it can be seen that the optimal inertia and damping coefficient values result in a time response that achieves a balance between having a fast settling time but high frequency nadir and fast ROCOF, and a slow settling time but low frequency nadir and slow ROCOF. In this situation where it is not possible to simultaneously achieve these objectives, a Pareto front is achieved by the optimization problem in (3.9).

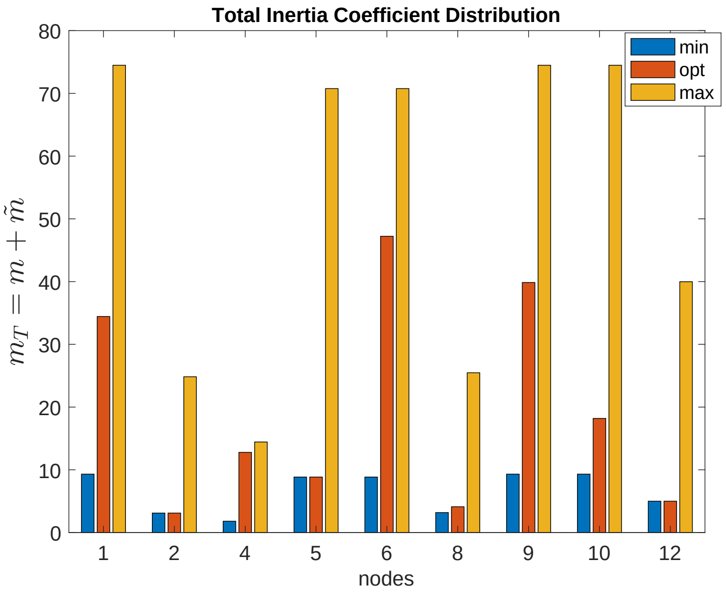

Figure 3.3: Optimal inertia coefficient distribution across all nodes assuming the location of disturbance is unknown.

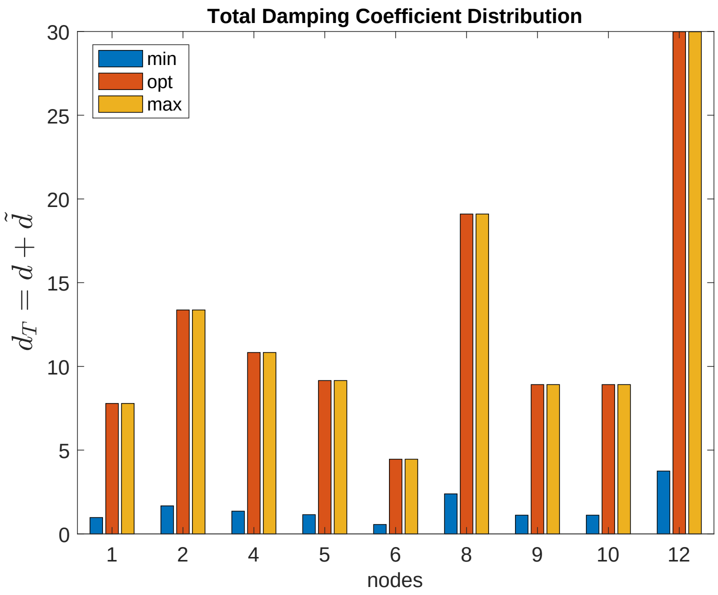

Figure 3.4: Optimal damping coefficient distribution across all nodes assuming the location of disturbance is unknown.

Fig. 3.7 sheds more light on the frequency response in Fig. 3.6 by showing the eigenvalues (pole placements) due the inertia and damping distribution across the network considered. As observed in Fig. 3.7(a), the farther away the poles are from the imaginary axis, the faster it takes for the system to arrive at steady state, albeit with a larger deviation due to the magnitude of the poles, as observed in the response in Fig. 3.6(a). Conversely, as observed in Fig. 3.7(c), the closer the poles are to the imaginary axis, the slower it takes for the system to arrive at steady state as observed in the response in Fig. 3.6(c) but it also results in a smaller deviation due to the magnitude of the poles. The optimal case is able to trade-off these extremes resulting in a balanced response.

Varying β

The effect of β in (3.9) can be observed in Fig. (3.8). Varying β determines the extent of the trade-off between the ROCOF/frequency nadir and settling time, for example, in the case of providing a fast inertia response, a small frequency deviation and slow ROCOF is

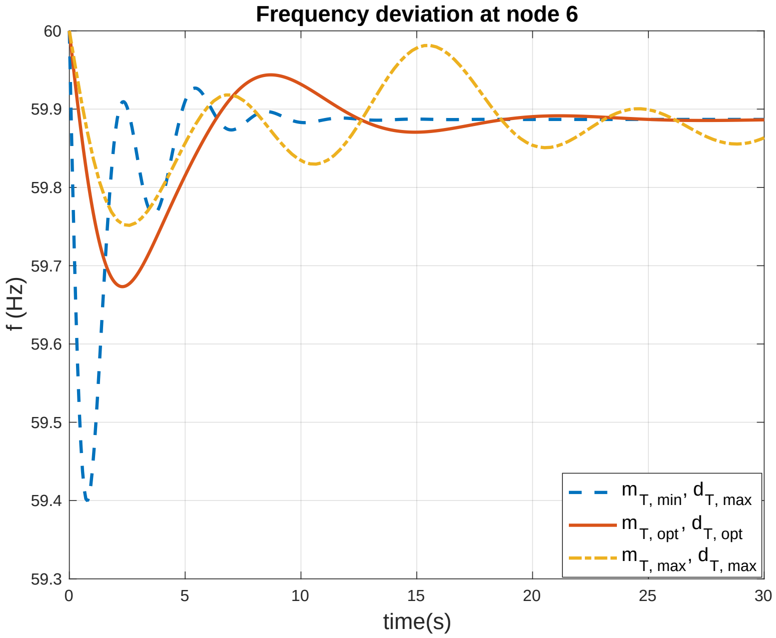

Figure 3.5: Frequency deviation at node 6 due to partial loss of generating capacity at node 6 assuming the location of disturbance is unknown. The optimal response is a trade of between a large frequency deviation and ROCOF but fast settling time and a small frequency deviation and ROCOF but slow settling time.

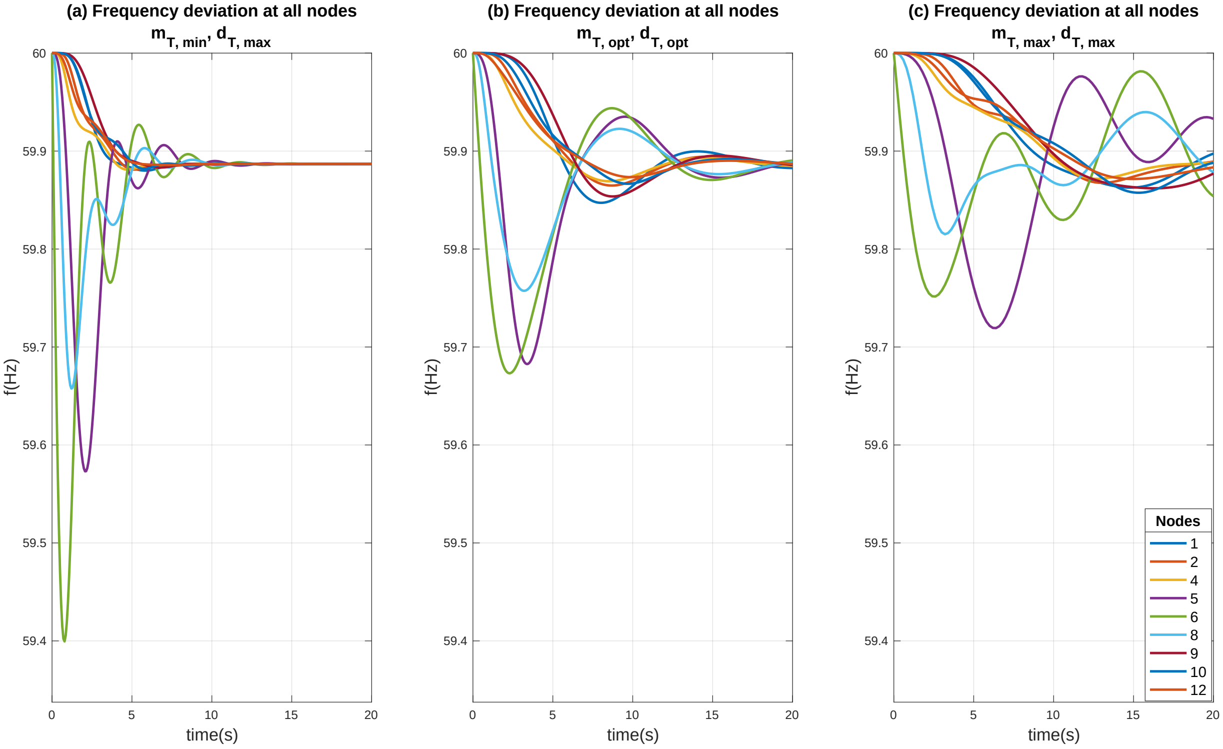

Figure 3.6: Frequency deviation at all nodes due to partial loss of generating capacity at node 6 assuming the location of disturbance is unknown. (a): Frequency response using the extrema - minimum total inertia and maximum total damping; (b): Frequency response using the optimum total inertia and damping; (c): Frequency response using the extrema - maximum total inertia and damping. It shows the same trade-off properties across all nodes and how the optimal coefficients results in a balanced smoother response at all the nodes.

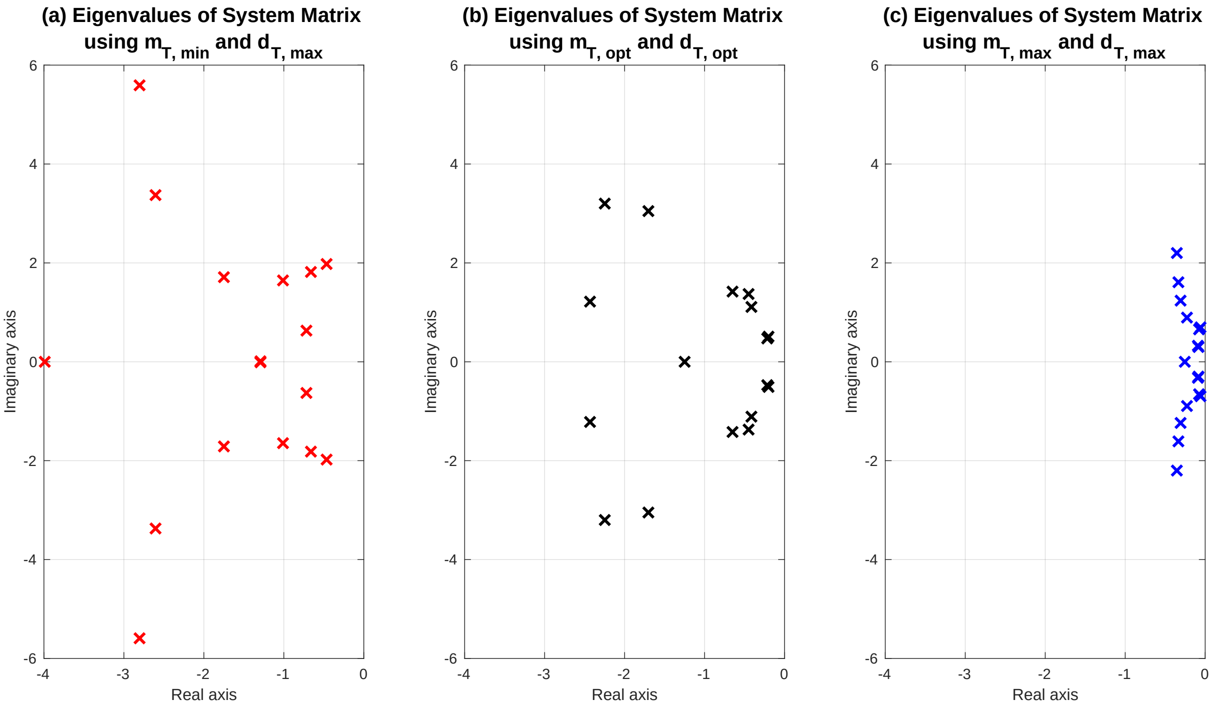

Figure 3.7: System eigenvalue analysis when (a): using the extrema - minimum total inertia and maximum total damping; (b): using the optimum total inertia and damping; (c): using the extrema - maximum total inertia and damping.

desired. The β therefore controls the amount inertia in the system to achieve the desired the ROCOF.

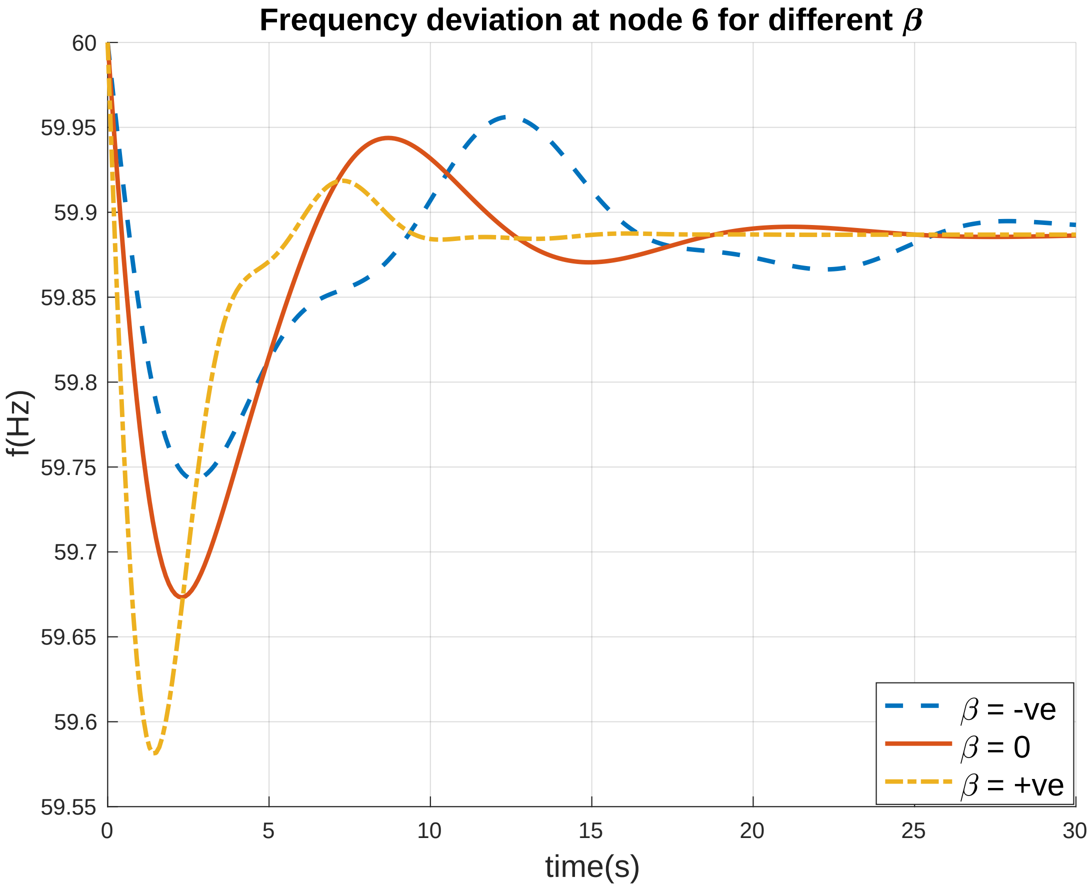

Figure 3.8: Frequency deviation at node 6 due to step input for different values of β. A negative β value results in a lower ROCOF and smaller frequency deviation but slower time response while a positive β value results in a higher ROCOF and larger frequency deviation but faster time response.

3.5.2 Disturbance Location Known

We consider next, how the inertia and damping coefficient distribution across the nodes changes if the location of the disturbance is known beforehand due to prior history or vulnerabilities. For this case, we assume the disturbance is likely to occur at node 6, we therefore have that $\triangle \boldsymbol{P}$ in (3.2) is given by $\triangle \boldsymbol{P} = \boldsymbol{\eta \Delta}(t)$. The $\Delta(t)$ represents a step input and $\boldsymbol{\eta}$ is represented by the standard basis $\mathbf{e_i}$ in the direction of node 6 and is pre-multiplied by the matrix $\boldsymbol{B}$ in (3.2) before the optimization. The observations from the results in Fig. 3.9 - 3.12 show a reduction in the optimal inertia and damping coefficient distribution across the nodes for a similar disturbance and time response compared to the response in Fig.3.3 - 3.6 where no knowledge of the disturbance is assumed. Compared to Fig.3.3, the optimal inertia allocation in Fig. 3.9 is highest at the disturbed node while the optimal damping values in Fig. 3.10 is not maximally assigned across board as in the unknown disturbance case in Fig. 3.4. The total inertia and damping coefficients values for the known disturbance case are $\sum m_i = 118.86$ and $\sum d_i = 85$ respectively, which is smaller than the unknown case. This implies that a possible knowledge of the disturbance enables a more efficient resource distribution for similar frequency response across the system.

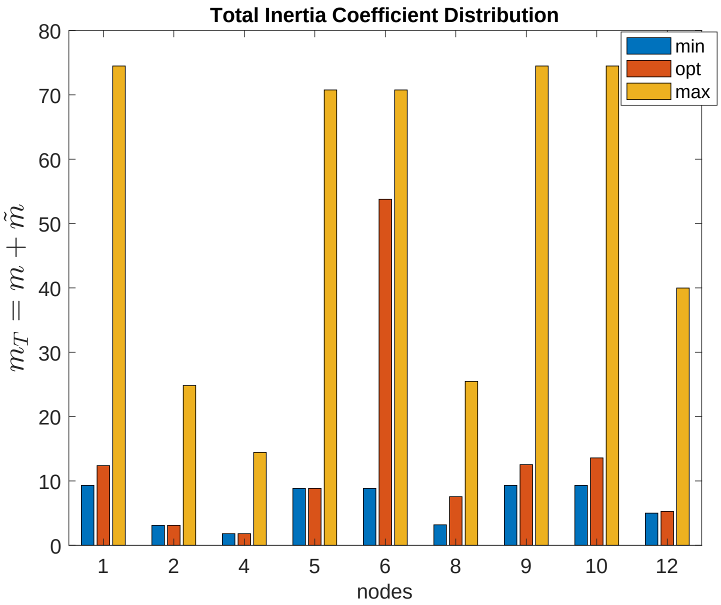

Figure 3.9: Optimal inertia coefficient distribution across all nodes assuming the location of disturbance is known.

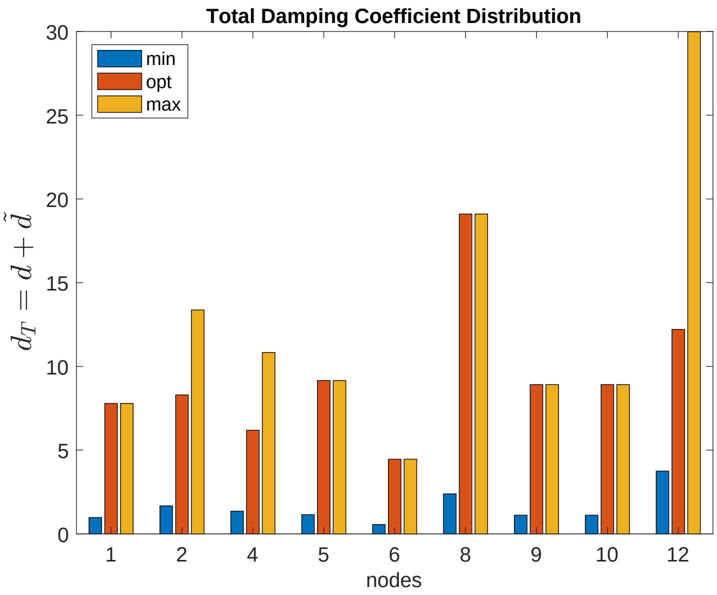

Figure 3.10: Optimal damping coefficient distribution across all nodes assuming the location of disturbance is known.

As stated in the unknown disturbance scenario, Fig. 3.13 also sheds more light on the frequency response in Fig. 3.12 by showing the eigenvalues (pole placements) due the same scenarios of inertia and damping distribution across the network considered. It can be observed that the optimal case is still a trade-off between the extrema and while the poles appear pushed further to the imaginary axis, the resulting frequency response is still faster in settling with a smaller frequency deviation.

Based on these analysis, it can be seen that the control weight β gives the ability to control the frequency performance requirements. Also, computing an optimal value for the $\tilde{\mathbf{m}}$ and $\tilde{\mathbf{d}}$ requires some knowledge of the system state and history. If this is unknown, the optimal values are allocated in a robust way to cater for all disturbance scenarios. The $\tilde{\mathbf{m}}$ and $\tilde{\mathbf{d}}$ design variables can be recomputed and the new values assigned to the gain blocks of the inverter controller at every operating point. This will be required as the operating point and parameters of the power systems network changes depending on the units committed.

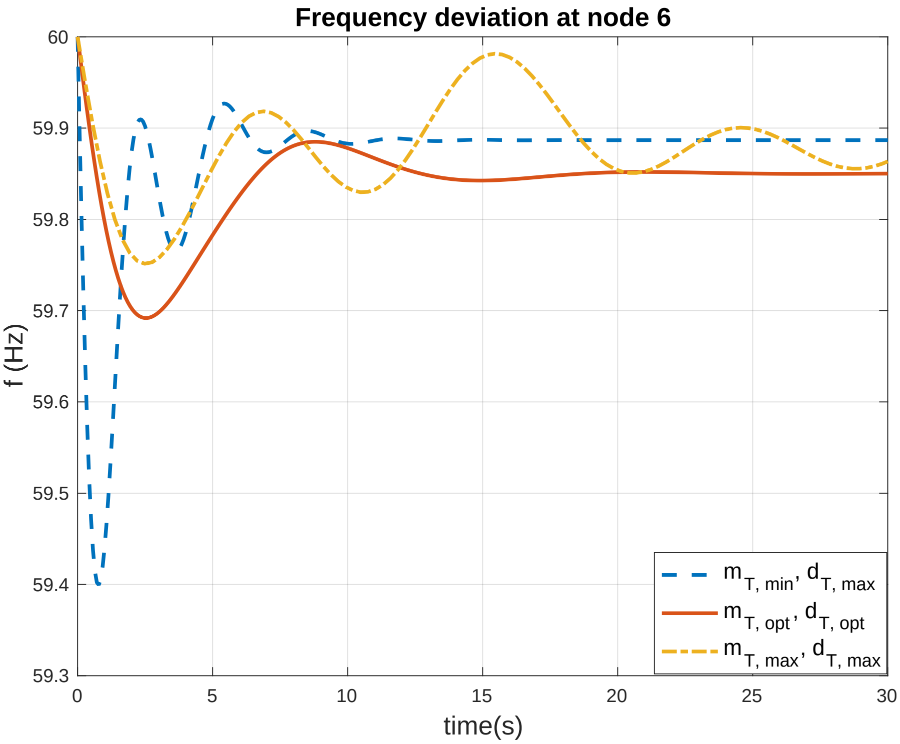

Figure 3.11: Frequency deviation at node 6 due to partial loss of generating capacity at node 6 assuming the location of disturbance is known. The optimal response is still is a trade of between a large frequency deviation and ROCOF but fast settling time and a small frequency deviation and ROCOF but slow settling time, despite reduction in inertia and damping values

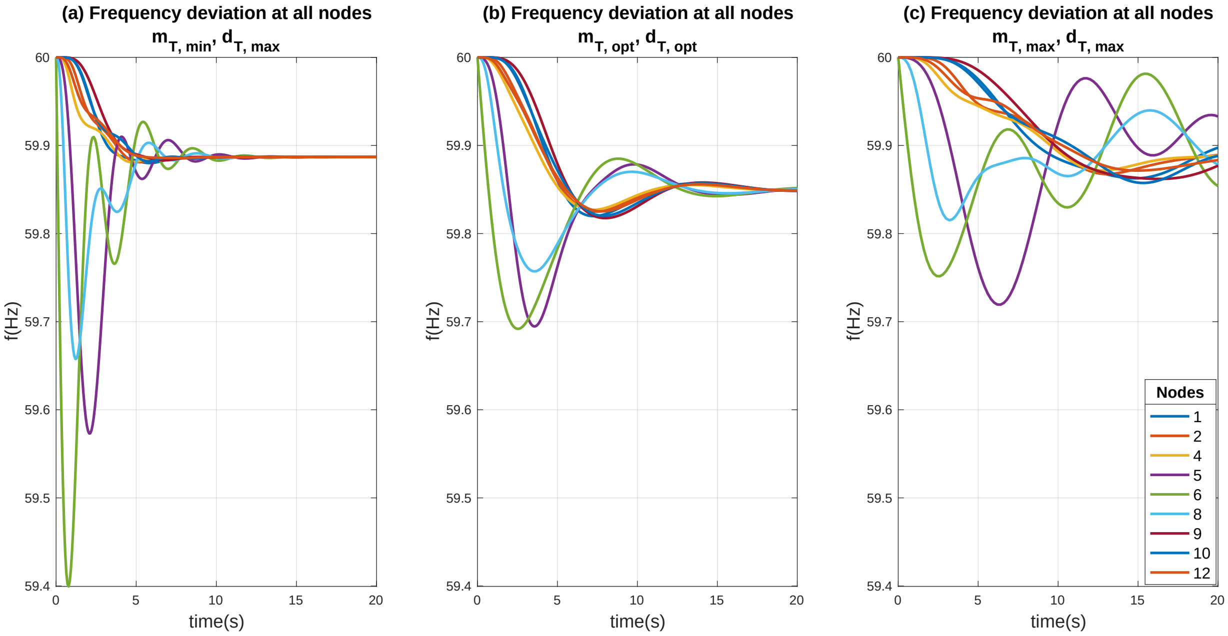

Figure 3.12: Frequency deviation at all nodes due to partial loss of generating capacity at node 6 assuming the location of disturbance is known. (a): Frequency response using the extrema - minimum total inertia and maximum total damping; (b): Frequency response using the optimum total inertia and damping; (c): Frequency response using the extrema - maximum total inertia and damping. It shows same trade-off properties across all nodes and how the optimal coefficients results in a balanced smoother response at all the nodes.

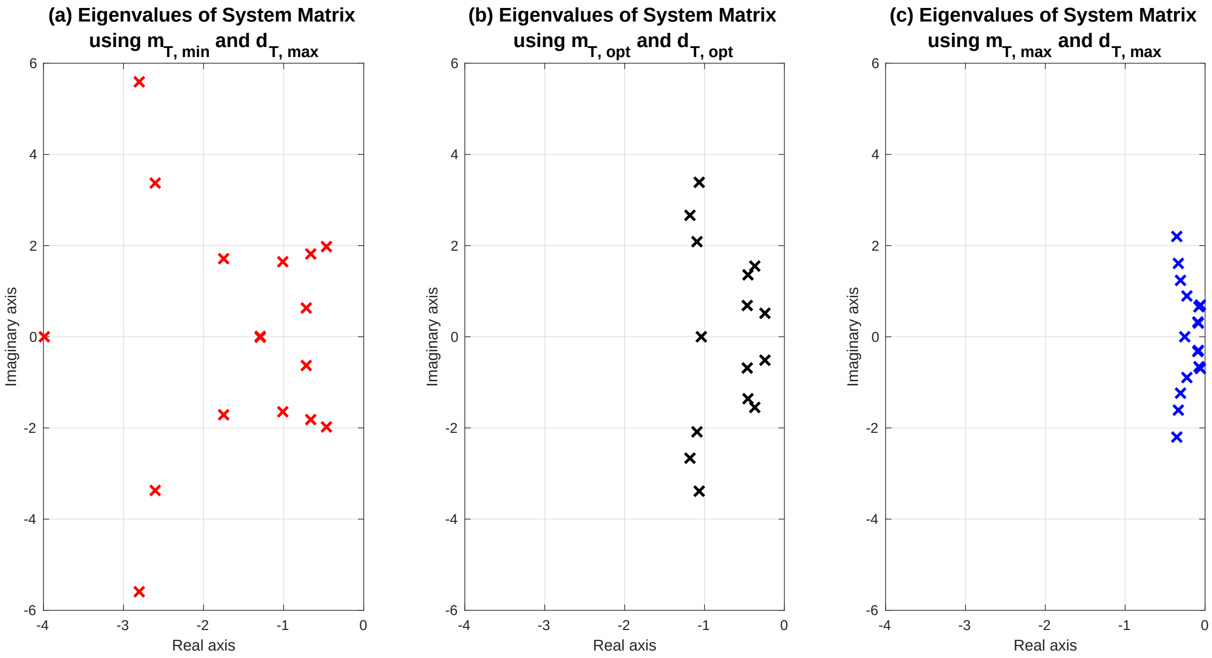

Figure 3.13: System eigenvalue analysis when (a): using the extrema - minimum total inertia and maximum total damping; (b): using the optimum total inertia and damping; (c): using the extrema - maximum total inertia and damping.

3.6 Conclusion

We considered the problem of optimally designing the virtual inertia and damping coefficient of a VSM that mimics the inertia response of a synchronous generator by injecting additional active power proportional to the ROCOF and frequency deviation. We used an augmented $\mathcal{H}_2$ norm objective function to incorporate the time domain frequency response requirements and provide an explicit computationally efficient gradient to compute the coefficient values. We applied this method to a test case and our time domain simulation performed as expected from the theory. We also showed via simulation, how the knowledge of a potential disturbance location could help in efficiently computing the coefficients.

Chapter 4

INVERTER POWER CONTROL IN LOW-INERTIA POWER SYSTEMS

4.1 Introduction

4.1.1 Motivation

The electric grid has been undergoing a transition from a network with dynamics fully governed by synchronous machines to a mixed-source network with dynamics governed by both synchronous machines and inverter-based resources (IBRs). This transition is marked by a reduction in the amount of mechanical inertia in the system, which has led to more pronounced frequency responses to disturbances and faults in the grid [15, 16]. At the same time, by the virtue of the speed of power electronic circuits, IBRs such as solar, wind and energy storage have the capability to respond to frequency changes in the grid at a much faster rate than traditional generators with rotating masses. The challenge of how to best utilize these new capabilities has spurred much research interest in the last few years (e.g., see [17] and the references within).

4.1.2 Literature Review

Various control strategies that utilizes the IBRs has been proposed. The goal of these strategies is to design the active power response of the IBRs to changes in frequency, such that some objective is minimized. For example, standard objectives of interests are the magnitude of the frequency deviation, the rate of change of frequency (ROCOF) and the settling time. A unique challenge in the control of IBRs is that they tend to face much tighter limits than conventional machines. For example, solar and wind resources cannot increase their power output beyond the maximum power tracking point, which introduces a hard (and asymmetrical) constraint on the action of the inverters. For a storage unit, it has only a limited amount of energy that can be used to respond to a disturbance.

Of the varying control strategies proposed for IBRs, *droop control* [26–28] and *virtual synchronous machines* (VSMs) [31, 32, 114] are the most popular as they function by mimicking the frequency-power dynamic response of a synchronous machine. As suggested by their names, droop control injects/absorbs an amount of active power in proportion to the frequency deviation, and VSMs act as a second order oscillator to provide inertia and damping to the grid. The parameters (droop slope, inertia and damping constants) used in these strategies can be optimized using a number of techniques [2, 79, 80].

The structural simplicity of VSMs also leads to a fundamental limitation [79, 81]. Since there are only two parameters to tune (inertia and damping), there is an inherent trade-off between different objectives and there is no choice of parameters that will make the frequency deviation, ROCOF, and settling time small at the same time [79]. In addition, it is difficult to include hard constraints, since simply thresholding the output once the constraints are reached tend to lead to very poor performances [121]. Adaptive rules can be used to alleviate this drawback somewhat, and works in [81–83] change the parameter based on the measured frequency deviation and ROCOF values. However, it is difficult to find an optimal rule to update these parameters in real-time.

4.1.3 Contributions

The contributions of this chapter are as follows:

- We propose a novel control strategy called the Inverter Power Control (IPC), based on model predictive control (MPC), by explicitly formulating the problem of finding the optimal active power set-point of an IBR to minimize the frequency deviation and the ROCOF in the network. It turns out that this formulation also implicitly minimizes the systems settling time.
- We derive a modified swing equation to model the dynamics of a mixed-source net-

work to be used with the MPC algorithm which requires a model of the system to be optimized. This derived model is represented in a form such that the active power set-point is obtained using the IBRs internal angle as control input.

- We model an observer to estimate unmeasured disturbances and states in the event of disturbances or limited communication in the system, where only limited buses are equipped with measurement devices (e.g. PMUs). We show that our proposed IPC framework is still applicable to these variations in systems operating conditions.

More specifically, at any timestep, using system states obtained from wide-area measurements [98], we simulate the dynamics of the systems for a finite horizon, then find the best set-points that optimizes the objective over that horizon. The first action is then adopted for the current timestep, and the process repeats. Our approach is similar in spirit to the ones in [81–83] since an objective is optimized in an online fashion. However, instead of optimizing the parameters, we directly find the best power set-points. This approach turns out to provide both an easier optimization problem and better control performances since the hard constraints on the IBRs are explicitly included in the optimization process.

Through simulation studies, we show that the IPC strictly outperforms optimally tuned VSMs for the IEEE 3-machine 9-bus and New England 39-bus system, even under limited communication and large measurement noises.

The remainder of this paper is organized as follows: Section 5.2 defines the models used in this paper. Section 4.3 presents the design and formulation of the IPC algorithm. Section 4.4 presents the state and disturbance observer design. Section 5.5 compares the performances of IPC to VSMs in a standard test system. Section 5.6 concludes the paper.

4.2 Modeling

We denote the real line by $\mathbb{R}$, the cardinality of a set $\mathcal{S}$ as $|\mathcal{S}|$, the $n \times n$ identity and zero matrices as $\boldsymbol{I}_n$ and $\mathbf{0}_n$, respectively. Matrices and vectors are denoted by a bold-faced variables.

4.2.1 System Structure

Steady state conditions in a power systems are achieved when there is a balance between the power produced by the generating sources and the power consumed by loads and lossy components. For stability analysis, the entire system can be reduced to an equivalent network via Kron reduction [122]. This eliminates passive and non-dynamic load buses and leaves only buses with at least one generating source connected. With this in place, frequency stability analysis can be carried out, with the frequency dynamics governed by the reactions of buses to active power imbalances in the system.

In this work, we assume the availability of state variables and network information for control purposes. In a later section, we will relax this assumption to partial availability of state variables from some generators.

Because the generators and IBRs had different dynamics, we denote their sets by $\mathcal{G}$ and $\mathcal{I}$, respectively. Note that the total number of generating sources in the network is $\mathcal{N} := \mathcal{G} \cup \mathcal{I}$.

4.2.2 Synchronous Machines

The rotor dynamics of each synchronous generator in a given power system is governed by the well-known swing equation [123]. Here we adopt a discretized version of the equations, which in per unit (p.u.) system is:

$$\begin{aligned} \omega_i^{t+1} &= \omega_i^t + \frac{h}{m_i}\left(P_{\mathrm{m},i}^t - P_{\mathrm{e},i}^t - d_i\omega_i^t\right), \\ \delta_i^{t+1} &= \omega_\mathrm{b}\left(\delta_i^t + h\;\omega_i^{t+1}\right), \end{aligned} \tag{4.1}$$

$\forall i \in \mathcal{G}$ where h is the step size for the discrete simulation, δ_i (rad) is the rotor angle, $\omega = \bar{\omega}_i - \omega_0$ is the rotor speed deviation, ω_b is the base speed of the system, m_i is the inertia constant, d_i is the damping constant, $P_{\mathrm{m},i}$ is the mechanical input power and $P_{\mathrm{e},i}$ is the electric power output of the i^{th} machine.

The electrical output power $P_{\mathrm{e},i}$ is given by the AC power flow equation in terms of the internal emf $|E_i|$ and rotor angle δ_i:

$$P^t_{\mathrm{e},i} = \sum_{i\sim j} |E_i E_j| [g_{ij}\cos(\delta^t_i - \delta^t_j) + b_{ij}\sin(\delta^t_i - \delta^t_j)], \tag{4.2}$$

$\forall i, j \in \mathcal{G}$, where $g_{ij} + jb_{ij}$ is the reduced admittance between nodes i and j. We assume the internal emf are constant because of the actions of the exciter systems.

The nonlinearity of the AC power flow in (5.2) makes (5.1) difficult to use for control applications. Linearizing (5.1) around the nominal point and using the DC power flow approximation [35], the bus dynamics become:

$$\begin{aligned} \triangle\omega^{t+1}_i &= \triangle\omega^t_i + \frac{h}{m_i}\left(\triangle P^t_{\mathrm{m},i} - \triangle P^t_{\mathrm{e},i} - d_i \triangle \omega^t_i\right), \\ \triangle\delta^{t+1}_i &= \omega_{\mathrm{b}}\left(\triangle\delta^t_i + h \ \triangle \omega^{t+1}_i\right), \end{aligned} \tag{4.3}$$

where $\triangle P^t_{\mathrm{e},i} = \sum_{i\sim j} b_{ij} \triangle \delta^t_{ij}$ is the dc power flow between 2 buses. We model changes to the mechanical input power $\triangle P^t_{\mathrm{m},i}$ by a combination of droop and automatic governor control (AGC) actions [35] according to the discretized equation (see appendix B.1 and B.2 for derivation):

$$\begin{gathered} \triangle P^{t+1}_{\mathrm{m},i} = \frac{1}{1+hk_1}\Bigg(\left[2 + hk - \frac{h^2 k_2}{m_i}\right] \triangle P^t_{\mathrm{m},i} - \triangle P^{t-1}_{\mathrm{m},i} + \\ h^2\left[\left(\frac{k_2 d_i}{m_i} - k3\right) \triangle \omega^t_i - \frac{k_2}{m_i}\left(\triangle P^t_{\mathrm{e},i}\right)\right]\Bigg), \end{gathered} \tag{4.4}$$

where k_1, k_2 and k_3 are the gain coefficients of the droop and AGC controller.

4.2.3 Virtual Synchronous Machine (VSM)

From the network point of view, the grid-connected IBR is seen as producing a constant power according to its predetermined set-point and fast dynamics governed by closed-loop controls actions [124]. When configured in the grid-following mode, these controls help maintain the output power of the IBRs while remaining synchronized to the terminal voltage set by the grid [59]. For system analysis, the inverter can be modeled as a voltage source behind a reactance, much like a synchronous machine as shown in Fig. 4.1.

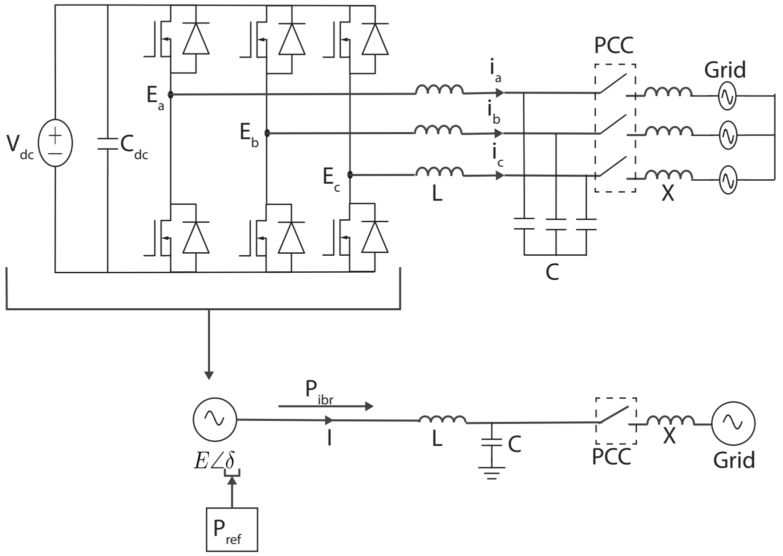

Figure 4.1: Schematic diagram of a grid-connected IBR showing its configuration and representation as a voltage source behind a reactance

In the event of a power imbalance in the network reflected by a frequency deviation, an inverter does not have a "natural" response to frequency deviation as synchronous machines does since they are made of power electronics components and have no rotating mass. To elicit some response, an additional control loop is therefore needed to enable the inverters participate in frequency control by changing the power set-point of the inverter based on frequency measurements. The concept of virtual synchronous machine (VSM) has been proposed in literature to provide this additional control loop and it comes in different configurations [32, 33, 75]. The basic idea is to mimic the behavior of a synchronous machine's response to a frequency deviation by choosing appropriate gains corresponding to the inertia and damping of the machines and producing power proportional to the ROCOF and frequency deviation. Since the response of the inverter is entirely digital, it can be programmed with almost arbitrary functions.

In this work, we adopt the frequency-power VSM configuration in [33] where the IBR control measures the grid frequency denoted as $\triangle\omega_{ibr}$ using the phase locked loop (PLL) [61] and computes the additional power

$$\triangle P = \triangle P_{\text{km}} + \triangle P_{\text{kd}} = K_{\text{m}} \frac{d \triangle \omega_{\text{ibr}}}{dt} + K_{\text{d}} \triangle \omega_{\text{ibr}} \tag{4.5}$$

by which to modify the initial real power set-point P_0 to a new set-point P_{ref} according, to combat the frequency decline. The gains K_{m} and K_{d} represent the virtual inertia and damping constants respectively. A block diagram representing this process is shown in Fig. 4.2. In contrast to synchronous machines where the constants are decided by the physical parameters, these constants of the VSM can be optimized over [79].

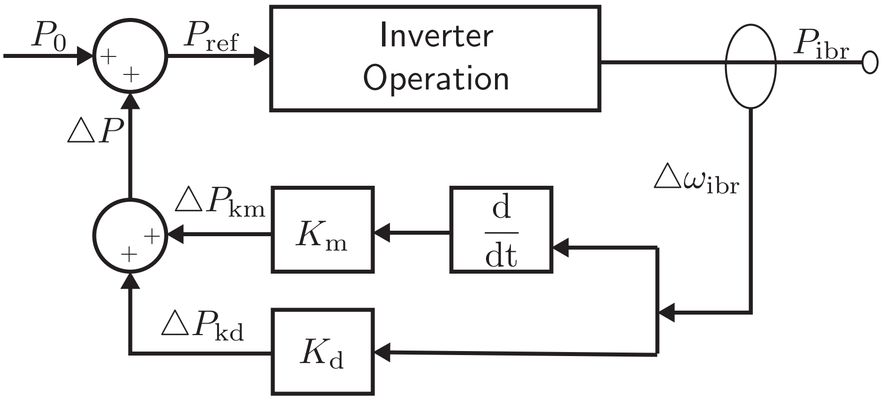

Figure 4.2: Block Diagram showing the operation of the VSM control loop which utilizes a feedback PD control mechanism to enable the IBR participate in frequency control

To simplify the model in (4.5) for simulation purposes, we assume the grid frequency measured locally by the PLL, that is, the local frequency at the IBR node, is approximately equal to the center of inertia (COI) frequency [124, 125]. This represents an inertia-weighted average frequency given by:

$$\triangle \omega_{ibr} = \frac{\sum_{i=1}^{n} m_i \triangle \omega_i}{\sum_{i=1}^{n} m_i} \tag{4.6}$$

where $n = |\mathcal{G}|$, $\triangle \omega_i$ is the rotor speed deviation, and m_i is the inertia constant of the i^{th} synchronous generators in the network. Using this COI approximation highlights one of the drawbacks of existing VSM configuration as it is difficult to numerically determine the local frequency at a bus and efforts to utilize geographically close generators to approximate the local frequency results in poor VSM controller performance.

As stated in the introduction, even though the constants in the VSM can be adjusted, they do not provide enough degrees of freedom to optimize the active power output of the inverter. In the next section, we fully leverage the flexibility of the power electronic interfaces using a MPC framework.

4.3 Inverter Power Control (IPC)

In this work, we propose a novel method for controlling the output power of the IBR, called the Inverter Power Control (IPC). This controller functions by modifying the initial real power set-point P_0 to a new set-point P_{ref} as shown in Fig. 4.3 at each time step such that a weighted sum of the frequency deviation and ROCOF is minimized. Due to the timescale difference between IBRs and synchronous machines, the real power set-points of an IBR can be set almost instantaneously. Therefore, the important question becomes how to solve the optimization problem at each time step fast enough to find the real power set-point and how much communication is required in performing these calculations. In this section, we describe how to formulate the optimization problem and provide an efficient algorithm, assuming all of the information are known at the IBR. The next section then discusses how to deal with limited and noisy measurements, as well as incomplete communication.

For the k^{th} IBR, let u_k denote its angle (referenced to the slack-bus). We think of this u_k as the control variable in the optimization problem. Note that the actual control of the IBR is not done via angle control, rather, we use the optimized u_k to find the corresponding active power output of the inverter, then set the inverter to that power.

To determine this real power set-point at a given time step, consider the power flow equation in (5.2), we write out the i^{th} generator's power output $P_{\text{e},i}$ into two parts: power flowing from the i^{th} generator to other generator denoted as $P_{\text{eG},i}$ and from the i^{th} generator to IBRs

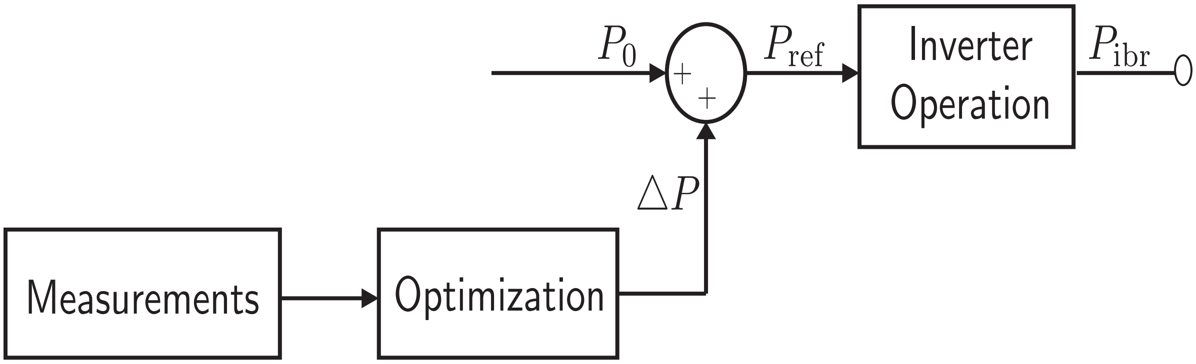

Figure 4.3: Block Diagram showing the operation of the IPC controller which utilizes state and network variables to modify the real power set-point of the IBR at each timestep

denoted as $P_{\mathrm{eI},i}$, such that:

$$\begin{aligned} P_{\mathrm{e},i} &= P_{\mathrm{eG},i} + P_{\mathrm{eI},i} \\ &= \sum_{i\sim j,i,j\in\mathcal{G}} |E_iE_j|[g_{ij}\cos(\delta_i-\delta_j)+b_{ij}\sin(\delta_i-\delta_j)] \\ &+ \sum_{i\sim k,i,\in\mathcal{G},k\in\mathcal{I}} |E_iE_k|[g_{ik}\cos(\delta_i-u_k)+b_{ij}\sin(\delta_i-u_k)], \end{aligned} \tag{4.7}$$

and the output power from the k^{th} IBR denoted as $P_{\mathrm{ibr},k}$ can also be written in two parts as:

$$\begin{aligned} P_{\mathrm{ibr},k} &= P_{\mathrm{ibr},ki} + P_{\mathrm{ibr},kj}, \\ &= \sum_{k\sim i,k\in\mathcal{I},i\in\mathcal{G}} |E_kE_i|[g_{ki}\cos(u_k-\delta_i)+b_{ki}\sin(u_k-\delta_i)] \\ &+ \sum_{k\sim j,j,k\in\mathcal{I}} |E_kE_j|[g_{kj}\cos(u_k-u_j)+b_{kj}\sin(u_k-u_j)], \end{aligned} \tag{4.8}$$

depending on whether the kth IBR is connected to a synchronous machine or another IBR.

4.3.1 Nonlinear Optimization Problem

At any timestep, we consider the behavior of the system N steps ahead. Without loss of generality, we start the problem at time $t = 0$. The control variables are the inverter angles, which we denote as $\boldsymbol{u}^0, \boldsymbol{u}^1, \ldots, \boldsymbol{u}^{N-1}$. Once these are set, the rest of the system are governed by their swing equations. As stated before, the objective is to minimize a function of the frequency deviation and the ROCOF, and the IPC problem is given by:

$$\underset{\{\boldsymbol{u}^0,\boldsymbol{u}^1,\ldots,\boldsymbol{u}^{N-1}\}}{\text{Min.}} \sum_{t=0}^{N-1} \left\{ \|\boldsymbol{\omega}^{t+1}\|_2^2 + \frac{1}{h}\|\boldsymbol{\omega}^{t+1} - \boldsymbol{\omega}^t\|_2^2 \right\} \tag{4.9a}$$

$$\text{s.t. } \omega_i^{t+1} = \omega_i^t + \frac{h}{m_i}\big(P_{\mathrm{m},i}^t - P_{\mathrm{e},i}^t - d_i\omega_i^t - \triangle P_i^t\big),\ \forall i \in \mathcal{G} \tag{4.9b}$$

$$P_{e,i}^t = \text{Equation } (4.7),\ \forall i \in \mathcal{G} \tag{4.9c}$$

$$P_{ibr,k}^t = \text{Equation } (5.6),\ \forall k \in \mathcal{I} \tag{4.9d}$$

$$P_{\mathrm{ibr,min},k}^t \le P_{\mathrm{ibr},k}^t \le P_{\mathrm{ibr,max},k}^t, \tag{4.9e}$$

$$\sum_{t=1}^{N} P_{\mathrm{ibr,k}}^t \le E_{\mathrm{ibr,\ tot},k}^t, \tag{4.9f}$$

where $\boldsymbol{\omega}^{t+1} \in \mathcal{R}^{|\mathcal{G}|}$ is a vector of all machine frequency deviations at the next time step and $\boldsymbol{\omega}^{t+1} - \boldsymbol{\omega}^t$ is a vector of all machine ROCOF between the current and next time step. The evolution of $\boldsymbol{\omega}$ is given in (5.8b) (swing equations) with the added $\triangle P_i$ used to denote disturbances to the network which can be either a loss in generation or load, the power constraints are given in (5.8e) and the energy constraints are in (5.8f). Here we take the frequency deviation and the ROCOF to be equally weighted for simplicity, but their weighting can be adjusted as needed for different practical scenarios.

After (5.8) is solved, the control variable $\boldsymbol{u}^0$ is substituted into the power flow equations (4.7) to find the active power set-points of the IBRs. Then the IBRs hold their power at these set-points until the next time the optimization problem is solved. Note that even though only the first control variable $\boldsymbol{u}^0$ is used, we need to solve for all of the other control variables because of the time coupling in the dynamics of the system.

It turns out that the AC power flow equations in (4.7) and (5.6) makes the problem nonlinear and difficult to solve in real-time. Therefore, the next two sections uses DC power flow to obtain an approximate problem that is much easier to solve.

4.3.2 Unconstrained Linearized Problem

The main source of non-linearity in (5.8) comes from the AC power flow equations in (5.8c) and (5.8d) and we use the standard DC power flow model from (5.3) to approximate these equations.

Therefore, at bus $i \in \mathcal{G}$ (synchronous machines), we have:

$$\begin{aligned} \triangle P_{e,i} &= \triangle P_{eG,i} + \triangle P_{eI,i} \\ &= \sum_{i\sim j, j\in\mathcal{G}} b_{ij}(\triangle\delta_i - \triangle\delta_j) + \sum_{i\sim j, k\in\mathcal{I}} b_{ik}(\triangle\delta_i - u_k), \end{aligned} \tag{4.10}$$

which can be written in matrix form as:

$$\triangle \boldsymbol{P_e} = \underbrace{\begin{bmatrix} b_{ii} & -b_{ij} \\ -b_{ji} & b_{jj} \end{bmatrix}}_{\boldsymbol{B}_{\mathrm{GG}}} \begin{bmatrix} \triangle\delta_i \\ \triangle\delta_j \end{bmatrix} + \underbrace{\begin{bmatrix} -b_{ik} \\ -b_{jk} \end{bmatrix}}_{\boldsymbol{B}_{\mathrm{GI}}} u_k, \tag{4.11}$$

where $\boldsymbol{B}_{\mathrm{GG}}$ contains the connection between synchronous generators and $\boldsymbol{B}_{\mathrm{GI}}$ contains the connection between a synchronous generator and IBRs. In state space form, it becomes

$$\underbrace{\begin{bmatrix} \triangle\boldsymbol{\omega^{t+1}} \\ \triangle\boldsymbol{\delta^{t+1}} \end{bmatrix}}_{\boldsymbol{x^{t+1}}} = \underbrace{\begin{bmatrix} -\boldsymbol{M^{-1}D} & -\boldsymbol{M^{-1}B}_{\mathrm{GG}} \\ \boldsymbol{I_n} & \boldsymbol{0_n} \end{bmatrix}}_{\boldsymbol{\bar{A}}} \underbrace{\begin{bmatrix} \triangle\boldsymbol{\omega^t} \\ \triangle\boldsymbol{\delta^t} \end{bmatrix}}_{\boldsymbol{x^t}} + \underbrace{\begin{bmatrix} -\boldsymbol{M^{-1}B}_{\mathrm{GI}} \\ \boldsymbol{0_n} \end{bmatrix}}_{\boldsymbol{\bar{B}_u}} \boldsymbol{u^t} + \underbrace{\begin{bmatrix} -\boldsymbol{M^{-1}} \\ \boldsymbol{0_n} \end{bmatrix}}_{\boldsymbol{\bar{B}_d}} \underbrace{\triangle\boldsymbol{P^t}}_{\boldsymbol{d^t}} \tag{4.12}$$

where $\triangle\boldsymbol{\delta} \in \mathbb{R}^n$ is the rotor angles deviation, $\triangle\boldsymbol{\omega} \in \mathbb{R}^n$ is the rotor speed deviation, $\boldsymbol{M} = \mathrm{diag}(m_1, \ldots, m_n) \in \mathbb{R}^{n\times n}$, $\boldsymbol{D} = \mathrm{diag}(d_1, \ldots, d_n) \in \mathbb{R}^{n\times n}$, $\triangle\boldsymbol{P^t} \in \mathbb{R}^n$ is vector of all power deviations which comes from the disturbances and noises in the system, denoted by $\boldsymbol{d}^t$.

Since the IPC does not know the disturbance or noise impacting the system, we use a two step process to solve the optimization problem. First, we ignore the disturbance term such that the IPC's model of the system is:

$$\underbrace{\begin{bmatrix}\triangle\boldsymbol{\omega}^{t+1}\\ \triangle\boldsymbol{\delta}^{t+1}\end{bmatrix}}_{\boldsymbol{x}^{t+1}} = \underbrace{\begin{bmatrix}-\boldsymbol{M}^{-1}\boldsymbol{D} & -\boldsymbol{M}^{-1}\boldsymbol{B}_{ee}\\ \boldsymbol{I}_n & \boldsymbol{0}_n\end{bmatrix}}_{\bar{\boldsymbol{A}}}\underbrace{\begin{bmatrix}\triangle\boldsymbol{\omega}^{t}\\ \triangle\boldsymbol{\delta}^{t}\end{bmatrix}}_{\boldsymbol{x}^{t}} + \underbrace{\begin{bmatrix}-\boldsymbol{M}^{-1}\boldsymbol{B}_{eI}\\ \boldsymbol{0}_n\end{bmatrix}}_{\bar{\boldsymbol{B}}}\boldsymbol{u}^t. \tag{4.13}$$

Note that in this case the IPC's model of the system is actually wrong since the disturbances are not modeled. It turns out that this model is still useful, since the measurements are updated every time the MPC problem is solved, and this compensates for using a wrong model. In the rest of this section, we focus on solving the optimization problem using the model in (4.13) since it illustrates our methodology. Of course, when the measurement noise in the system is large or not every bus is equipped with wide-area measurement devices, it becomes necessary to explicitly estimate the mismatch between the model and the actual system. We do so in section 4.4.

We reformulate the objective function in terms of the network model in (4.13) by defining the output of the linearized model as the frequency deviation $\triangle\boldsymbol{\omega}^t$:

$$\boldsymbol{y}^t = \underbrace{\begin{bmatrix}\boldsymbol{I}_n & \boldsymbol{0}_n\end{bmatrix}}_{\boldsymbol{C}}\boldsymbol{x}^t = \triangle\boldsymbol{\omega}^t \tag{4.14}$$

such that the ROCOF becomes:

$$\triangle\boldsymbol{y}^t = \frac{1}{h}\left[\boldsymbol{y}^t - \boldsymbol{y}^{t-1}\right] = \frac{1}{h}\left[\triangle\boldsymbol{\omega}^t - \triangle\boldsymbol{\omega}^{t-1}\right] \tag{4.15}$$

The IPC optimization algorithm in (5.8) without the power limit constraint (5.8e) and total energy constraints (5.8f) can now be written as a linear quadratic programming problem:

$$\begin{aligned}\underset{\boldsymbol{u}^t}{\text{Min.}}\ J &= \frac{1}{2}\sum_{t=0}^{N-1}\left[{\boldsymbol{y}^t}^T\boldsymbol{Q_1}\boldsymbol{y}^t + {\triangle\boldsymbol{y}^t}^T\boldsymbol{Q_2}\triangle\boldsymbol{y}^t\right]\\ \text{s.t.}\quad \boldsymbol{x}^{t+1} &= \bar{\boldsymbol{A}}\boldsymbol{x}^t + \bar{\boldsymbol{B}}\boldsymbol{u}^t\\ \boldsymbol{y}^t &= \boldsymbol{C}\boldsymbol{x}^t.\end{aligned} \tag{4.16}$$

This can be written in matrix form for N time step ahead as:

$$\underset{\boldsymbol{u}}{\text{Min.}}\ J = \frac{1}{2}\boldsymbol{x^0}^{\boldsymbol{T}}\boldsymbol{G}\boldsymbol{x^0} + \boldsymbol{x^0}^{\boldsymbol{T}}\boldsymbol{F}\boldsymbol{u} + \frac{1}{2}\boldsymbol{u}^{\boldsymbol{T}}\boldsymbol{H}\boldsymbol{u}. \tag{4.17}$$

where $\boldsymbol{H}$ and $\boldsymbol{F}$ are constant matrices depending on $\bar{\boldsymbol{A}}$ and $\bar{\boldsymbol{B}}$.

Not surprisingly, the optimal solution to this unconstrained problem is linear in the starting point $\boldsymbol{x}^0$:

$$\boldsymbol{u}^* = -\boldsymbol{H}^{-1}\boldsymbol{F}^{\boldsymbol{T}}\boldsymbol{x^0}. \tag{4.18}$$

This solution can be interpreted as a linear policy, where the optimal action is determined as a linear function of the current state information (see appendix A.1 for derivation of $\bar{\boldsymbol{A}}$, $\bar{\boldsymbol{B}}$ and $\boldsymbol{u}^*$).

4.3.3 Constrained Linearized Optimization Problem

In the presence of constraints, we need to solve a quadratic programming optimization problem with linear constraints of the form:

$$\begin{aligned} &\underset{\boldsymbol{u}}{\text{Min.}}\ J = \frac{1}{2}\boldsymbol{x^0}^{\boldsymbol{T}}\boldsymbol{G}\boldsymbol{x^0} + \boldsymbol{x^0}^{\boldsymbol{T}}\boldsymbol{F}\boldsymbol{u} + \frac{1}{2}\boldsymbol{u}^{\boldsymbol{T}}\boldsymbol{H}\boldsymbol{u} \\ &\text{s.t.} \quad \boldsymbol{L}\boldsymbol{u} \leq \boldsymbol{W} + \boldsymbol{V}\boldsymbol{x^0}, \end{aligned} \tag{4.19}$$

where $\mathbf{L}, \boldsymbol{W}$ and $\boldsymbol{V}$ depends on the constraint being considered. In this paper, we consider constraints on the power output at each time step (5.8e) and constraints on the total energy available to provide frequency control (5.8f).

Power Output Constraint

In practical considerations, there can be a limit on the amount of instantaneous power that can be drawn from the IBR due to factors such as the distance to the maximum power tracking operating point, the current ratings and switching speed of some power electronics components, and also power capability or C-rate of a battery.

The transformation of the minimum and maximum instantaneous power limit from $P^t_{\text{ibr,min},k} \leq P^t_{\text{ibr},k} \leq P^t_{\text{ibr,max},k}$ to the linear constraint in (5.28) involves writing the linearized power output of the k^{th} IBR at time step t in terms of the control variable $\boldsymbol{u}^t$ and states $\boldsymbol{x}^t$, and then stacking them in matrix form for the N control horizon.

The linearized output power $P^t_{\text{ibr},k}$ is written in terms of the power flow to generators and to other IBRs as:

$$\begin{aligned} P^t_{\text{ibr},k} &= \sum_{k\sim i, k\in\mathcal{I}, i\in\mathcal{G}} b_{ki}(u^t_k - \triangle\delta^t_i) + \sum_{k\sim j, j,k\in\mathcal{I}} b_{kj}(u^t_k - u^t_j) \\ &= -\sum_{k\sim i, i\in\mathcal{G}} b_{ki} \triangle \delta^t_i + \sum_{k\in\mathcal{I}} b_{kk} u^t_k - \sum_{k\sim j, j\in\mathcal{I}} b_{kj} u^t_j, \end{aligned} \tag{4.20}$$

which can be written in matrix form as:

$$P^t_{\text{ibr},k} = \begin{bmatrix} \boldsymbol{0_n} & -[\boldsymbol{B}]_{\boldsymbol{ki}} \end{bmatrix} \boldsymbol{x^t} + \begin{bmatrix} -[\boldsymbol{B}]_{\boldsymbol{kj}} & [\boldsymbol{B}]_{\boldsymbol{kk}} \end{bmatrix} \boldsymbol{u^t} \tag{4.21}$$

Stacking (5.22) for a N time horizon and writing the linear system dynamics in term of the initial state results in a form:

$$\boldsymbol{P}_{\text{ibr},\boldsymbol{k}} = \boldsymbol{B}_{\text{p}1}\boldsymbol{x^0} + \boldsymbol{B}_{\text{p}2}\boldsymbol{u}, \tag{4.22}$$

which can finally be written in the linear constraint form of (5.28) as:

$$\underbrace{\begin{bmatrix} -\boldsymbol{B}_{\text{p}2} \\ \boldsymbol{B}_{\text{p}2} \end{bmatrix}}_{\boldsymbol{L}} \boldsymbol{u} \leq \underbrace{\begin{bmatrix} -\boldsymbol{P}_{\text{ibr, min}} \\ \boldsymbol{P}_{\text{ibr, max}} \end{bmatrix}}_{\boldsymbol{W}} + \underbrace{\begin{bmatrix} \boldsymbol{B}_{\text{p}1} \\ -\boldsymbol{B}_{\text{p}1} \end{bmatrix}}_{\boldsymbol{V}} \boldsymbol{x^0}. \tag{4.23}$$

See appendix A.3 for derivation.

Total Energy Constraint

This constraint occurs when there is a limit on the energy capacity of the IBR as in the case of a battery. For this constraint to be fully satisfied, the total energy not only at the end of the control horizon but also at each rolling sum of the consecutive time step should be less than the maximum energy capacity.

As with the power output constraint, the total energy constraint $\sum_{t=1}^{N} P^{t}_{\text{ibr,k}} \leq E^{t}_{\text{ibr, tot},k}$ can also be written in the linear constraint form in (5.28) by taking the rolling sum over the inverter power output matrix in (4.22). This results in another matrix of the form:

$$\boldsymbol{E}_{\text{ibr},\boldsymbol{k}} = \boldsymbol{B}_{\text{e}1}\boldsymbol{x}^{\boldsymbol{0}} + \boldsymbol{B}_{\text{e}2}\boldsymbol{u}. \tag{4.24}$$

To avoid a sudden decline in the power output when the maximum available energy limit is reached, a rate constraint can be added to the power output decline between a specified consecutive time step. This can also be represent in the form of (5.28) by taking a one time step difference of the IBR power output matrix in (4.22), that is, a difference between the next time step and current time step IBR power output. This results in a matrix of the form:

$$\triangle\boldsymbol{P}_{\text{ibr},\boldsymbol{k}} \triangleq \boldsymbol{\epsilon} = \boldsymbol{B}_{\text{r}1}\boldsymbol{x}^{\boldsymbol{0}} + \boldsymbol{B}_{\text{r}2}\boldsymbol{u}. \tag{4.25}$$

Equation (4.24) and (4.25) can finally be written in the linear constraint form of (5.28) as

$$\underbrace{\begin{bmatrix} \boldsymbol{B}_{\text{e}2} \\ \boldsymbol{B}_{\text{r}2} \end{bmatrix}}_{\boldsymbol{L}} \boldsymbol{u} \leq \underbrace{\begin{bmatrix} \boldsymbol{E}_{\text{ibr, tot}} \\ \boldsymbol{\epsilon} \end{bmatrix}}_{\boldsymbol{W}} + \underbrace{\begin{bmatrix} -\boldsymbol{B}_{\text{e}1} \\ -\boldsymbol{B}_{\text{r}1} \end{bmatrix}}_{\boldsymbol{V}} \boldsymbol{x}^{\boldsymbol{0}}\boldsymbol{.} \tag{4.26}$$

where $\boldsymbol{\epsilon}$ is a vector of IBR power output rate limit for each one time step difference. See appendix A.4 for derivation.

Even with constraints, a linear quadratic program can be solved extremely efficiently for systems with thousands of variables and constraints [126]. Again, to actually implement the controller, we compute and set the power output of the IBRs.

4.4 *State Estimation and Limited Communication*

In section 4.3, the IPC controller was designed using the reduced linearized model of the network as in (4.13) and under the assumption of a full state measurement. When operating this controller in a realistic setting, we would want the controller to be robust against issues such as model mismatch, that is, the difference between the actual system model and the linearized model used by the IPC; noisy measurements, and incomplete measurements because of limited communication between buses.

We address these issues in this section by integrating an observer into the IPC controller system according to Fig. 4.4 to enable the controller estimate a better model of the system from the received measurements.

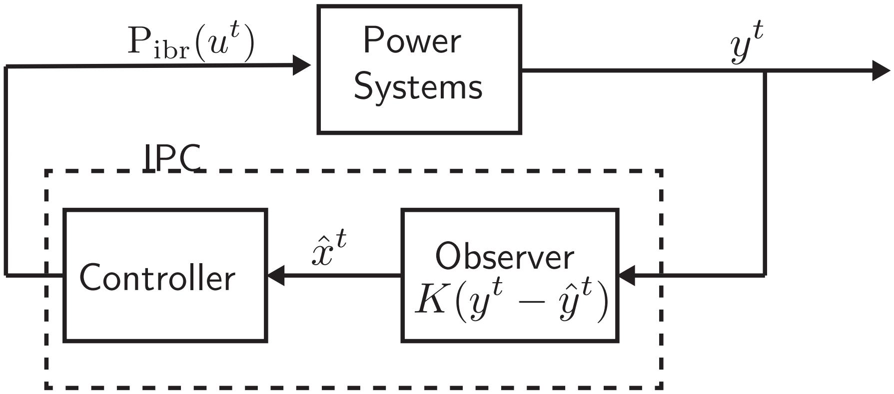

Figure 4.4: Block diagram showing the operation of an observer integrated IPC in a power systems. The state measurements received by the observer in addition to the predicted state by the model is used to estimate the true state of the system.

Let the dynamics of the actual power systems governed by (5.1) be represented concisely as:

$$\begin{aligned} \boldsymbol{x}^{t+1} &= \boldsymbol{f}(\boldsymbol{x}^t, \boldsymbol{u}^t) \\ \boldsymbol{y}^t &= \boldsymbol{g}(\boldsymbol{x}^t, \boldsymbol{u}^t). \end{aligned} \tag{4.27}$$

A simple discrete observer model design [127] for the system in (5.4) can be written as:

$$\begin{aligned} \hat{\boldsymbol{x}}^{t|t} &= \hat{\boldsymbol{x}}^{t|t-1} + \boldsymbol{K}(\boldsymbol{y}^t - \hat{\boldsymbol{y}}^t) \\ \hat{\boldsymbol{y}}^t &= \boldsymbol{C}\hat{\boldsymbol{x}}^{t|t-1}, \end{aligned} \tag{4.28}$$

where the notation $\hat{\boldsymbol{x}}^{t|\tau}$ means the prediction of $\boldsymbol{x}^t$ made at time τ. Therefore the variables with $\hat{\boldsymbol{x}}^{t|t}$ is the updated observer state prediction based on new measurement $\boldsymbol{y}^t$, $\hat{\boldsymbol{x}}^{t|t-1}$ is the observer state prediction of the current time step using measurements from the previous time step, and $\boldsymbol{K}$ is a gain chosen such that the error between the measured and predicted state $\boldsymbol{y}^t - \hat{\boldsymbol{y}}^t$ is quickly driven to zero.

4.4.1 State and Disturbance Estimation

To estimate the state and disturbance in a noisy system with model mismatch and other forms of disturbance, we redefine $\boldsymbol{d}^t$ as a vector of all disturbances. We then integrate an input/output constant disturbance model [127] into the IPC system model in (5.11) to obtain:

$$\begin{aligned} \hat{\boldsymbol{x}}^{t+1} &= \bar{\boldsymbol{A}}\hat{\boldsymbol{x}}^t + \bar{\boldsymbol{B}}_u\boldsymbol{u}^t + \bar{\boldsymbol{B}}_d\hat{\boldsymbol{d}}^t \\ \hat{\boldsymbol{d}}^{t+1} &= \hat{\boldsymbol{d}}^t \\ \hat{\boldsymbol{y}}^t &= \boldsymbol{C}\hat{\boldsymbol{x}}^t + \boldsymbol{C}_d\boldsymbol{d}^t, \end{aligned} \tag{4.29}$$

where the disturbance $\hat{\boldsymbol{d}}$ is modeled as a constant disturbance for the control period. Equation (4.29) can then be written in an augmented form as:

$$\begin{aligned} \begin{bmatrix} \hat{\boldsymbol{x}}^{t+1} \\ \hat{\boldsymbol{d}}^{t+1} \end{bmatrix} &= \begin{bmatrix} \bar{\boldsymbol{A}} & \bar{\boldsymbol{B}}_d \\ \boldsymbol{0} & \boldsymbol{I} \end{bmatrix} \begin{bmatrix} \hat{\boldsymbol{x}}^t \\ \hat{\boldsymbol{d}}^t \end{bmatrix} + \begin{bmatrix} \bar{\boldsymbol{B}}_u \\ \boldsymbol{0} \end{bmatrix} \boldsymbol{u}^t \\ \hat{\boldsymbol{y}}^t &= \begin{bmatrix} \boldsymbol{C} & \boldsymbol{C}_d \end{bmatrix} \begin{bmatrix} \hat{\boldsymbol{x}}^t \\ \hat{\boldsymbol{d}}^t \end{bmatrix}. \end{aligned} \tag{4.30}$$

The predicted augmented state and disturbance can then be estimated using the observer model in (5.5) as:

$$\begin{bmatrix} \hat{\boldsymbol{x}}^{t|t} \\ \hat{\boldsymbol{d}}^{t|t} \end{bmatrix} = \begin{bmatrix} \hat{\boldsymbol{x}}^{t|t-1} \\ \hat{\boldsymbol{d}}^{t|t-1} \end{bmatrix} + \boldsymbol{K} \left(\boldsymbol{y}^t - \begin{bmatrix} \boldsymbol{C} & \boldsymbol{C}_d \end{bmatrix} \begin{bmatrix} \hat{\boldsymbol{x}}^{t|t-1} \\ \hat{\boldsymbol{d}}^{t|t-1} \end{bmatrix} \right) \tag{4.31}$$

where $\boldsymbol{K}$ is the gain matrix for the augmented state and disturbance variable. For simplicity, we adopt a fixed gain structure for the gain matrix $\boldsymbol{K}$.

This observer integrated IPC model in (5.14) and (5.15) replaces the linear model in (4.13), with the augmented state used in place of the original states $\boldsymbol{x^t}$ and the rest of the algorithm follows through for the constrained and unconstrained case.

4.4.2 Limited Communication

While wide area measurement system (WAMS) data, consisting of sensors and communication infrastructures, is becoming increasingly available [128] in modern power systems, it will still take some time before full communication coverage across the network can be realized. Even with these types of infrastructure, there is always the possibility of communication issues.

To tackle the issue of limited communication, we assume that the initial state measurements of the generators is available. For example, these can be conveyed using the existing SCADA system every two to four seconds. The augmented state and disturbance estimate in (5.15) is then used in estimating the full state and disturbance. The only difference is in the gain used since the structure and dimension of the gain $\boldsymbol{K}$ will change depending on the number of generators with available state information, that is, the dimension of $\boldsymbol{y^t}$. As with the state and disturbance estimation case, these gains are also selected as fixed gains. More sophisticated gain structures will be explored in future works.

The key idea here is that the mismatch between the evolved initial state of the generators with limited communication and what the state should be if there was communication is reflected as a disturbance in the network and can be estimated using the measurements from available generators.

4.5 Case Studies

In this section, we validate the performance and versatility of the IPC controller by testing it on the IEEE WECC 3-machine 9-bus system and IEEE New England 10-machine 39-bus (NE39) system used for power systems dynamics stability studies [123, 129]. We study scenarios including constraints on the power and energy output of the IBR, noisy measurements and limited communication. Under each scenario, a large disturbance in the form of a partial generating capacity loss is applied to a generator in the network to initiate an event that can lead to a marked frequency decline. The performance metrics for the controller is its ability to maintain the frequency deviation within a small range, quickly recovering to the nominal frequency value and limiting the ROCOF.

4.5.1 IEEE WECC 3 Machine 9-Bus System

We validate the proposed IPC controller by first testing it on the IEEE WECC 3-machine 9-bus (3m9b) system, a popular system used in stability studies. We transform the network into a low-inertia network by replacing generator G3 at bus 3 with an IBR (either solar or wind but coupled with energy storage) total aggregated capacity equal to the replaced generator as shown in Fig. 4.5. The network is then reduced to an equivalent network by eliminating the passive and static load buses, that is, buses 4 - 9, using Kron reduction. A disturbance of 60% loss of capacity is applied to the second generator (*G2*) located at bus 2 from 0.5 to 5 seconds.

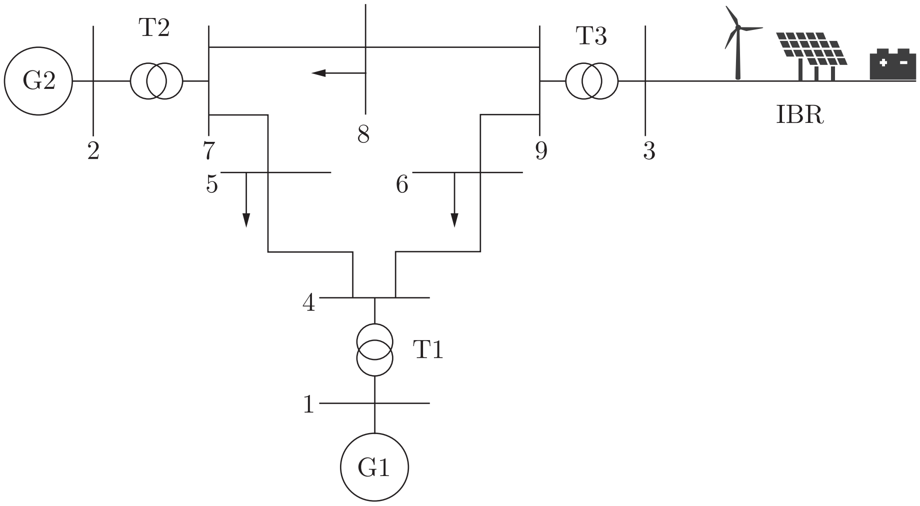

Figure 4.5: IEEE WECC 3-machine 9-bus system schematic with generator G3 at bus 3 replaced with an IBR of equal aggregated capacity.

The performance of the proposed controller is compared to that of an optimally tuned VSM controller discussed in Section 4.2.3 with computed optimal gain coefficients of $K_{\mathrm{m}} = 11.22$ and $K_{\mathrm{d}} = 60.20$ according to [79]. Note that the VSM controllers are not optimized for power or energy limits and simply saturates when the computed IBR output power exceeds its limits.

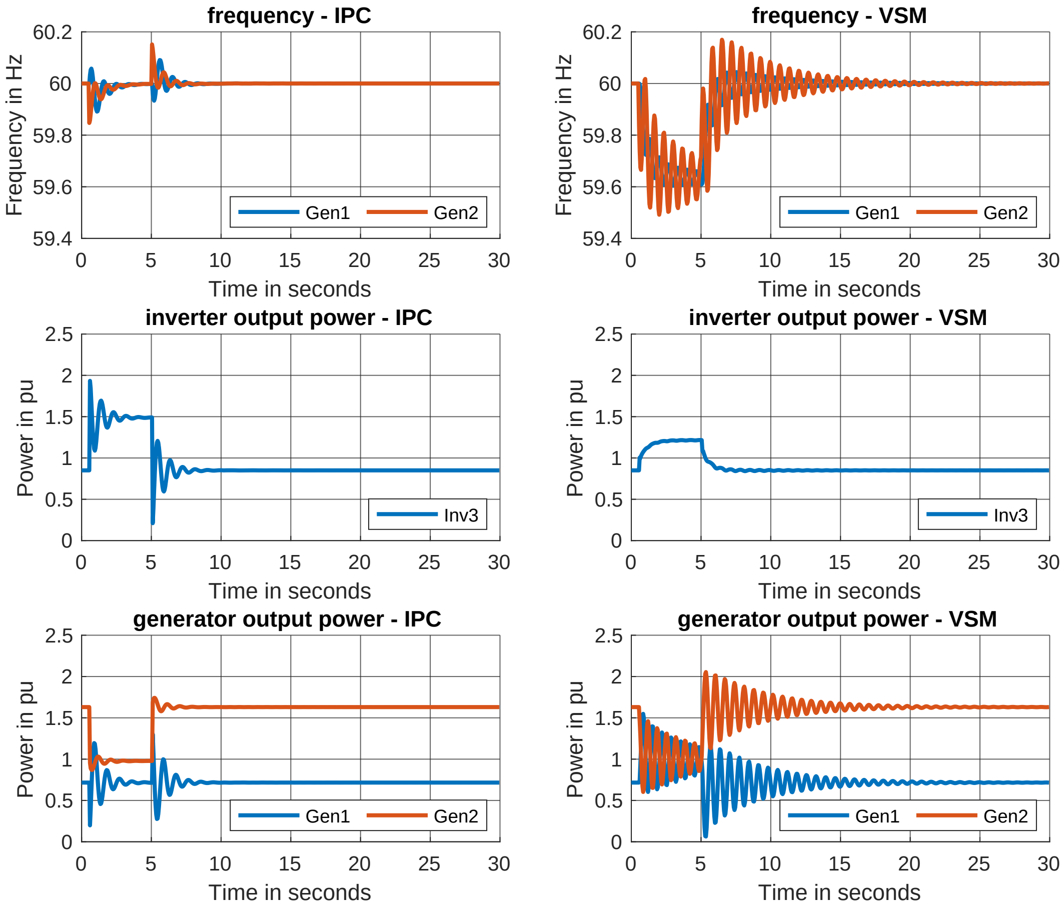

Figure 4.6: Comparison of IPC and VSM control strategies for an unconstrained scenario in a 3m9b network. The IPC outperforms the VSM in keeping the frequencies within limits by utilizing the unlimited resources available to it.

Fig. 4.6 shows the generator frequencies and IBR output power of the unconstrained IPC and VSM, that is, under the conditions of unlimited IBR power and energy capacities. The proposed IPC controller is able to optimally determine the required amount of active power to ensure a suitable frequency response. Specifically, the IPC keeps the frequencies within about 0.2 Hz of nominal, while the frequency varies by more than 0.6 Hz under the VSM controller. This shows that even though unconstrained amount of power is available to both controllers, the look-ahead and adaptive nature of the proposed controller enables it outperform the VSM.

It's interesting to note that Fig. 4.6 also implies that the performance of an IBR is strictly better than that of a synchronous generator, since the VSM acts as a synchronous generator with optimized inertia and droop coefficients. Therefore, replacing conventional generators by renewable resource does not necessarily mean the frequency response is worse. Rather, if the resource can be optimized, then much better responses are possible.

Power and Energy Constraints

Figs. 4.7 and 4.8 shows the generator frequencies and IBR output power for a power and energy constrained IPC and VSM, respectively. The maximum power limits at each time step was set to 1.5pu while the total energy limit was set to 20pu.

Compared to the VSM, the IPC is still able to limit the frequency deviation to about 0.2 Hz for the limited power case and 0.4Hz for the limited energy case while keeping the system frequency from rapid oscillation as seen in the VSM case. The IPC is able to integrate the resource constraints into its optimization and look-ahead to determine the best control strategy but similar performance is very hard to achieved using a VSM controller since it lacks an explicit optimization step to deal with hard constraints. Also, in the power constrained scenario, because the VSM relies on a second order control structure and local state information, it is not able to maximize the available resource as its active power output is still less than the power limit.

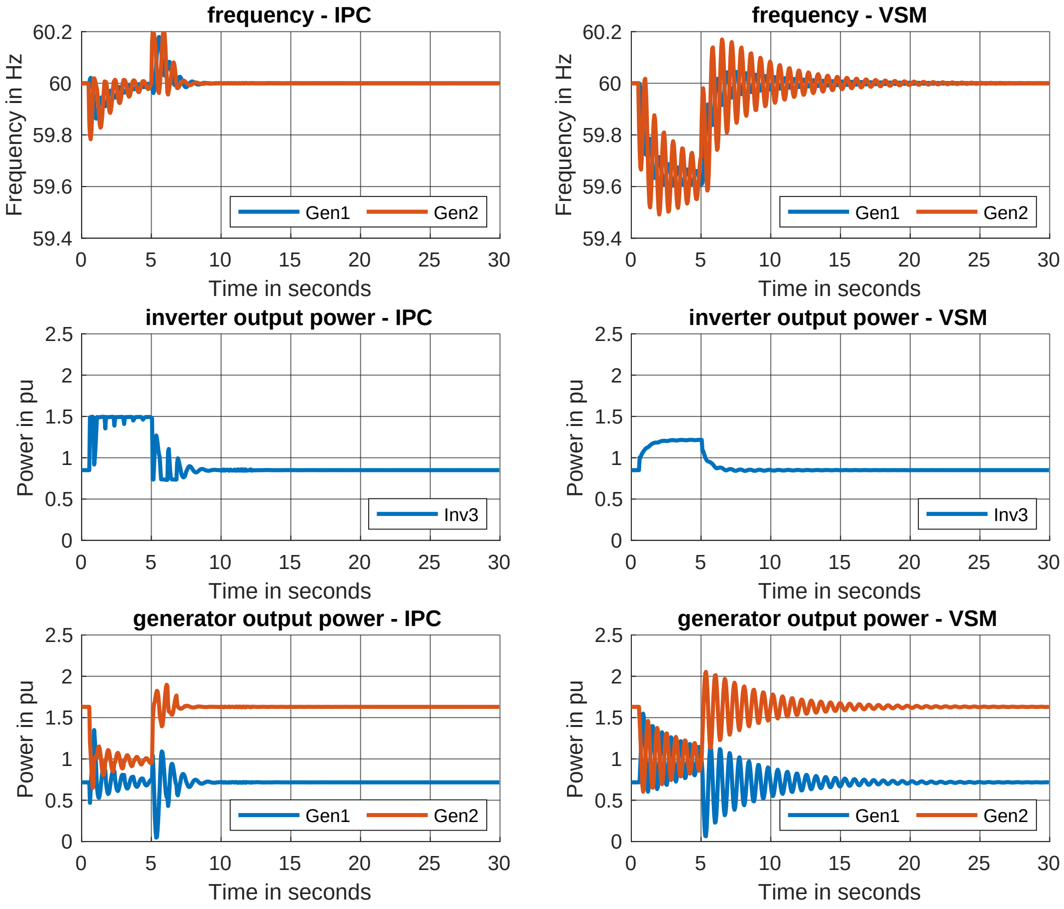

Figure 4.7: Comparison of IPC and VSM control strategies under a power constraint of 1.5 p.u. in the 3m9b network. The IPC manages to keep the frequencies deviation within reasonable limits while respecting the power limits compared to the VSM which does not utilize the resources available to it up to the power limit.

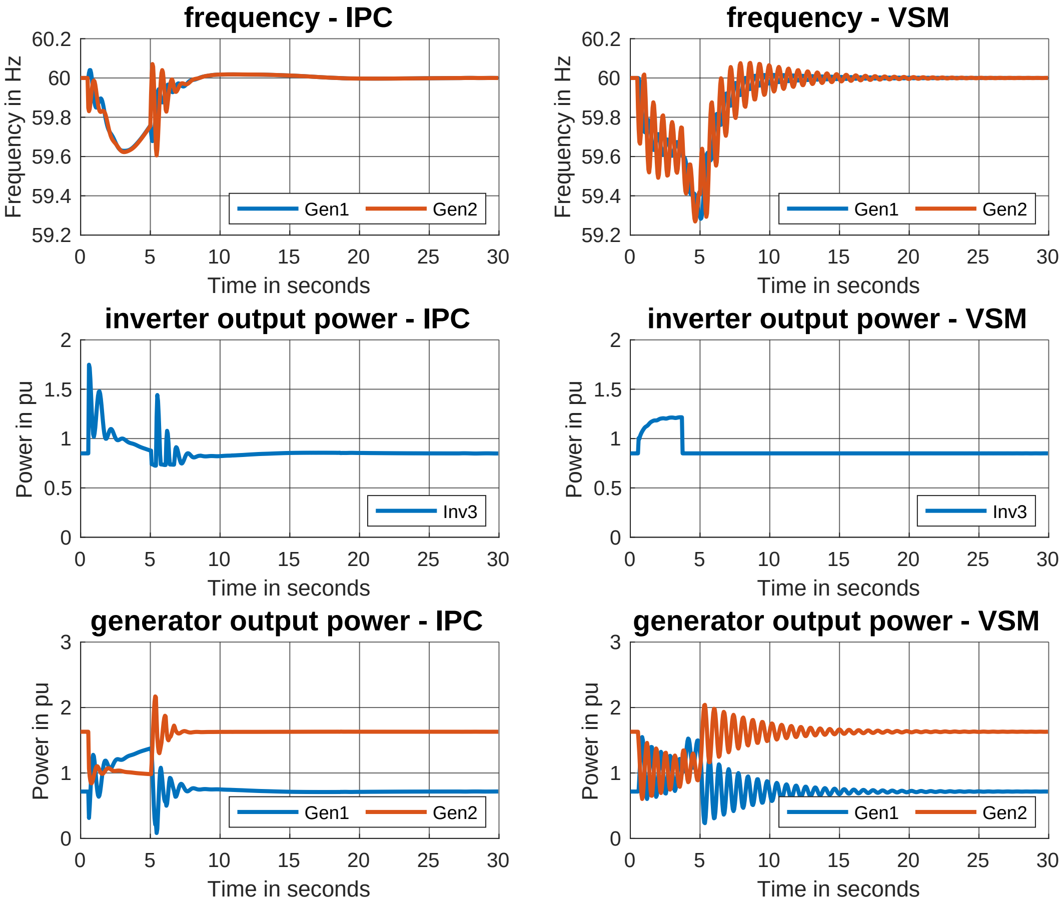

Figure 4.8: Comparison of IPC and VSM control strategies under an energy constraint of 20 p.u. in the 3m9b network. The IPC controller with its adaptive look ahead properties is able to prevent large frequency excursion compared to the VSM.

Robustness of the Controller

Fig. 4.9 demonstrates the robustness of the IPC controller to noise, model mismatch and external disturbances to the system with the incorporation of the observer model in (5.15). According to PMU standards in [130], the total vector error of a PMU measurement should be $< 1\%(\sim 40$dB signal-to-noise ration (SNR)) while [131] suggested that the SNR of PMU measurements can vary between 30 to 65 dB. We therefore model the effect of noisy measurements adding noise to create SNRs of 30dB and 50dB, respectively. These represent the worst-case and an average-case SNR scenarios. Fig. 4.9 shows that noise has very little impact to the performance of the IPC (even under only 30 dB of SNR). Of course, the observer plays an important role in this robustness to noisy measurements.

4.5.2 IEEE New England 10 Machine 39-Bus System

We further validate the proposed IPC controller on a larger system, the IEEE New England 39-bus system, and verify its ability to function effectively even in a limited communication scenario. The network is transformed into a low-inertia network by removing the interconnection to the rest of the US network and replacing generator 5 at bus 34 with an IBR (either solar or wind but coupled with energy storage) total aggregated capacity equal to the replaced generator as shown in Fig. 5.3, and reduced to an equivalent network using Kron reduction. The disturbance of 60% loss of capacity is applied to the fourth generator ($G4$) located at bus 33 from 0.5 to 5 seconds.

The performance of the proposed controller is compared to that of an optimally tuned VSM controller discussed in Section 4.2.3 with computed optimal gain coefficients of $K_\mathrm{m} = 201.7$ and $K_\mathrm{d} = 520$ according to [79]. Note that the VSM controllers are not optimized for power or energy limits and simply saturates when the computed IBR output power exceeds its limits.

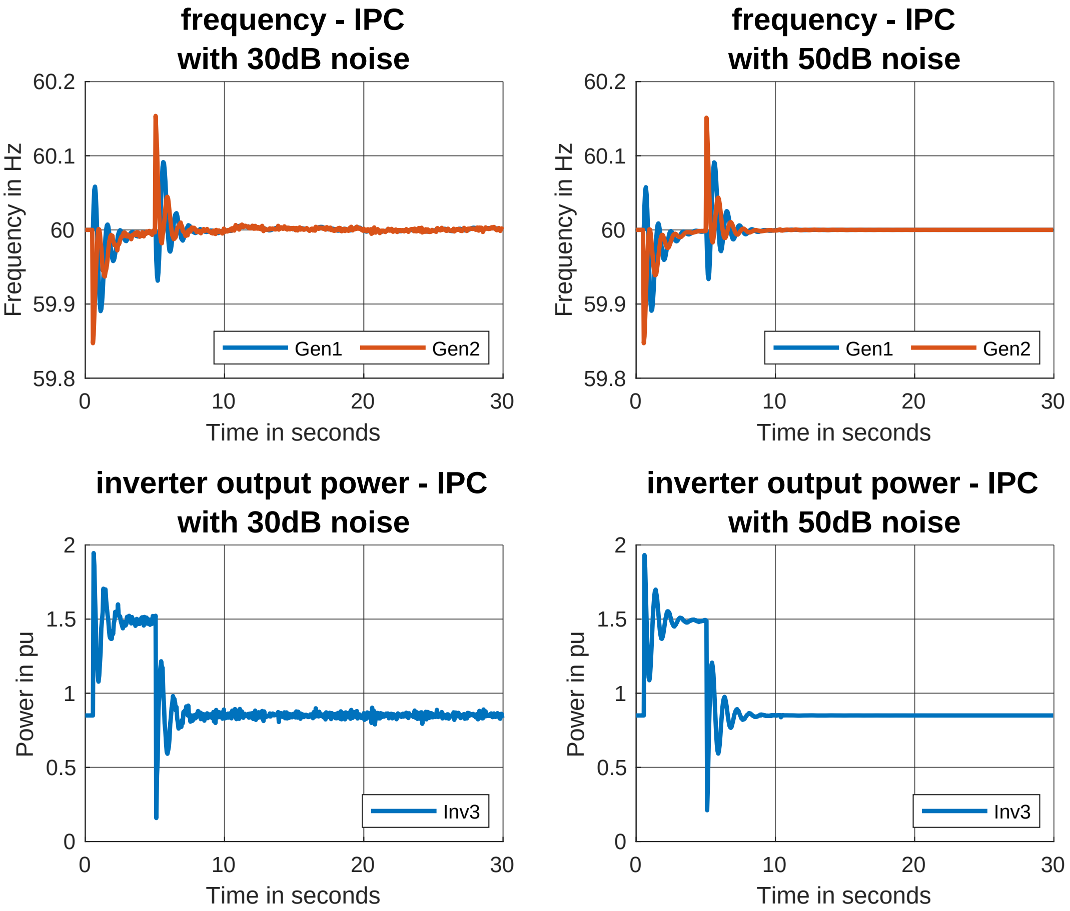

Figure 4.9: Robust IPC under SNR of 30dB and 50dB in the 3m9b network. The IPC controller is still able achieve a smooth response while keeping the frequency within limit even in a worst-case noise scenario.

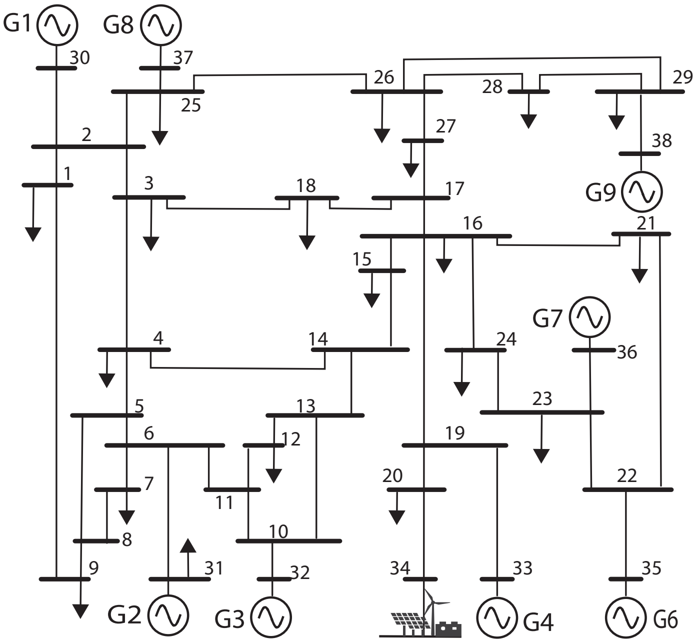

Figure 4.10: New England 39-bus system schematic with generator 5 at bus 34 replaced with an IBR of equal aggregated capacity.

Unconstrained Scenario

Fig. 4.11 shows the generator frequencies and IBR output power of the unconstrained IPC and VSM, that is, under the conditions of unlimited IBR power and energy capacities. For a clearer viewing, only the frequency response of the second (slack), fourth (disturbed), seventh and ninth generator are shown. The proposed IPC controller is able to optimally determine the required amount of active power to ensure a suitable frequency response. Specifically, the IPC keeps the frequencies within about 0.2 Hz of nominal and restore the frequency to its nominal value, while under the VSM controller, the frequency varies by about 0.4 Hz and oscillates longer due to the inability of the VSM to anticipate the impact of the inter-area swing, that is a groups of generators swinging against each other [132].

This shows that even though an unconstrained amount of power is available to both controllers, the look-ahead and adaptive nature of the proposed IPC controller enables it outperform the VSM by utilizing the resources available to satisfy the given objective. It overcomes

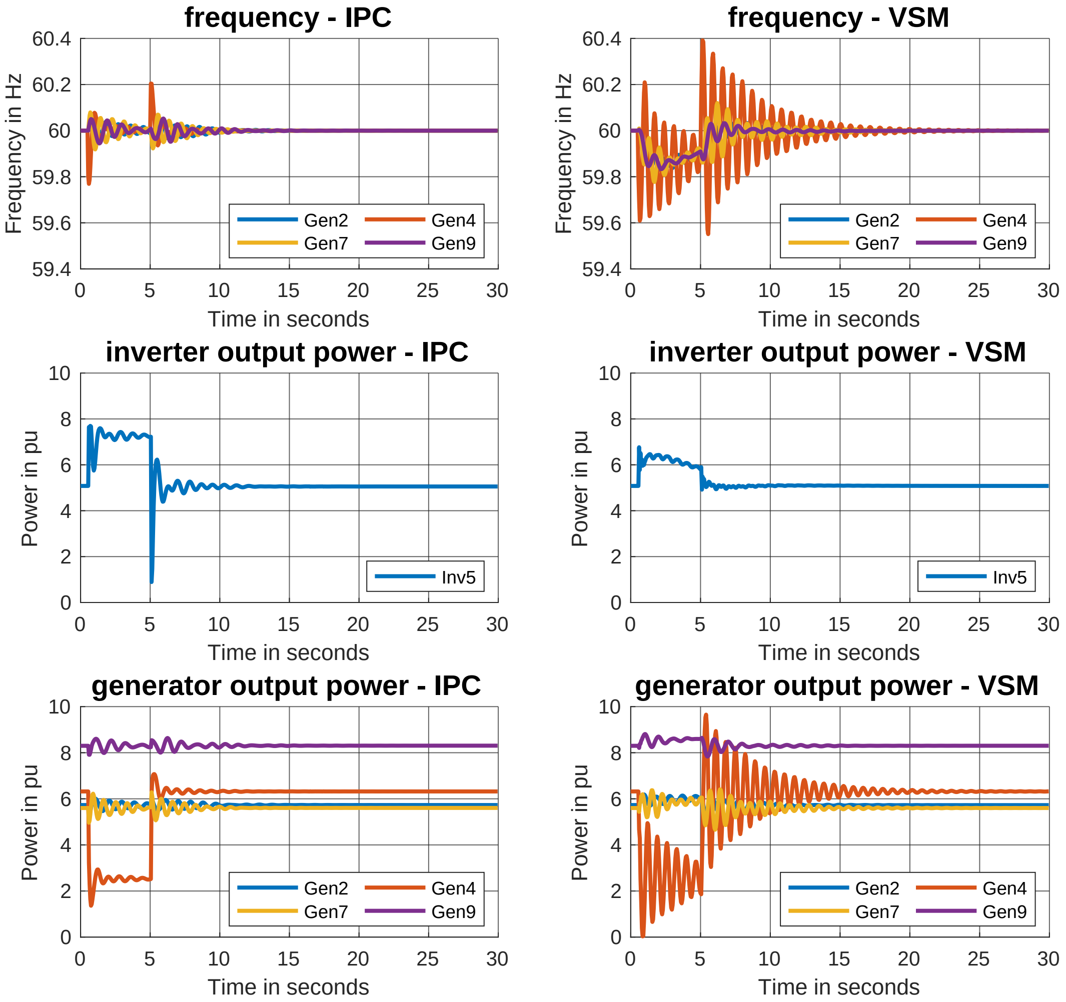

Figure 4.11: Comparison of IPC and VSM control strategies for an unconstrained scenario in a NE39 network. The plots show the frequency and generator output power for some select generators and the IBR's output power. The IPC outperforms the VSM in keeping the frequencies within limits.

a particular issue of when the local frequency measurement becomes misleading a network with different coherent areas swinging against each other. Fig. 4.12 shows the center of inertia frequency given by (4.6) when utilizing the VSM control structure compared to the true frequency of each generators, which the former is misleadingly small.

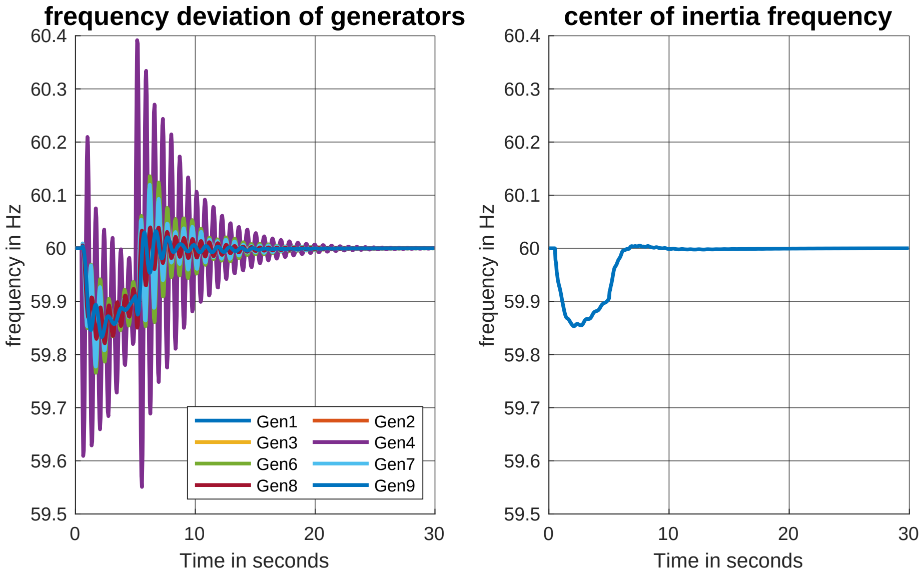

Figure 4.12: Comparison of the actual frequency of the individual generators in the NE39 network (*left*) and the inertia weighted frequency called the frequency of the center of inertia (*right*) which we take to be the local grid frequency measured for numerical simulation

As observed in the 3m9b case, Fig. 4.11 also implies that the performance of an IBR is strictly better than that of a synchronous generator, since the VSM mimics the response of a synchronous generator with optimized inertia and droop coefficients. Therefore, replacing conventional generators by renewable resource does not necessarily mean the frequency response is worse. Rather, if the resource can be optimized, then much better responses are possible.

Power and Energy Constraints

Figs. 4.13 and 4.14 shows select generators' frequency and output power, and also the IBR output power for a power and energy constrained IPC and VSM, respectively. The maximum power limits at each time step was set to 7pu while the total energy limit was set to 70pu. For a clearer viewing, only the frequency response of the second (slack), fourth (disturbed), seventh and ninth generator are shown. Compared to the VSM, the IPC is still able to limit the frequency deviation to about 0.3 Hz for the limited power case and 0.4Hz for the limited energy case while keeping the system frequency from rapid oscillation as seen in the VSM case. The IPC is able to integrate the resource constraints into its optimization and look-ahead to determine the best control strategy, but similar performance is very hard to achieved using a VSM controller since it lacks an explicit optimization step to deal with hard constraints, therefore unable to utilize the full resource at its disposal.

Robustness of the Controller

Fig. 4.15 demonstrates the robustness of the IPC controller to noise, model mismatch and external disturbances to the system with the incorporation of the observer model in (5.15). According to PMU standards in [130], the total vector error of a PMU measurement should be $< 1\%(\sim 40$dB signal-to-noise ration (SNR)) while [131] suggested that the SNR of PMU measurements can vary between 30 to 65 dB. We therefore model the effect of noisy measurements by adding noise to create SNRs of 30dB and 50dB, respectively representing the worst-case and an average-case SNR scenarios and shows that noise has very little impact to the performance of the IPC (even under 30 dB of SNR). Of course, the observer plays an important role in this robustness to noisy measurements.

Limited Communication

We further test the performance of the IPC under 2 limited communication scenario. In scenario A - partial communication scenario, we assume that measurements can be received from the generators colored green (G3, G4, G6, and G7) while only initial state measurements

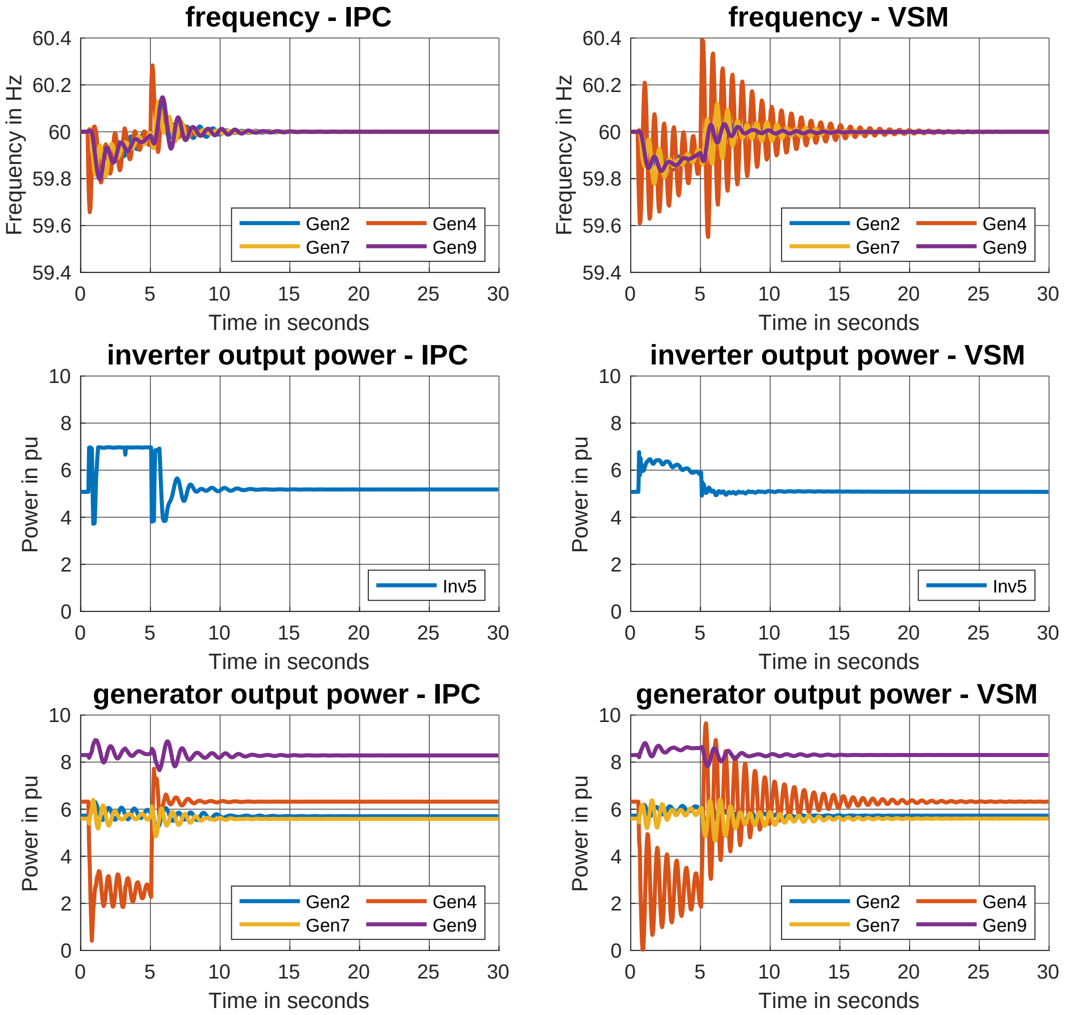

Figure 4.13: Comparison of IPC and VSM control strategies for a power constrained scenario in a NE39 network. The IPC controller is able to adaptively change its power output to minimize frequency deviations while respecting the power limits

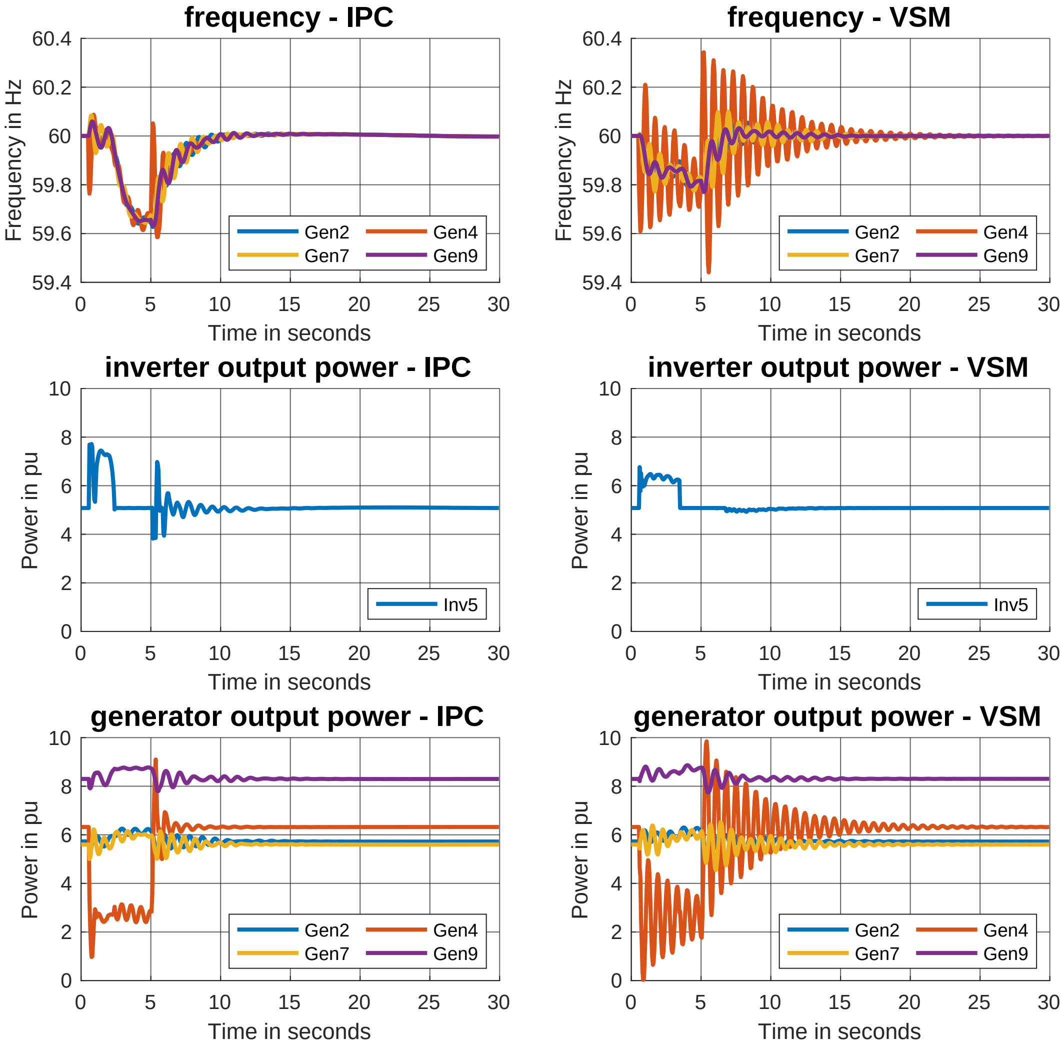

Figure 4.14: Comparison of IPC and VSM control strategies for an energy constrained scenario in a NE39 network. The IPC controller is also able to adaptively change its power output to ensure that the energy limits over its operation horizon are respected.

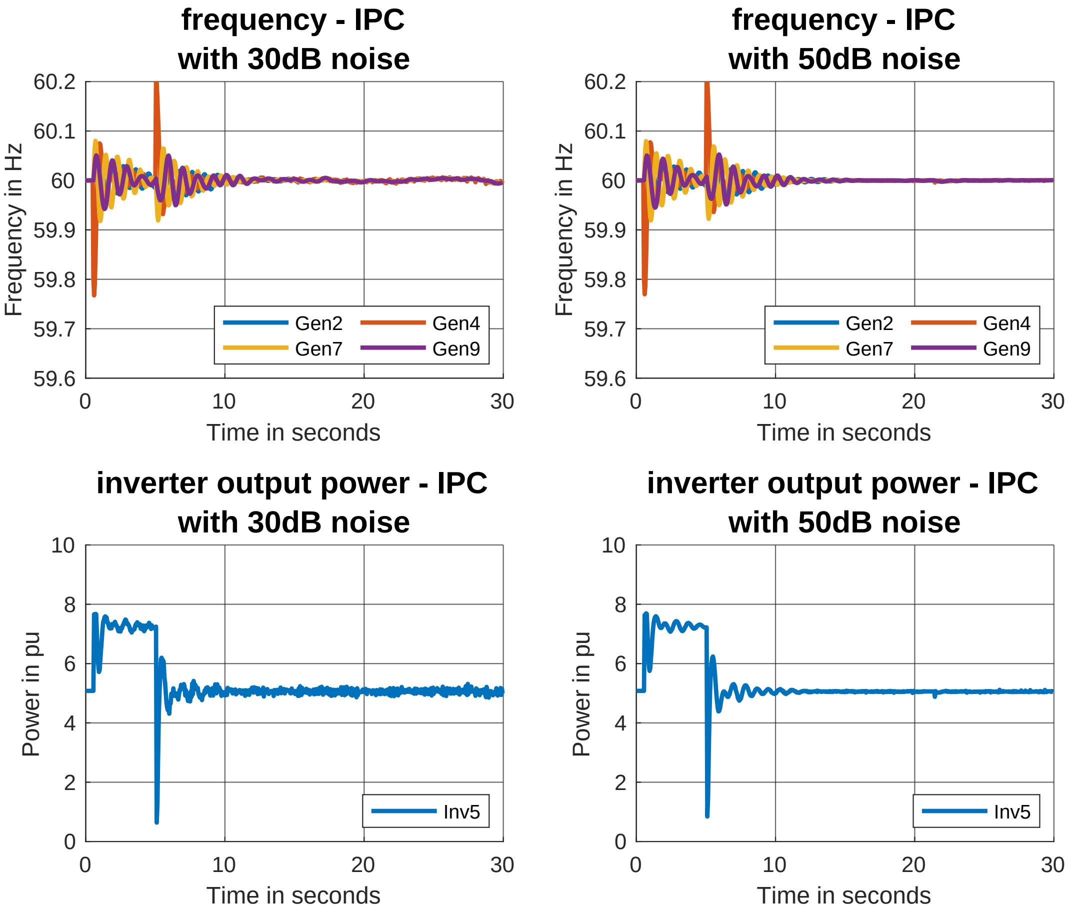

Figure 4.15: Robust IPC under SNR of 30dB and 50dB in a NE39 network. The IPC controller is still able achieve a smooth response while keeping the frequency within limit even in a worst-case noise scenario.

is received from the generators colored red (G1, G2, G8 and G9) in Fig. 4.16. This case represents a setting when the faulted generator (G4) is able to communicate with the inverter. In scenario B - no-communication scenario, we assume a case where we cannot communicate with any of the generators after the initial state communication but we instead utilize the local measurement of the system states which we assume to be the averaged value of the states at each time step. Under this scenario, the IPC controller uses these local measurements as the states of each of the generators and the control algorithm proceeds as normal. The left-side plot of Fig. 4.17 shows the IPCs performance under the partial communication scenario. By communicating with some buses, the IPC is able to reconstruct enough of the system-level information to make the computations at the IPC useful. The right-side plot of Fig. 4.17 shows the IPCs performance under the no-communication scenario, where none of

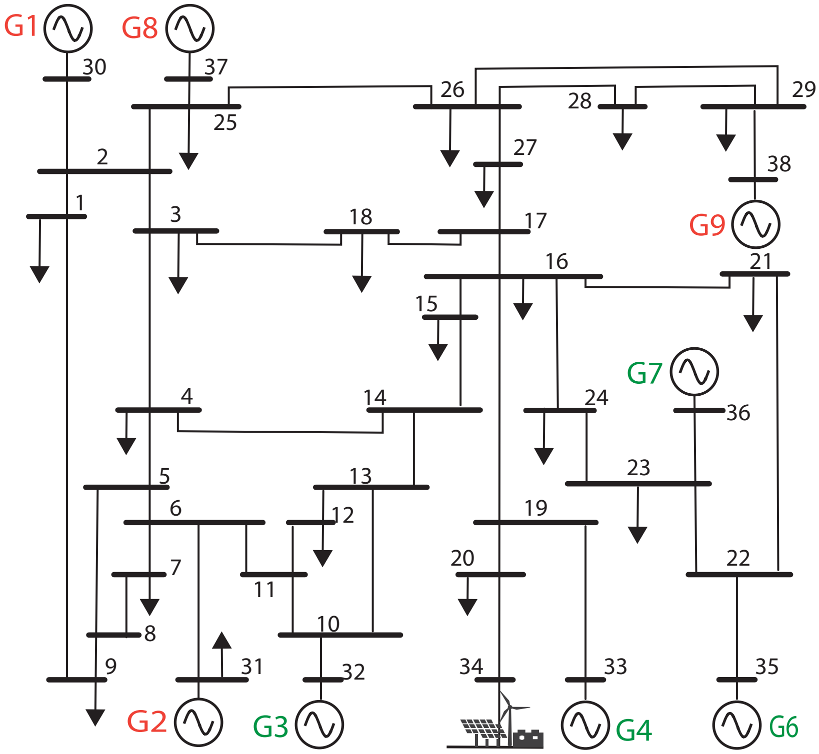

Figure 4.16: New England 39-bus system schematic with the generators divided into two groups: green and red.

the generators can exchange information with each other. Here the IPC performs much like a VSM. This is expected since without communication, the best IPC can do is to utilize its local measurements to take actions.

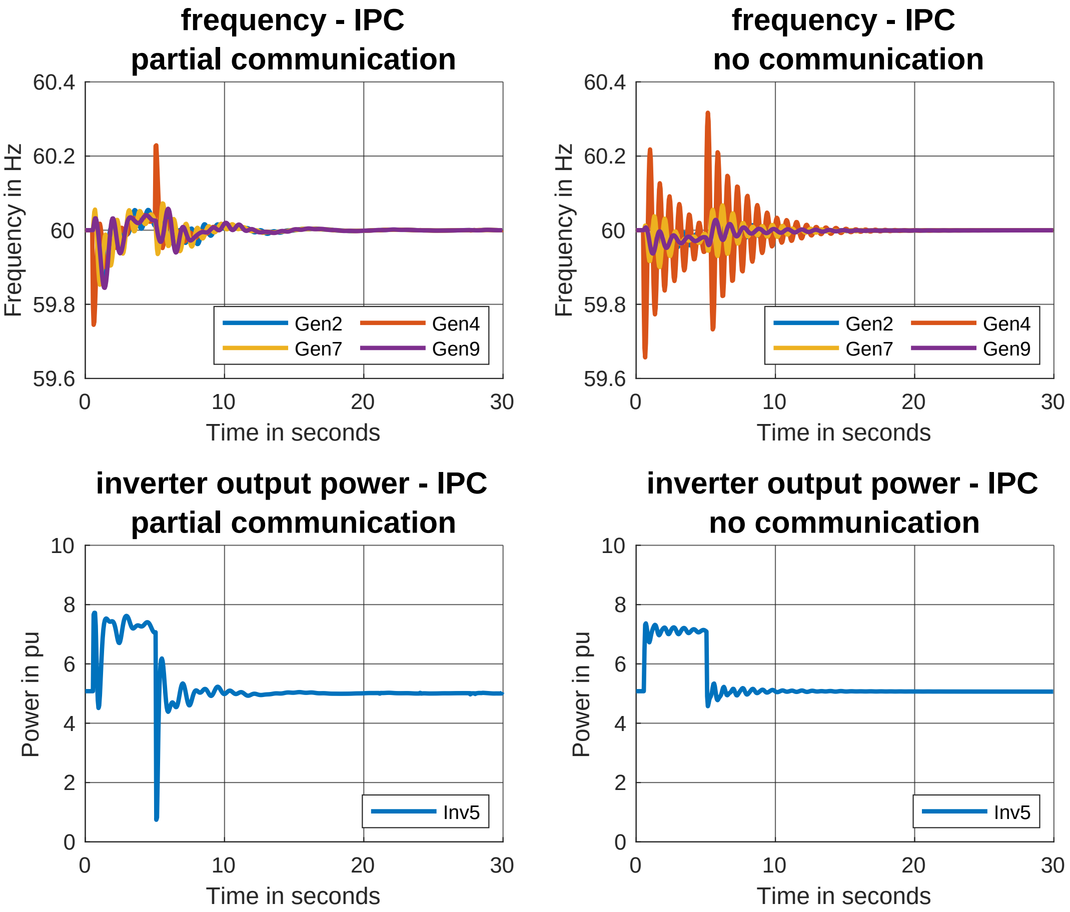

Figure 4.17: Comparison of IPC control actions in a NE39 network under a partial and no-communication scenario. The IPC still outperforms the VSM in its ability to minimize the frequency deviation

4.6 Conclusion

In this chapter, we proposed a novel control strategy called the Inverter Power Control that optimally determines the active power set-point for an inverter-based resource in real-time. Using a model predictive control framework, hard power and energy constraints are considered explicitly in the optimization process. We show via simulation on a test system the superiority of the proposed controller in comparison to the optimally tuned virtual synchronous machine, under both noisy and limited communication settings. Our future work explores enhancing the controller to function in a large network with multiple IBRs, integrating model identification techniques and robustness to communication delays.

Chapter 5

MULTI-INVERTER POWER CONTROL IN LOW-INERTIA POWER SYSTEMS

5.1 Introduction

5.1.1 Motivation

In most parts of the world, the present day electric grid consists of a mix of traditional synchronous generators and inverter-based resources (IBRs) such as solar, wind, and batteries, typically connected via power electronics to the grid. In a bid to render the grid more sustainable coupled with advancements in technology development of energy storage, there is a projected increase in the amount of IBRs that will be integrated to the grid by 2050 [3]. Since these IBRs are power electronic devices and therefore lacking in physical inertia, there will be an accompanying decline in the available rotational inertia system-wide [16,17]. The benefits of having an adequate amount of physical inertia in the network is that it provides the first-stage primary frequency control [15] in the event of a disturbance or power imbalance to the grid by releasing the kinetic energy stored in the rotating mass of the synchronous machine. The lack of physical inertia by the IBRs can be compensated for by their fast actuation, that is, the IBRs capability of injecting active power into the grid by the virtue of the speed of its power electronic circuits. This implies that if the IBRs can be optimally coordinated and controlled, then they have the capability of responding to frequency changes in the grid at a much faster rate than traditional generators with rotating masses.

5.1.2 Literature Review

Varying control strategies that utilizes the IBRs as a means of providing this initial fast frequency response (FFR) has been the subject of a lot of research in recent years e.g., see [17, 24, 25] and the references within), with the most popular being the *Droop Control* and *Virtual Synchronous Machines* (VSMs). In their most basic forms, the frequency (angle) droop control injects/absorbs an amount of active power in proportion to the frequency deviation (relative phase angle) [26–30], while the VSMs act as a second order oscillator to provide inertia and damping to the grid [31–33]. The parameters (droop slope, inertia and damping constants) used in these strategies can be optimized over to satisfy some standard objectives such as magnitude of the frequency deviation, the rate of change of frequency (ROCOF) and the settling time by using a number of techniques [2, 79, 80].

A fundamental drawback of these control strategies is the constraining of IBRs to behave like synchronous machines when responding to a frequency event as this limits the potentials of the fast acting and flexible IBRs [62]. In addition to the drawbacks of these control strategies discussed in chapter 4 and [62], another important drawback is that during transient conditions where there are huge frequency variations across the network with coherent groups of generators swinging against one another, using control strategies that utilize local information can result in the system going unstable [133–135] due to either errors in estimating the true states and in some cases it does not capture the true frequency dynamics of the whole network. Also, in a network with multiple IBR resources which are asynchronous in nature, some form of coordination is required to ensure that the resources do not compete with each other in trying to provide frequency response. While adaptively changing the parameters of the controllers might improve its performance [81–83], it is still computationally difficult to compute these parameters in real-time and also the controller depends on accurately determining the frequency deviation and ROCOF to determine these parameters which local information cannot reliably provide.

In chapter 4 and in our previous work in [62], we proposed a novel control strategy called the Inverter Power Control (IPC) based on model predictive control (MPC) to optimally determine the active power set-point of an IBR that minimizes the frequency deviation and the ROCOF. We assumed the IBRs integrated to the system can be aggregated into a single

IBR which runs the IPC algorithm. In a system with multiple IBRs, centralized system running a modified version of the IPC is needed to coordinate these resources such that there is no competition amongst the IBRs in injecting active power to the grid to the detriment of the frequency response. As the grid evolves, we expect to see more IBRs connected at different points in the grid and the question becomes how to coordinate these resources to jointly provide fast frequency response in the grid.

5.1.3 Contributions

The contributions of this chapter are as follows:

- We extend the mathematical framework of the IPC, including its ability to handle hard constraints, to a multiple IBR system which we call Multi-IPC (MIPC).
- We show that by including a weighted IBR power output to the objective function we are able to coordinate amongst multiple resources to find the optimal active power set-point of the IBRs that minimizes the frequency deviation and ROCOF.
- We further show how the MPC algorithm is amenable to being used in a distributed control structure where each IBR utilizes state information from neighboring generators, that is, a subset of the total number of generators in the network, by leveraging on an observer and the synchronizing properties of the power system network, to estimate the unmeasured states and disturbances.

As in the single IBR control case, this formulation also implicitly minimizes the systems settling time and finds the best IBRs' set-points at each time step that optimizes the objective over that control horizon. We finally show through simulation studies, the efficacy of the MIPC algorithm in coordinating and controlling multiple IBRs scenario in the IEEE 39-bus system and also its performance under a distributed control structure.

The remainder of this paper is organized as follows: Section 5.2 defines the models used in this paper. Section 5.3 presents the design and formulation of the MIPC algorithm. Section

5.4 presents the distributed MIPC control. Section 5.5 shows the performances of MIPC in a centralized and distributed multiple IBR communication scenario. Section 5.6 concludes the paper.

5.2 Modeling

We denote the real line by $\mathbb{R}$, the cardinality of a set $\mathcal{S}$ as $|\mathcal{S}|$, the $n \times n$ identity and zero matrices as $\boldsymbol{I}_n$ and $\mathbf{0}_n$, respectively. Matrices and vectors are denoted by a bold-faced variables.

5.2.1 System Structure

Let the set of generators and IBRs be denote by $\mathcal{G}$ and $\mathcal{I}$, respectively such that the total number of generating sources in the network is $\mathcal{N} := \mathcal{G} \cup \mathcal{I}$. For frequency stability analysis, the dynamics of the network can be reduced to the dynamics of the interconnected synchronous machine by reducing the entire system into an equivalent network via Kron reduction [122]. This eliminates passive and non-dynamic load buses and leaves only buses with at least one generating source connected such that the frequency dynamics is governed by power imbalances in the system.

5.2.2 Synchronous Machines

The rotor dynamics of each synchronous generator in a given power system is governed by the well-known swing equation [123] which in discretized per unit (p.u.) form is:

$$\begin{aligned} \omega_i^{t+1} &= \omega_i^t + \frac{h}{m_i}\left(P_{\mathrm{m},i}^t - P_{\mathrm{e},i}^t - d_i\omega_i^t\right), \\ \delta_i^{t+1} &= \omega_{\mathrm{b}}\left(\delta_i^t + h\,\omega_i^{t+1}\right), \end{aligned} \tag{5.1}$$

$\forall i \in \mathcal{G}$ where h is the step size for the discrete simulation, δ_i (rad) is the rotor angle, $\omega = \bar{\omega}_i - \omega_0$ is the rotor speed deviation, ω_{b} is the base speed of the system, m_i is the inertia constant, d_i is the damping constant, $P_{\mathrm{m},i}$ is the mechanical input power and $P_{\mathrm{e},i}$ is the electric power output of the i^{th} machine.

The electrical output power $P_{\mathrm{e},i}$ is given by the AC power flow equation in terms of the internal emf $|E_i|$ and rotor angle δ_i:

$$P_{\mathrm{e},i}^t = \sum_{i\sim j} |E_i E_j| [g_{ij} \cos(\delta_i^t - \delta_j^t) + b_{ij} \sin(\delta_i^t - \delta_j^t)], \tag{5.2}$$

$\forall i, j \in \mathcal{G}$, where $g_{ij} + jb_{ij}$ is the reduced admittance between nodes i and j. We assume the internal emf are constant because of the actions of the exciter systems.

The nonlinearity of the AC power flow in (5.2) makes it difficult to use (5.1) for control applications, so we utilize the DC power flow [35] such that the bus dynamics become:

$$\begin{aligned} \triangle\omega_i^{t+1} &= \triangle\omega_i^t + \frac{h}{m_i}\left(\triangle P_{\mathrm{m},i}^t - \triangle P_{\mathrm{e},i}^t - d_i \triangle \omega_i^t\right), \\ \triangle\delta_i^{t+1} &= \omega_{\mathrm{b}}\left(\triangle\delta_i^t + h \ \triangle \omega_i^{t+1}\right), \end{aligned} \tag{5.3}$$

where $\triangle P_{\mathrm{e},i}^t = \sum_{i\sim j} b_{ij} \triangle \delta_{ij}^t$ which is the dc power flow between 2 buses.

We model changes to the mechanical input power $\triangle P_{\mathrm{m},i}^t$ by a combination of droop and automatic governor control (AGC) actions [35].

5.2.3 Observer Design

In dynamic system modeling and control, observers can be used to estimate unknown system states and estimate unknown inputs affecting the system dynamics such as disturbances and noise. It can also to used estimate model mismatch which arises as a result of differences between the actual system dynamics and the model of the system used for control purposes [136]. Let the dynamics of the actual power systems governed by (5.1) be represented concisely by:

$$\begin{aligned} \boldsymbol{x}^{t+1} &= \boldsymbol{f}(\boldsymbol{x}^t, \boldsymbol{u}^t, \boldsymbol{d}^t) \\ \boldsymbol{y}^t &= \boldsymbol{g}(\boldsymbol{x}^t, \boldsymbol{u}^t, \boldsymbol{d}^t). \end{aligned} \tag{5.4}$$

A simple discrete observer model design [127] for the system in (5.4) can be written as:

$$\begin{aligned} \hat{\boldsymbol{x}}^{t|t} &= \hat{\boldsymbol{x}}^{t|t-1} + \boldsymbol{K}(\boldsymbol{y}^t - \hat{\boldsymbol{y}}^t) \\ \hat{\boldsymbol{y}}^t &= \boldsymbol{C}\hat{\boldsymbol{x}}^{t|t-1}, \end{aligned} \tag{5.5}$$

where the notation $\hat{\boldsymbol{x}}^{t|\tau}$ means the prediction of $\boldsymbol{x}^t$ made at time τ. Therefore the variables with $\hat{\boldsymbol{x}}^{\boldsymbol{t|t}}$ is the updated observer state prediction based on new measurement $\boldsymbol{y^t}$, $\hat{\boldsymbol{x}}^{\boldsymbol{t|t-1}}$ is the observer state prediction of the current time step using measurements from the previous time step, and $\boldsymbol{K}$ is a gain chosen such that the error between the measured and predicted state $\boldsymbol{y^t} - \hat{\boldsymbol{y}}^t$ is quickly driven to zero. This gain should be chosen carefully as too high of a gain can result in the controller saturating.

5.3 Multi-Inverter Power Control (MIPC)

In this work, we improve on our proposed IBR output power control algorithm in [62] by extending its performance to handle scenarios where there are multiple IBRs in the network. We term this extended controller as multi-inverter power controller (MIPC). This MIPC controller functions by modifying the initial real power set-points of all the IBRs in the network, that is from P_{0_k} to a new set-point P_{ref_k} as shown in Fig. 4.3 based on not only system state and network information, but also on the output power of the participating IBRs.

When dealing with multiple IBRs in the network, the consideration of how the power imbalance response should be shared amongst the IBRs is needed. This power sharing capability amongst the IBRs can be incorporated into the control algorithm as a weighted minimization of the individual IBRs output power, noting that the IBR output power is a function of the system state and the IBR internal angle as will be discussed later. This is somewhat similar in spirit to the droop configuration in synchronous machines where the individual droop settings of the machines determines how much power each machine contributes to the power imbalance in the network. This allows multiple machines work in tandem to share the responsibility of balancing out the power without competing each other [35]. The difference is that while the droop is a linear map between frequency and power output, the assigned weights here is not necessarily linear.

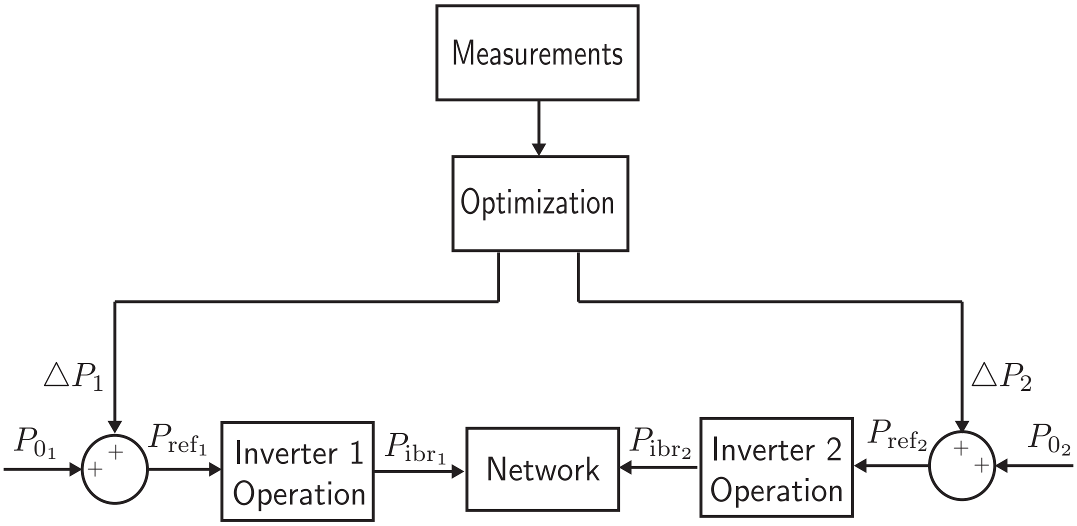

Figure 5.1: Block Diagram showing the operation of the centralized MIPC controller which utilizes state and network information to modify the real power set-point of the IBRs at each timestep

5.3.1 Nonlinear Optimization Problem

Let u_k denote the k^{th} IBR angle (referenced to the slack-bus) and considered as the control variable in the optimization problem. It should be noted that the actual control action of the IBR is not achieved by directly changing the IBRs angle since we do not want to alter the normal operation of the IBR, rather, the optimized u_k which is the IBRs angle is used to find the corresponding active power output of the IBR, which is the actual control action taken.

Let the total power flowing out of the k^{th} IBR be denoted as $P_{\text{ibr},k}$ such that:

$$\begin{aligned} P_{\text{ibr},k} = &\sum_{k\sim i, k\in\mathcal{I}, i\in\mathcal{G}} |E_k E_i|[g_{ki}\cos(u_k-\delta_i)+b_{ki}\sin(u_k-\delta_i)] \\ &+\sum_{k\sim j, j,k\in\mathcal{I}} |E_k E_j|[g_{kj}\cos(u_k-u_j)+b_{kj}\sin(u_k-u_j)], \end{aligned} \tag{5.6}$$

and the total power flowing out of the i^{th} synchronous machine be denoted as $P_{e,i}$ such that:

$$\begin{aligned} P_{\mathrm{e},i} = & \sum_{i\sim j,i,j\in\mathcal{G}} |E_i E_j|[g_{ij}\cos(\delta_i-\delta_j)+b_{ij}\sin(\delta_i-\delta_j)] \\ & + \sum_{i\sim k,i,\in\mathcal{G},k\in\mathcal{I}} |E_i E_k|[g_{ik}\cos(\delta_i-u_k)+b_{ij}\sin(\delta_i-u_k)]. \end{aligned} \tag{5.7}$$

At any timestep, we consider the behavior of the system N steps ahead. The control variables are the IBR angles denoted as $\boldsymbol{u}^0, \boldsymbol{u}^1, \ldots, \boldsymbol{u}^{N-1}$. Once these are set, the rest of the system are governed by their swing equations. As stated earlier, the objective is to minimize a function of the frequency deviation, ROCOF, and the weighted output power of the IBRs. The MIPC problem is then given by:

$$\underset{\{\boldsymbol{u}^0,\boldsymbol{u}^1,\ldots,\boldsymbol{u}^{N-1}\}}{\text{Min.}} \sum_{t=0}^{N-1} \left\{ \|\boldsymbol{\omega}^{t+1}\|_2^2 + \frac{1}{h}\|\boldsymbol{\omega}^{t+1}-\boldsymbol{\omega}^t\|_2^2 + \|\boldsymbol{r}\odot\boldsymbol{P}^t_{\text{ibr}}\|_2^2 \right\} \tag{5.8a}$$

$$\text{s.t. } \omega_i^{t+1} = \omega_i^t + \frac{h}{m_i}\left(P^t_{\mathrm{m},i} - P^t_{\mathrm{e},i} - d_i\omega_i^t - \triangle P_i^t\right), \ \forall i\in\mathcal{G} \tag{5.8b}$$

$$P^t_{e,i} = \text{Equation (5.7)}, \ \forall i\in\mathcal{G} \tag{5.8c}$$

$$P^t_{ibr,k} = \text{Equation (5.6)}, \ \forall k\in\mathcal{I} \tag{5.8d}$$

$$P^t_{\text{ibr,min},k} \le P^t_{\text{ibr},k} \le P^t_{\text{ibr,max},k}, \tag{5.8e}$$

$$\sum_{t=1}^{N} P^t_{\text{ibr,k}} \le E^t_{\text{ibr, tot},k}, \tag{5.8f}$$

where $\boldsymbol{u}^t \in \mathcal{R}^{|\mathcal{I}|}$ is the vector of all IBR angles, $\boldsymbol{\omega}^{t+1} \in \mathcal{R}^{|\mathcal{G}|}$ is a vector of all machine frequency deviations at the next time step, $\boldsymbol{\omega}^{t+1} - \boldsymbol{\omega}^t$ is a vector of all machine ROCOF between the current and next time step, $\boldsymbol{P}^t_{\text{ibr}} \in \mathcal{R}^{|\mathcal{I}|}$ is a vector of all IBR output power and $\boldsymbol{r} \in \mathcal{R}^{|\mathcal{I}|}$ is a vector of 'droop' weights for the IBRs. The evolution of $\boldsymbol{\omega}$ is given in (5.8b) (swing equations) with the added $\triangle P_i$ used to denote disturbances to the network which can be either a loss in generation or load, the power constraints are given in (5.8e) and the energy constraints are in (5.8f). Here we take the frequency deviation and the ROCOF to be equally weighted for simplicity, but their weighting can be adjusted as needed for different practical scenarios. The IBR output power on the other hand is weighted by the IBR droop.

After (5.8) is solved, the control variable $\boldsymbol{u}^0$ is substituted into the IBR output power equation in (5.6) to find the active power set-points of the IBRs. Then the IBRs hold their power at these set-points until the next time the optimization problem is solved. Due to the nonlinearity of the AC power flow equations in (5.6) and (5.7) it is difficult to solve this optimization problem in real-time. Therefore, we use the DC power flow to obtain an approximate problem that is much easier to solve and does not necessarily impact the ability of the MIPC to provide frequency response.

5.3.2 Unconstrained Linearized Problem

To setup the mathematical framework of this problem, we first consider the unconstrained version of (5.8), that is, the MIPC optimization algorithm without the power limit constraint (5.8e) and total energy constraints (5.8f).

State Space Formulation

The main difficulty in solving (5.8) lies in the non-linearity of (5.6) and (5.7). We can use the standard DC power flow model from (5.3) to approximate these equations such that the total output power from the generators can be written as:

$$\begin{aligned}\triangle P_{e,i} &= P_{\mathrm{e},ij} + P_{\mathrm{e},ik}\\ &= \sum_{i\sim j, j\in\mathcal{G}} b_{ij}(\triangle\delta_i - \triangle\delta_j) + \sum_{i\sim j, k\in\mathcal{I}} b_{ik}(\triangle\delta_i - u_k),\\ &= (\sum_{i\sim j} b_{ij} + \sum_{i\sim k,} b_{ik}) \triangle \delta_i + \sum_{i\sim j, j\in\mathcal{G}} -b_{ij} \triangle \delta_j + \sum_{i\sim j, k\in\mathcal{I}} -b_{ik} u_k.\end{aligned} \tag{5.9}$$

which can be written in matrix form as:

$$\triangle \boldsymbol{P_e} = \underbrace{\begin{bmatrix} b_{ii} & -b_{ij} \\ -b_{ji} & b_{jj} \end{bmatrix}}_{\boldsymbol{B}_{\mathrm{GG}}} \begin{bmatrix} \triangle\delta_i \\ \triangle\delta_j \end{bmatrix} + \underbrace{\begin{bmatrix} -b_{ik} \\ -b_{jk} \end{bmatrix}}_{\boldsymbol{B}_{\mathrm{GI}}} u_k, \tag{5.10}$$

where $\boldsymbol{B}_{\text{GG}}$ contains the connection between synchronous generators and $\boldsymbol{B}_{\text{GI}}$ contains the connection between a synchronous generator and IBRs.

Writing the linearized discretized swing equation in (5.3) in state space form and incorporating (5.10) in it results in

$$\underbrace{\begin{bmatrix} \triangle\boldsymbol{\omega}^{t+1} \\ \triangle\boldsymbol{\delta}^{t+1} \end{bmatrix}}_{\boldsymbol{x}^{t+1}} = \underbrace{\begin{bmatrix} -\boldsymbol{M}^{-1}\boldsymbol{D} & -\boldsymbol{M}^{-1}\boldsymbol{B}_{\text{GG}} \\ \boldsymbol{I}_n & \boldsymbol{0}_n \end{bmatrix}}_{\bar{\boldsymbol{A}}} \underbrace{\begin{bmatrix} \triangle\boldsymbol{\omega}^{t} \\ \triangle\boldsymbol{\delta}^{t} \end{bmatrix}}_{\boldsymbol{x}^{t}} + \underbrace{\begin{bmatrix} -\boldsymbol{M}^{-1}\boldsymbol{B}_{\text{GI}} \\ \boldsymbol{0}_n \end{bmatrix}}_{\bar{\boldsymbol{B}}_{\boldsymbol{u}}} \boldsymbol{u}^t + \underbrace{\begin{bmatrix} -\boldsymbol{M}^{-1} \\ \boldsymbol{0}_n \end{bmatrix}}_{\bar{\boldsymbol{B}}_{\boldsymbol{d}}} \underbrace{\triangle\boldsymbol{P}^t}_{\boldsymbol{d}^t} \tag{5.11}$$

where $\triangle\boldsymbol{\delta} \in \mathbb{R}^n$ is the rotor angles deviation, $\triangle\boldsymbol{\omega} \in \mathbb{R}^n$ is the rotor speed deviation, $\boldsymbol{M} = diag(m_1, \ldots, m_n) \in \mathbb{R}^{n\times n}$, $\boldsymbol{D} = diag(d_1, \ldots, d_n) \in \mathbb{R}^{n\times n} \in \mathbb{R}^n$, $\triangle\boldsymbol{P} \in \mathbb{R}^n$ is vector of all power deviations which comes from the disturbances and noises in the system, denoted by $\boldsymbol{d}^t$.

Assuming full observability of states, the output equation can be written as:

$$\boldsymbol{y}^t = \underbrace{\begin{bmatrix} \boldsymbol{I}_n & \boldsymbol{0}_n \end{bmatrix}}_{\bar{\boldsymbol{C}}} \underbrace{\begin{bmatrix} \triangle\boldsymbol{\omega}^{t} \\ \triangle\boldsymbol{\delta}^{t} \end{bmatrix}}_{\boldsymbol{x}^{t}}. \tag{5.12}$$

Let $n = |\mathcal{G}|$, $m = 2 \times n$, $p = |\mathcal{I}|$ and $n_d = |\boldsymbol{d}|$ such that $|\bar{\boldsymbol{A}}| = m \times m$, $|\bar{\boldsymbol{B}}_{\boldsymbol{u}}| = m \times p$, $|\bar{\boldsymbol{B}}_{\boldsymbol{d}}| = m \times n_d$, and $|\bar{\boldsymbol{C}}| = m \times m$.

State and Disturbance Estimation

In the event of a disturbance to the network, such as a loss of generating capacity or load, the IPC does not know the location and magnitude of this disturbance. Furthermore, due to the use of the linearized state space model in (5.11) there will be a difference between predicted and measured output as a result of the model mismatch. All these can lead to an incorrect estimation of the system states at each time step and an offset in the eventual steady state value of the system states.

To estimate the state and disturbance with model mismatch and other forms of disturbance, we first redefine $\boldsymbol{d}^t$ and $\bar{\boldsymbol{B}}_d$ in (5.11) as a vector of all possible disturbances and some weighting matrix respectively. We then integrate the IPC state space model in (5.11) with an input/output constant disturbance model [127] to obtain:

$$\begin{aligned} \boldsymbol{x}^{t+1} &= \bar{\boldsymbol{A}}\boldsymbol{x}^t + \bar{\boldsymbol{B}}_u\boldsymbol{u}^t + \bar{\boldsymbol{B}}_d\boldsymbol{d}^t \\ \boldsymbol{d}^{t+1} &= \boldsymbol{d}^t \\ \boldsymbol{y}^t &= \bar{\boldsymbol{C}}\boldsymbol{x}^t + \boldsymbol{C}_d\boldsymbol{d}^t, \end{aligned} \tag{5.13}$$

where the disturbance $\boldsymbol{d}$ is modeled as a constant disturbance for the control period such that it follows an integral dynamics. Equation (5.13) can then be written in an augmented state space form as:

$$\begin{aligned} \underbrace{\begin{bmatrix} \boldsymbol{x}^{t+1} \\ \boldsymbol{d}^{t+1} \end{bmatrix}}_{\boldsymbol{z}^{t+1}} &= \underbrace{\begin{bmatrix} \bar{\boldsymbol{A}} & \bar{\boldsymbol{B}}_d \\ \boldsymbol{0}_n & \boldsymbol{I}_n \end{bmatrix}}_{\boldsymbol{A}} \underbrace{\begin{bmatrix} \boldsymbol{x}^{t} \\ \boldsymbol{d}^{t} \end{bmatrix}}_{\boldsymbol{z}^{t}} + \underbrace{\begin{bmatrix} \bar{\boldsymbol{B}}_u \\ \boldsymbol{0} \end{bmatrix}}_{\boldsymbol{B}} \boldsymbol{u}^t \\ \boldsymbol{y}^t &= \underbrace{\begin{bmatrix} \bar{\boldsymbol{C}} & \bar{\boldsymbol{C}}_d \end{bmatrix}}_{\boldsymbol{C}} \underbrace{\begin{bmatrix} \boldsymbol{x}^{t} \\ \boldsymbol{d}^{t} \end{bmatrix}}_{\boldsymbol{z}^{t}}. \end{aligned} \tag{5.14}$$

The predicted augmented state and disturbance can then be estimated using the linear observer model in (5.5) as:

$$\hat{\boldsymbol{z}}^{t|t} = \hat{\boldsymbol{z}}^{t|t-1} + \underbrace{\begin{bmatrix} \boldsymbol{K}_x \\ \boldsymbol{K}_d \end{bmatrix}}_{\boldsymbol{K}} \left(\boldsymbol{y}^t - \boldsymbol{C}\hat{\boldsymbol{z}}^{t|t-1}\right) \tag{5.15}$$

where $\boldsymbol{K}$ is the gain matrix for the augmented state and disturbance variable. For simplicity, we adopt a fixed gain structure for the gain matrix $\boldsymbol{K}$ with $\boldsymbol{K_x} \in \mathcal{R}^{m\times m}$ and $\boldsymbol{K_d} \in \mathcal{R}^{m\times m}$ chosen such that the estimator is stable.

Remark 1 *The augmented system in (5.14) is observable if and only if $(\bar{C}, \bar{A})$ is observable and*

$$\begin{bmatrix} \bar{\boldsymbol{A}} - \boldsymbol{I_n} & \bar{\boldsymbol{B}}_{\boldsymbol{d}} \\ \bar{\boldsymbol{C}} & \bar{\boldsymbol{C}}_{\boldsymbol{d}} \end{bmatrix} \tag{5.16}$$

has full column rank (see [127] for proof).

Remark 2 *For condition in (5.16) to be satisfied, the number of disturbances in $\boldsymbol{d}$ has to be smaller or equal to the number of available measurements, that is, if $\boldsymbol{y}^t \in \mathcal{R}^m$ and $\boldsymbol{d}^t \in \mathcal{R}^{n_d}$, then $n_d \leq m$ (see [137, 138] for proof)*

In this work, we choose $n_d = m$, such that $\bar{\boldsymbol{B}}_{\boldsymbol{d}} \in \mathcal{R}^{m \times m}$ and $\bar{\boldsymbol{C}}_{\boldsymbol{d}} \in \mathcal{R}^{m \times m}$ can be chosen to satisfy the observability condition in (5.16).

Model Predictive Control (MPC)

With the model of the system defined and the ability to predict future evolutions guaranteed, we reformulate the L2-norm objective function in (5.8a) in terms of the network model in (5.14) as follows:

a) Frequency deviation:

$$\triangle \boldsymbol{\omega}^{\boldsymbol{t}} = \underbrace{\begin{bmatrix} \boldsymbol{I_n} & \boldsymbol{0_n} & \boldsymbol{0_n} \end{bmatrix}}_{\boldsymbol{C_p}} \hat{\boldsymbol{z}}^{\boldsymbol{t}}, \tag{5.17}$$

such that

$$\|\boldsymbol{\omega}^t\|_2^2 = (\boldsymbol{C_p} \hat{\boldsymbol{z}}^{\boldsymbol{t}})^{\boldsymbol{T}} \bar{\boldsymbol{Q}}_{\boldsymbol{1}} (\boldsymbol{C_p} \hat{\boldsymbol{z}}^{\boldsymbol{t}}) = \hat{\boldsymbol{z}}^{\boldsymbol{t}\boldsymbol{T}} \underbrace{\boldsymbol{C}_{\boldsymbol{p}}^{\boldsymbol{T}} \bar{\boldsymbol{Q}}_{\boldsymbol{1}} \boldsymbol{C_p}}_{\hat{\boldsymbol{Q}}_{\boldsymbol{1}}} \hat{\boldsymbol{z}}^{\boldsymbol{t}}. \tag{5.18}$$

b) ROCOF:

$$\frac{1}{h} \left[\triangle \boldsymbol{\omega}^{\boldsymbol{t}} - \triangle \boldsymbol{\omega}^{\boldsymbol{t-1}} \right] = \frac{1}{h} \boldsymbol{C_p} \left[\hat{\boldsymbol{z}}^{\boldsymbol{t}} - \hat{\boldsymbol{z}}^{\boldsymbol{t-1}} \right] = \hat{\boldsymbol{C}}_{\boldsymbol{p}} \triangle \hat{\boldsymbol{z}}^{\boldsymbol{t}} \tag{5.19}$$

such that

$$\frac{1}{h}\| \triangle\boldsymbol{\omega}^{t} - \triangle\boldsymbol{\omega}^{t-1} \|_2^2 = (\hat{\boldsymbol{C}}_{\boldsymbol{p}} \triangle \hat{\boldsymbol{z}}^{t})^{\boldsymbol{T}}\bar{\boldsymbol{Q}}_{\boldsymbol{2}}(\hat{\boldsymbol{C}}_{\boldsymbol{p}} \triangle \hat{\boldsymbol{z}}^{t}) = \triangle\hat{\boldsymbol{z}}^{t^{\boldsymbol{T}}} \underbrace{\hat{\boldsymbol{C}}_{\boldsymbol{p}}^{\boldsymbol{T}}\bar{\boldsymbol{Q}}_{\boldsymbol{2}}\hat{\boldsymbol{C}}_{\boldsymbol{p}}}_{\hat{\boldsymbol{Q}}_{\boldsymbol{2}}} \triangle\hat{\boldsymbol{z}}^{t}. \tag{5.20}$$

c) Output IBR Power: To compute the weighted IBR out power in terms of the network model, we utilize the DC power flow model in (5.3) such that

$$\begin{aligned} P_{\mathrm{ibr},k}^{t} &= \sum_{k\sim i, i\in\mathcal{G}} b_{ki}(u_k^t - \triangle\delta_i^t) + \sum_{k\sim j, j\in\mathcal{I}} b_{kj}(u_k^t - u_j^t) \\ &= \sum_i b_{ki}u_k^t - \sum_i b_{ki} \triangle \delta_i^t + \sum_j b_{kj}u_k^t - \sum_j b_{kj}u_j^t \\ &= -\sum_i b_{ki} \triangle \delta_i^t + \underbrace{\sum_i b_{ki}u_k^t + \sum_j b_{kj}u_k^t}_{\sum(b_{ki}+b_{kj})=\sum b_{kk}} + \sum_j b_{kj}u_j^t \\ &= -\sum_{k\sim i, i\in\mathcal{G}} b_{ki} \triangle \delta_i^t + \sum b_{kk}u_k^t - \sum_{k\sim j, j\in\mathcal{I}} b_{kj}u_j^t, \end{aligned} \tag{5.21}$$

which can be written in matrix form as:

$$P_{\mathrm{ibr},k}^{t} = \underbrace{\begin{bmatrix} \boldsymbol{0_n} & -[\boldsymbol{B}]_{\boldsymbol{ki}} & \boldsymbol{0_n} \end{bmatrix}}_{\boldsymbol{B_{p1}}} \hat{\boldsymbol{z}}^{t} + \underbrace{\begin{bmatrix} [\boldsymbol{B}]_{\boldsymbol{kk}} & -[\boldsymbol{B}]_{\boldsymbol{kj}} \end{bmatrix}}_{\boldsymbol{B_{p2}}} \underbrace{\begin{bmatrix} \boldsymbol{u_k^t} \\ \boldsymbol{u_j^t} \end{bmatrix}}_{\boldsymbol{u^t}} \tag{5.22}$$

such that

$$\begin{aligned} \|\boldsymbol{r} \odot \boldsymbol{P}_{\mathrm{ibr}}^{t}\|_2^2 &= (\boldsymbol{r} \odot \boldsymbol{P}_{\mathrm{ibr}}^{t})^{\boldsymbol{T}}\bar{\boldsymbol{R}}(\boldsymbol{r} \odot \boldsymbol{P}_{\mathrm{ibr}}^{t}) = \boldsymbol{P}_{\mathrm{ibr}}^{t^{\boldsymbol{T}}} \underbrace{\boldsymbol{r}^{\boldsymbol{T}}\bar{\boldsymbol{R}}\boldsymbol{r}}_{\hat{\boldsymbol{R}}} \boldsymbol{P}_{\mathrm{ibr}}^{t}, \\ &= (\boldsymbol{B_{p1}}\hat{\boldsymbol{z}}^{t} + \boldsymbol{B_{p2}}\boldsymbol{u}^{t})^{\boldsymbol{T}}\hat{\boldsymbol{R}}(\boldsymbol{B_{p1}}\hat{\boldsymbol{z}}^{t} + \boldsymbol{B_{p2}}\boldsymbol{u}^{t}), \\ &= (\boldsymbol{B_{p1}}\hat{\boldsymbol{z}}^{t})^{\boldsymbol{T}}\hat{\boldsymbol{R}}(\boldsymbol{B_{p1}}\hat{\boldsymbol{z}}^{t}) + (\boldsymbol{B_{p1}}\hat{\boldsymbol{z}}^{t})^{\boldsymbol{T}}\hat{\boldsymbol{R}}(\boldsymbol{B_{p2}}\boldsymbol{u}^{t}) \\ &\quad +(\boldsymbol{B_{p2}}\boldsymbol{u}^{t})^{\boldsymbol{T}}\hat{\boldsymbol{R}}(\boldsymbol{B_{p1}}\hat{\boldsymbol{z}}^{t}) + (\boldsymbol{B_{p2}}\boldsymbol{u}^{t})^{\boldsymbol{T}}\hat{\boldsymbol{R}}(\boldsymbol{B_{p2}}\boldsymbol{u}^{t}) \\ &= \hat{\boldsymbol{z}}^{t^{\boldsymbol{T}}}\hat{\boldsymbol{R}}_{\boldsymbol{zz}}\hat{\boldsymbol{z}}^{t} + \hat{\boldsymbol{z}}^{t^{\boldsymbol{T}}}\hat{\boldsymbol{R}}_{\boldsymbol{zu}}\boldsymbol{u}^{t} + \boldsymbol{u}^{t^{\boldsymbol{T}}}\hat{\boldsymbol{R}}_{\boldsymbol{uz}}\hat{\boldsymbol{z}}^{t} + \boldsymbol{u}^{t^{\boldsymbol{T}}}\hat{\boldsymbol{R}}_{\boldsymbol{uu}}\boldsymbol{u}^{t}. \end{aligned} \tag{5.23}$$

In combination, the total objective function

$$\begin{aligned}
J &= \|\boldsymbol{\omega}^{t+1}\|_2^2 + \frac{1}{h}\|\boldsymbol{\omega}^{t+1} - \boldsymbol{\omega}^t\|_2^2 + \|\boldsymbol{r} \odot \boldsymbol{P}^t_{\text{ibr}}\|_2^2 \\
&= \boldsymbol{\hat{z}^{t^T}} \boldsymbol{\hat{Q}_1} \boldsymbol{\hat{z}^t} + \triangle \boldsymbol{\hat{z}^{t^T}} \boldsymbol{\hat{Q}_2} \triangle \boldsymbol{\hat{z}^t} + \boldsymbol{\hat{z}^{t^T}} \boldsymbol{\hat{R}_{zz}} \boldsymbol{\hat{z}^t} + \boldsymbol{\hat{z}^{t^T}} \boldsymbol{\hat{R}_{zu}} \boldsymbol{u^t} + \boldsymbol{u^{t^T}} \boldsymbol{\hat{R}_{uz}} \boldsymbol{\hat{z}^t} + \boldsymbol{u^{t^T}} \boldsymbol{\hat{R}_{uu}} \boldsymbol{u^t} \\
&= \boldsymbol{\hat{z}^{t^T}} \underbrace{(\boldsymbol{\hat{Q}_1} + \boldsymbol{\hat{R}_{zz}})}_{\boldsymbol{\hat{Q}_R}} \boldsymbol{\hat{z}^t} + \triangle \boldsymbol{\hat{z}^{t^T}} \boldsymbol{\hat{Q}_2} \triangle \boldsymbol{\hat{z}^t} + \boldsymbol{\hat{z}^{t^T}} \boldsymbol{\hat{R}_{zu}} \boldsymbol{u^t} + \boldsymbol{u^{t^T}} \boldsymbol{\hat{R}_{uz}} \boldsymbol{\hat{z}^t} + \boldsymbol{u^{t^T}} \boldsymbol{\hat{R}_{uu}} \boldsymbol{u^t}
\end{aligned} \tag{5.24}$$

For an unconstrained case, that is, the IPC optimization algorithm in (5.8) without the power limit constraint (5.8e) and total energy constraints (5.8f), the MPC is reduced to a linear quadratic programming (LQR) problem which can then be written as:

$$\begin{aligned}
&\underset{\boldsymbol{u^t}}{\text{Min.}}\ J = \frac{1}{2}\sum_{t=1}^{N-1}\left[\boldsymbol{\hat{z}^{t^T}} \boldsymbol{\hat{Q}_R} \boldsymbol{\hat{z}^t} + \triangle \boldsymbol{\hat{z}^{t^T}} \boldsymbol{\hat{Q}_2} \triangle \boldsymbol{\hat{z}^t} + \boldsymbol{\hat{z}^{t^T}} \boldsymbol{\hat{R}_{zu}} \boldsymbol{u^t} + \boldsymbol{u^{t^T}} \boldsymbol{\hat{R}_{uz}} \boldsymbol{\hat{z}^t} + \boldsymbol{u^{t^T}} \boldsymbol{\hat{R}_{uu}} \boldsymbol{u^t}\right] \\
&\text{s.t.}\quad \boldsymbol{\hat{z}^{t+1} = A\hat{z}^t + Bu^t.}
\end{aligned} \tag{5.25}$$

For a N control horizon duration, (5.25) can be re-written as:

$$J = \frac{1}{2}\boldsymbol{\hat{z}^{0^T}} \boldsymbol{G}_{\text{mod}} \boldsymbol{\hat{z}^0} + \frac{1}{2}\boldsymbol{u^T} \boldsymbol{H}_{\text{mod}} \boldsymbol{u} + \boldsymbol{\hat{z}^{0^T}} \boldsymbol{F}_{\text{mod}} \boldsymbol{u,} \tag{5.26}$$

where $\boldsymbol{H}_{\text{mod}}$ and $\boldsymbol{F}_{\text{mod}}$ are constant matrices depending on $\boldsymbol{A}$ and $\boldsymbol{B}$.

For an infinite-horizon LQR problem, the optimal solution is linear in the starting point $\boldsymbol{\hat{z}}^0$ such that:

$$\boldsymbol{u}^* = -\boldsymbol{H}_{\text{mod}}^{\boldsymbol{-1}} \boldsymbol{F}_{\text{mod}}^{\boldsymbol{T}} \boldsymbol{\hat{z}^0}. \tag{5.27}$$

This solution can be interpreted as a linear policy, where the optimal action is determined as a linear function of the current state information. (see appendix A.2 for derivation of $\boldsymbol{A}$, $\boldsymbol{B}$ and $\boldsymbol{u}^*$).

5.3.3 Constrained Linearized Problem

We now consider the constraints on the power output at each time step (5.8e) and constraints on the total energy available to provide frequency control (5.8f) in (5.8). This is for the most part similar to the constraint considered in chapter 4 but extended to a multi-IBR case and repeated in this chapter for completeness.

In the presence of constraints, (5.26) becomes of the form.

$$\begin{aligned} &\underset{\boldsymbol{u}}{\text{Min.}}\ J = \frac{1}{2}\hat{\boldsymbol{z}}^{\boldsymbol{0}^{\boldsymbol{T}}}\boldsymbol{G}_{\text{mod}}\hat{\boldsymbol{z}}^{\boldsymbol{0}} + \frac{1}{2}\boldsymbol{u}^{\boldsymbol{T}}\boldsymbol{H}_{\text{mod}}\boldsymbol{u} + \hat{\boldsymbol{z}}^{\boldsymbol{0}^{\boldsymbol{T}}}\boldsymbol{F}_{\text{mod}}\boldsymbol{u} \\ &\text{s.t.}\quad \boldsymbol{L}\boldsymbol{u} \leq \boldsymbol{W} + \boldsymbol{V}\hat{\boldsymbol{z}}^{\boldsymbol{0}}, \end{aligned} \tag{5.28}$$

where $\mathbf{L}, \boldsymbol{W}$ and $\boldsymbol{V}$ depends on the constraint being considered. Equation (5.28) can no longer be solved as a linear programming problem but as a quadratic programming optimization problem with linear constraints which can be solved extremely efficiently for systems with thousands of variables and constraints [126].

Power Output Constraint

In practical considerations, there can be a limit on the amount of instantaneous power that can be drawn from the IBR due to factors such as the distance to the maximum power tracking operating point, the current ratings and switching speed of some power electronics components, and also power capability or C-rate of a battery.

The linearized instantaneous output power $P^t_{\text{ibr},k}$ derived in (5.22) with the minimum and maximum power limit of $P^t_{\text{ibr,min},k} \leq P^t_{\text{ibr},k} \leq P^t_{\text{ibr,max},k}$ for a N time horizon can be written in the linear constraint form of (5.28) (see appendix A.3) as

$$\underbrace{\begin{bmatrix} -\tilde{\boldsymbol{B}}_{\text{p2}} \\ \tilde{\boldsymbol{B}}_{\text{p2}} \end{bmatrix}}_{\boldsymbol{L}} \boldsymbol{u} \leq \underbrace{\begin{bmatrix} -\tilde{\boldsymbol{P}}_{\text{ibr, min}} \\ \tilde{\boldsymbol{P}}_{\text{ibr, max}} \end{bmatrix}}_{\boldsymbol{W}} + \underbrace{\begin{bmatrix} \tilde{\boldsymbol{B}}_{\text{p1}} \\ -\tilde{\boldsymbol{B}}_{\text{p1}} \end{bmatrix}}_{\boldsymbol{V}} \hat{\boldsymbol{z}}^{\boldsymbol{0}}. \tag{5.29}$$

Total Energy Constraint

This constraint occurs when there is a limit on the energy capacity of the IBR as in the case of a battery. For this constraint to be fully satisfied, the total energy not only at the end of the control horizon but also at each rolling sum of the consecutive time step should be less than the maximum energy capacity.

As with the power output constraint, the total energy constraint $\sum_{t=1}^{N} P^t_{\text{ibr,k}} \leq E^t_{\text{ibr, tot},k}$ can be obtained by taking the rolling sum over the linearized instantaneous output power $P^t_{\text{ibr},k}$ derived in (5.22). To avoid a sudden decline in the power output when the maximum available energy limit is reached, a rate constraint can also be added to the power output decline between a specified consecutive time step. This can be obtained by by taking a one time step difference of the power output matrix in (5.22), that is, a difference between the next time step and current time step power output. For a N time horizon, these two constraint can be written in the linear constraint form of (5.28) (see appendix A.4) as

$$\underbrace{\begin{bmatrix} \tilde{\boldsymbol{B}}_{\text{e2}} \\ \tilde{\boldsymbol{B}}_{\text{r2}} \end{bmatrix}}_{\boldsymbol{L}} \boldsymbol{u} \leq \underbrace{\begin{bmatrix} \tilde{\boldsymbol{E}}_{\text{ibr, tot}} \\ \boldsymbol{\epsilon} \end{bmatrix}}_{\boldsymbol{W}} + \underbrace{\begin{bmatrix} -\tilde{\boldsymbol{B}}_{\text{e1}} \\ -\tilde{\boldsymbol{B}}_{\text{r1}} \end{bmatrix}}_{\boldsymbol{V}} \hat{\boldsymbol{z}}^{\boldsymbol{0}}. \tag{5.30}$$

where $\boldsymbol{\epsilon}$ is a vector of IBR power output rate limit for each one time step difference. See chapter appendix (A.4) for derivation.

5.4 *Distributed Control*

In section 5.3, we assumed that a centralized control center exists that receives state information, computes the MIPC algorithm and sends the active power set-points to the IBRs across the network. In a more realistic setting, especially in a large network where IBRs are interspersed, it might be difficult to get all state information to a central server and afterwards disperse to all IBRs. Under this setting, a form of distributed control strategy [139, 140] can be adopted where each IBR evaluates the same global objective function in the MIPC algorithm using the the network wide model and state information available to them, usually from a subset of the generators.

To achieve this, we assume at $t = 0$, the full state information is available to all IBRs after which we assume no further communication but instead rely on the synchronizing properties of the power systems [141]. It is well known that the frequencies of the synchronous machines are tightly coupled such that a disturbance to one generator is reflected across the network in the frequencies of the other generators [15]. At the next timestep, the IBR receives state information from a subset of generators as seen in Fig.5.2 and carries out an individual state and disturbance estimation using a reduced-order form of the augmented observer model in (5.16). That is, each IBR first estimates the missing states and then compensates for a possible mismatch by estimating the disturbance.

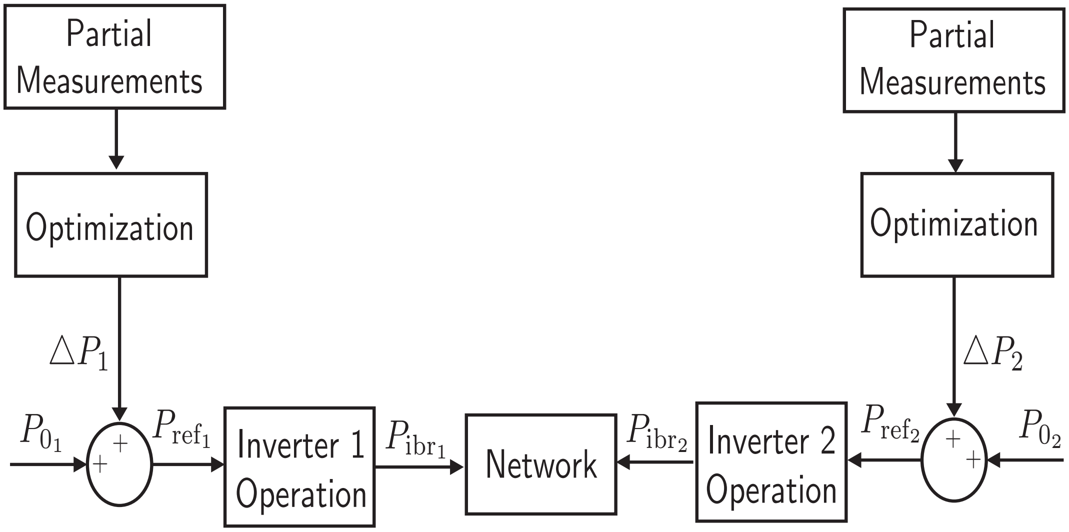

Figure 5.2: Block Diagram showing the operation of the distributed MIPC controller running on each IBR which utilizes partial state and network information to modify the real power set-point of the IBRs at each timestep

Consider the operation of one of the IBRs $\mathcal{I}_k \in \mathcal{I}$ that receives state variable information from a subset of generators $\mathcal{G}_k \in \mathcal{G}$, where $|\mathcal{G}_k| = w$, such that (5.16) becomes:

$$\underbrace{\begin{bmatrix} \hat{\boldsymbol{x}}_{\boldsymbol{k}}^{\boldsymbol{t|t}} \\ \hat{\boldsymbol{d}}_{\boldsymbol{k}}^{\boldsymbol{t|t}} \end{bmatrix}}_{\hat{\boldsymbol{z}}_{\boldsymbol{k}}^{\boldsymbol{t|t}}} = \underbrace{\begin{bmatrix} \hat{\boldsymbol{x}}_{\boldsymbol{k}}^{\boldsymbol{t|t-1}} \\ \hat{\boldsymbol{d}}_{\boldsymbol{k}}^{\boldsymbol{t|t-1}} \end{bmatrix}}_{\hat{\boldsymbol{z}}_{\boldsymbol{k}}^{\boldsymbol{t|t-1}}} + \underbrace{\begin{bmatrix} \boldsymbol{L}_{\boldsymbol{k_x}} \\ \boldsymbol{L}_{\boldsymbol{k_d}} \end{bmatrix}}_{\bar{\boldsymbol{L}}_{\boldsymbol{k}}} \left(\boldsymbol{y}_{\boldsymbol{k}}^{\boldsymbol{t}} - \begin{bmatrix} \boldsymbol{C} & \boldsymbol{C_d} \end{bmatrix} \begin{bmatrix} \hat{\boldsymbol{x}}_{\boldsymbol{k}}^{\boldsymbol{t|t-1}} \\ \hat{\boldsymbol{d}}_{\boldsymbol{k}}^{\boldsymbol{t|t-1}} \end{bmatrix} \right) \tag{5.31}$$

where $y_k^t \in \mathcal{R}^{2w}$ is the state information received from $\mathcal{G}_k$, and L_k is the augmented gain matrix for the k^{th} IBR such that $L_{k_x}, L_{k_d} \in \mathcal{R}^{m\times 2w}$. In this form, each IBR can then compute the MIPC algorithm in (5.25) such that:

$$\begin{aligned} &\underset{\boldsymbol{u}_{\boldsymbol{k}}^{\boldsymbol{t}}}{\text{Min.}}\ J_k = \frac{1}{2}\hat{\boldsymbol{z}}_{\boldsymbol{k}}^{\boldsymbol{0^T}}\boldsymbol{G}_{\text{mod}}\hat{\boldsymbol{z}}_{\boldsymbol{k}}^{\boldsymbol{0}} + \frac{1}{2}\boldsymbol{u}_{\boldsymbol{k}}^{\boldsymbol{T}}\boldsymbol{H}_{\text{mod}}\boldsymbol{u}_{\boldsymbol{k}} + \hat{\boldsymbol{z}}_{\boldsymbol{k}}^{\boldsymbol{0^T}}\boldsymbol{F}_{\text{mod}}\boldsymbol{u}_{\boldsymbol{k}}, \\ &\text{s.t.}\quad \hat{\boldsymbol{z}}_{\boldsymbol{k}}^{\boldsymbol{t+1}} = \boldsymbol{A}\hat{\boldsymbol{z}}_{\boldsymbol{k}}^{\boldsymbol{t}} + \boldsymbol{B}\boldsymbol{u}_{\boldsymbol{k}}^{\boldsymbol{t}}. \end{aligned} \tag{5.32}$$

Under this algorithm, each IBR can predict the possible output of other IBRs and adjust its output accordingly. This means that after (5.32) is solved, each IBR substitutes the control variable $\boldsymbol{u}_{\boldsymbol{k}}{}^0(t)$ into (5.6) to determine its active power set-point. We show via simulation in the result section that the IBRs under this setup are able to stabilize the system.

5.5 Results

In this section, we validate the performance of the MIPC controller by testing it on the IEEE New England 10-machine 39-bus (NE39) system used for power systems dynamics stability studies [129]. We study scenarios of up to four IBR integration into the network and of constraints on the power and energy output of the IBRs. We also study the performance of the MIPC controller in a limited communication centralized and distributed control framework. Under each scenario, a large disturbance in form a partial generating capacity loss is applied to a generator in the network to initiate an event that can lead to a marked frequency decline.

The performance metrics for the MIPC controller is its ability to maintain the the frequency deviation within a small range, limiting the ROCOF, and quickly recovering to the nominal frequency value.

The NE39 network is transformed into a low-inertia network by removing the interconnection to the rest of the US network and replacing the generator at certain buses with IBRs (either solar or wind but coupled with energy storage) of aggregated capacity equalling that of the replaced generator, and reduced to an equivalent network using Kron reduction. For the one IBR case, gen 5 at bus 34; for the two IBRs case as shown in Fig. 5.3, gen 3 and 5 at buses 32 and 34 respectively; for the three IBRs case, gen 3, 5 and 7 at buses 32, 34 and 36 respectively; and for the four IBRs case, gen 1, 3, 5 and 7 at buses 30, 32, 34 and 36 respectively, are replaced with IBRs. The disturbance is applied to the fourth generator ($G4$) located at bus 33. Its power output starts of at 6.32pu, then decreases to 3.16pu at 0.5 seconds and later increases to 4.42pu at 2 seconds. We utilize this disturbance structure to ensure that the dynamics of the systems are well-excited.

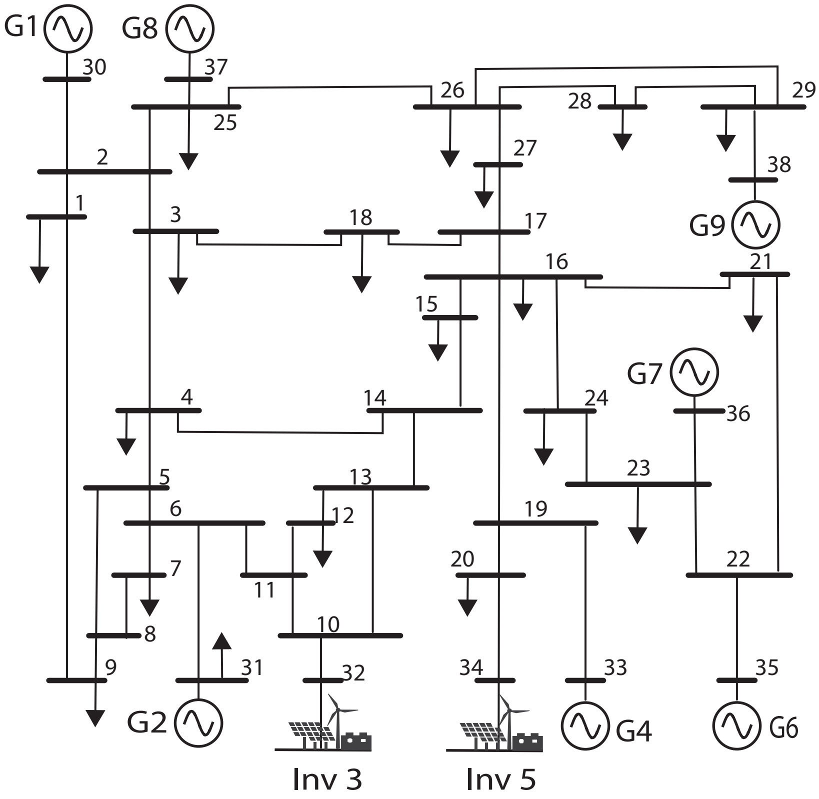

Figure 5.3: New England 39-bus system schematic with the generators 3 and 5 at bus 32 and 34 respectively, replaced with an IBRs of equal aggregated capacity.

5.5.1 Centralized Control

Under an unconstrained scenario, that is, under the conditions of unlimited IBR power and energy capacities, Fig. 5.4 shows the frequency response of select generators and inverter output power of the IBRs. For a clearer viewing, only the frequency response of the second (slack), fourth (disturbed), sixth and ninth generator are shown. When more than one IBR is integrated into the network, the MIPC is able to efficiently determine the optimal active power output of the individual IBR to ensure a suitable frequency response. The MIPC is able to share the total power response amongst the IBRs by weighting the output power of the IBRs similar to the way power output response is shared in a synchronous machine network. Furthermore, Fig. 5.4 shows that a better frequency response performance is obtained when using multiple IBRs as the frequency is able to return to its nominal value more quickly, with reduced oscillations as the number of IBRs increase, and the positive frequency deviation is reduced. In general, the MIPC controller is able to keep the frequency deviation within a 0.2Hz margin. The higher the number of IBRs the lower the amount of active power each IBR has to contribute.

As discussed in 5.3.3, one of the advantages of the MIPC control strategy is the ability to incorporate hard constraints into its optimization problem and constraints such as power and energy limit on IBRs are quite popular. Fig. 5.5 shows the frequency response of select generators and the inverter power outputs when two IBRs are integrated to the network, with a power limit of 7 pu and energy limit of 70 pu placed on the IBR (*inv 3*) connected at bus 32 in Fig. 5.3. Again for clearer viewing, only the frequency response of the second (slack), fourth (disturbed), sixth and ninth generator are shown.

In the power limit scenario, it can be observed that despite the limit on *inv 3*, the frequency response of the generators is the same as that of the unconstrained case in Fig. 5.4b, that is, about 0.2 Hz of negative deviation and about 0.05 Hz of positive deviation. In the energy limit scenario, the frequency response is slightly different from the unconstrained scenario in Fig. 5.4 as the positive deviation extends to about 0.1 Hz. Despite the limits, the MIPC

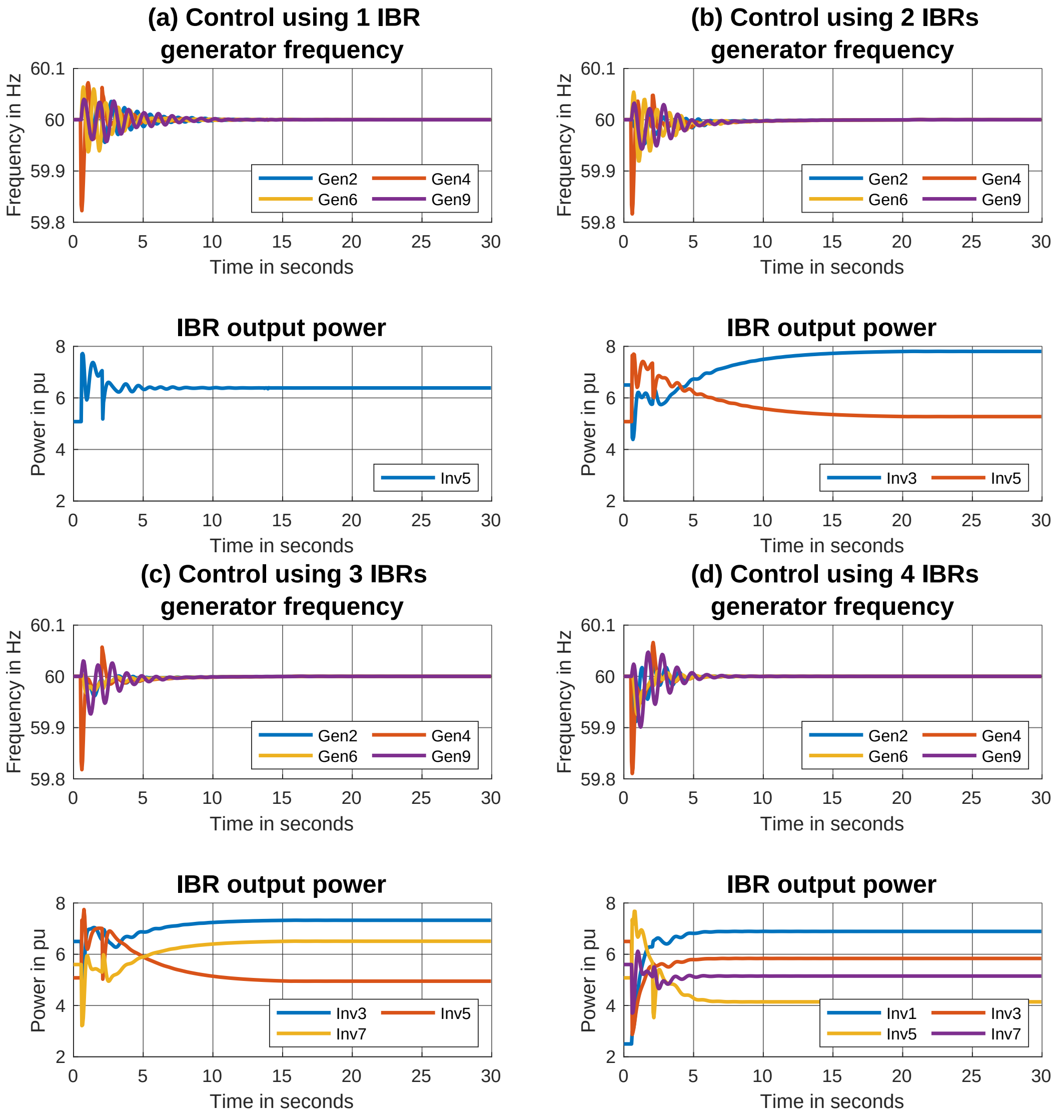

Figure 5.4: Plot showing frequency response of some select generators and inverter output power using centralized MIPC control strategy in an unconstrained scenario when multiple IBRs are integrated into the NE39 network. *(a)* One IBR connected as inv 5 at bus 34, *(b)* Two IBRs connected as inv 3 and 5 at bus 32 and 34 respectively, *(c)*: Three IBRs connected as inv 3, 5 and 7 at bus 32, 34 and 36 respectively, and *(d)*: Four IBRs connected as inv 1, 3, 5 and 7 at bus 30, 32, 34 and 36 respectively. The power output across the inverter is shared according to the weight assigned to each inverter.

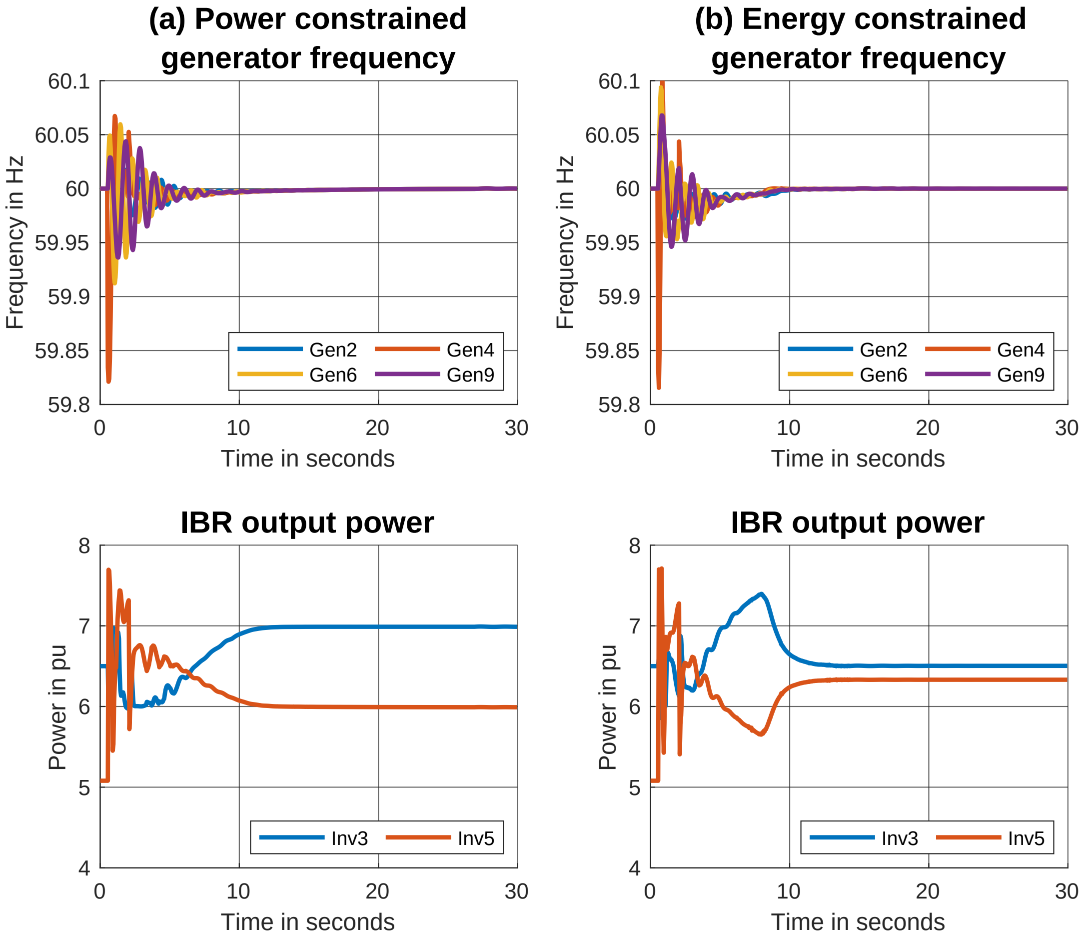

Figure 5.5: Plot showing frequency response of some select generators and inverter output power using MIPC control strategy in a power (*left*) and energy (*right*) constrained scenario when two IBRs are integrated into the NE39 network. The Power limit of *inv 3* is constrained to 7 pu, and the total energy limit of *inv 3* is constrained to 70 pu. The MIPC is able to leverage on other IBRs in the network when there is a limit on one thus ensuring that the same frequency frequency response for the power limit case and an almost similar response for the energy limit case when compared to the unconstrained case in Fig. 5.4b

is able to look ahead and also leverage on other IBR without an active constraint to ensure that the best strategy for an optimal frequency response is achieved.

We further consider a scenario where the centralized control system running the MIPC looses communication with some generators. Fig. 5.6 shows the comparison of the response under this scenario to when a full state communication is available. It can be observed that even under a partial communication scenario, the MIPC controller is able to estimate the impact of the unobserved state as a disturbance and drive the system to stability while keeping the frequency deviation at about 0.2Hz.

5.5.2 Distributed Control

The results shown thus far relies on a centralized MIPC control structure where the algorithm computation is carried out on a centralized system and the optimal power set-point is communicated to the IBRs in the network. Fig. 5.7 shows the frequency response of select generators and the inverter power outputs when two IBRs are integrated to the network under the modified distributed control scenario discussed in 5.4 compared to a centralized control scenario.

It can be observed that the observer model in the MIPC algorithm running on each IBR is able to estimate the unavailable states and also the disturbances, which is reflected as a mismatch between the available state measurement and the model predicted state. A combination of these estimates is able to capture enough of the system level information to determine what the optimal power output of each inverter should be. It can also be observed that at the start of the disturbance, the inverter output power response initially varies significantly compared to the centralized case but is able to eventually settle to the same power output.

We conjecture that the synchronizing properties of the electric grid [141] as well as its full connectivity enables the distributed MIPC controllers on each IBR individually arrive at steady state conditions.

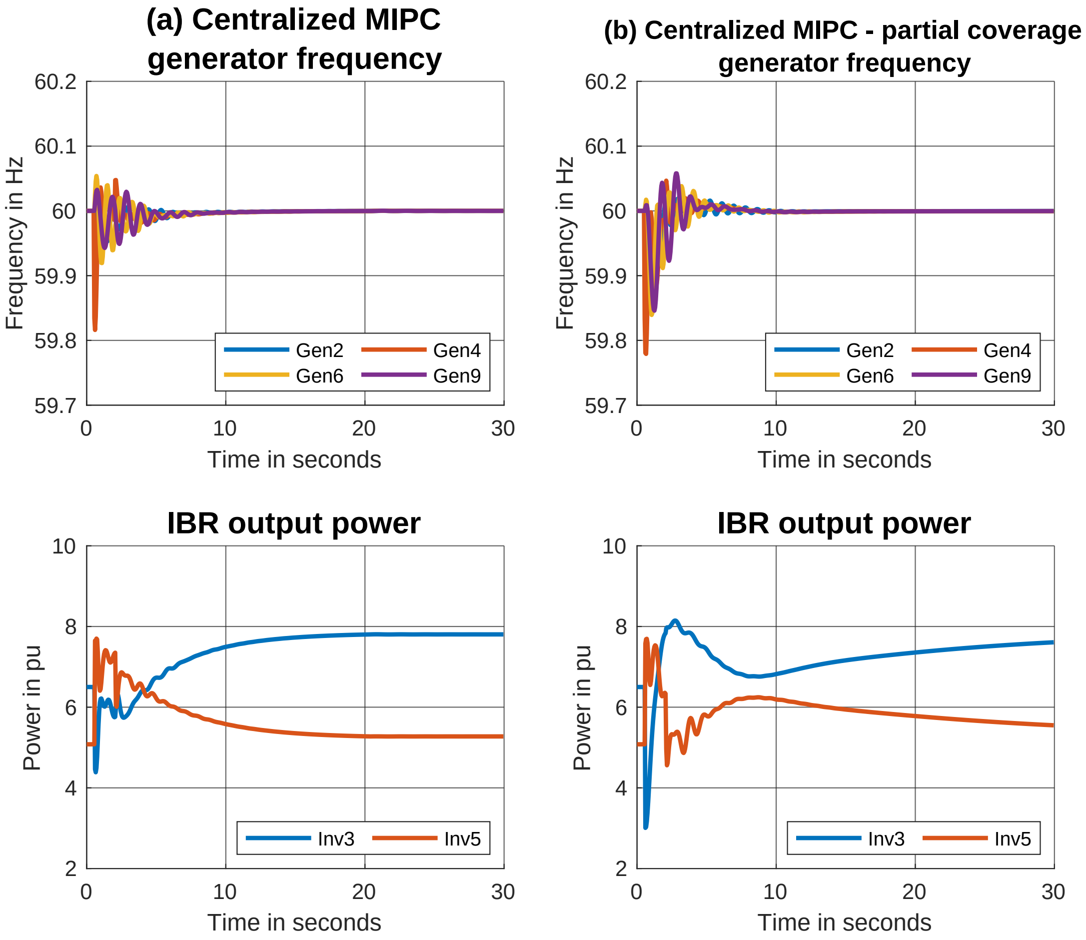

Figure 5.6: Plot showing a comparison of the frequency response of some select generators and inverter output powers using centralized MIPC control strategy in a full communication (*left*) and limited communication (*right*) scenario.

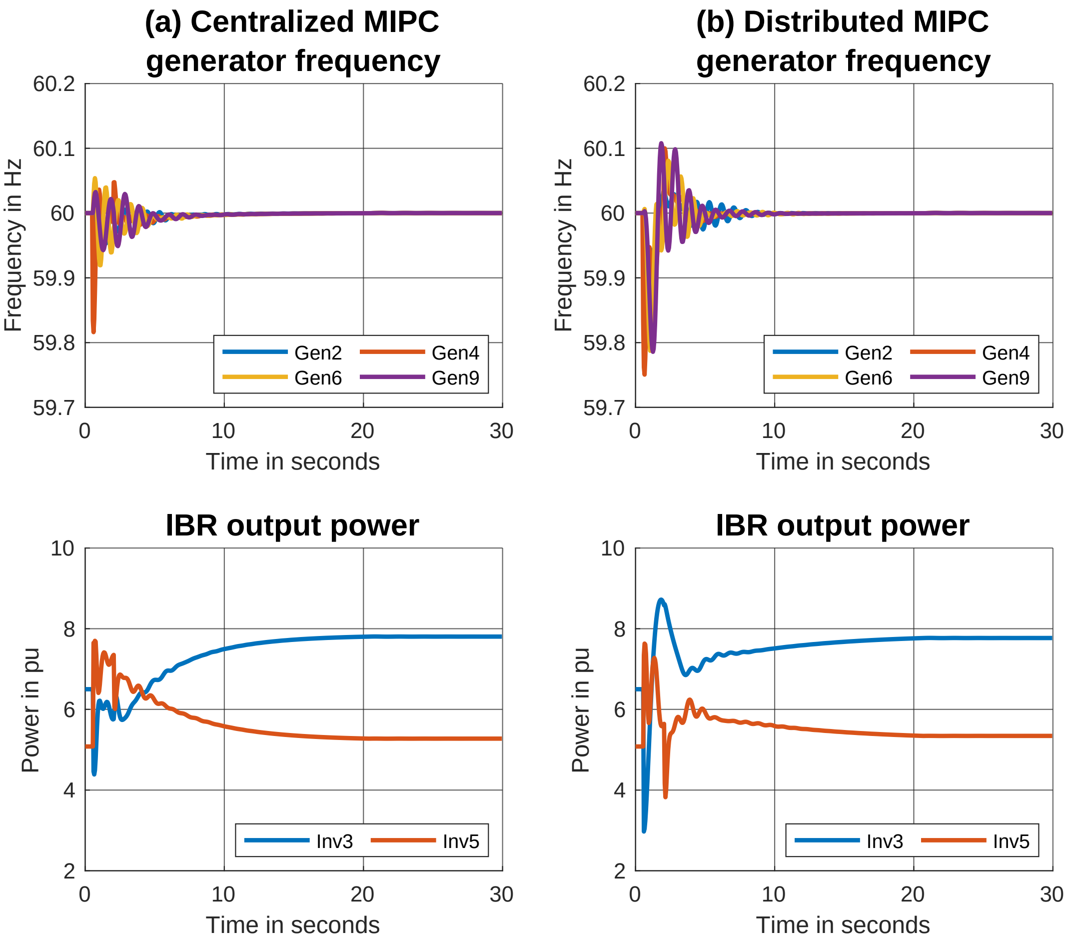

Figure 5.7: Plot showing a comparison of the frequency response of some select generators and inverter output powers using MIPC control strategy in a centralized control scenario (*left*) and a distributed control scenario (*right*) when two IBRs are integrated into the NE39 network with each individual IBRs running MIPC control but do not communicate with each other.

5.6 Conclusion

In this chapter, we extended the functionality of our previously proposed control strategy to handle coordination and control of multiple IBRs participating in frequency control at different locations in the grid in both a centralized and distributed control scenario. We validated the performance of this controller on the IEEE 39-bus system and showed that its control performance does not deteriorate with the addition of more IBRs (actuators) even under distributed control scenarios.

Future works will explore optimal location specific deployment of IBRs as it can be seen that the location of the IBR determines the significance of its participation in frequency control. Also more theoretical work on stability guarantees both in a centralized and distributed framework especially in a network with strong interactions amongst the nodes due to the synchronizing properties of the power system structure.

Chapter 6

CONCLUSION

6.1 Conclusion

This dissertation has addressed the participation of inverter based resources (IBRs) in providing frequency response in a low-inertia power systems. It achieves this by proposing efficient control and optimization algorithms for the frequency response control loop of the inverters through which these resources are connected to the grid, and validates the proposed algorithms on standard IEEE test cases. It adopts the definition of IBRs as asynchronous renewable energy resources (RES) and energy storage systems typically connected via power electronics to the grid. Based on this definition, it assumes each IBR is a combination of renewable resources such as wind and solar, and energy storage such as batteries to ensure available capacity to participate in frequency response. The control and optimization approaches proposed are divided into two categories: optimizing the performance of the virtual synchronous machine (VSM) and a novel control strategy termed inverter power control (IPC).

The first approach detailed in chapter 3 focused on optimizing the virtual inertia and gain coefficients of the VSM, using the network's $\mathcal{H}_2$ norm as a proxy for its time domain frequency control objectives such as maximum frequency deviation, rate of change of frequency (ROCOF) and settling time. Due to the non-convexity of the resulting optimization problem, an efficient gradient with respect to the virtual gain was proposed, derived and used in computing the virtual gains via projected gradient descent due to the box constraint property of the gains' limits. The major conclusion using this approach is the trade-off in competing multi-objective scenario, that is, a scenario where it is not possible to simultaneously achieve two or more objectives. In this case, a Pareto front is achieved by the optimization problem as reflected in the optimal virtual inertia assignment which achieves a balance between having a fast settling time but high frequency nadir and fast ROCOF, and a slow settling time but low frequency nadir and slow ROCOF when validated in a test system.

The second approach detailed in chapter 4 and 5 proposed a novel control strategy based on model predictive control (MPC) termed inverter power control (IPC) which relies on state measurements to directly determine the active-power set-point of the IBRs. This IPC control strategy sought to alleviate the fundamental drawback of the VSM approach that constrains the IBRs to behave like synchronous machines (second-order oscillator) when responding to frequency events, thus limiting the potentials of the fast acting and flexible IBRs. The mathematical framework for the IPC controller based on MPC was first setup for a single IBR integration to the system in conjunction with an observer design to enhance the robustness of the algorithm in situations of model mismatch, noise and limited communications. This algorithm was further extended to cater to a more realistic scenario where there are multiple IBRs connected at various location in the grid and showed how this controller, termed MIPC can be modified to function in a distributed control scenario with each IBR running the MIPC and optimizes over the global objectives. Case studies via simulations was conducted to validate the performance of the IPC controller which demonstrated the superiority of the IPC to the VSM especially its ability to include hard constraints, such as power and energy limits, that might be encountered during operation to the optimization problem. The case studies also showed that the MIPC controller running in a centralized configuration was able to coordinate and control the multiple IBRs and did not deteriorate the overall network performance compared to a single IBR running the IPC, and while the performance in the distributed control case had a bit more deviation compared to the centralized case, it also did not deteriorate the overall network performance significantly.

A noteworthy conclusion from this dissertation is that using either of the control approaches proposed, shows that replacing conventional generators with renewable energy resources would not necessarily result in a decline in frequency control response in the electric grid. Rather, if the resource can be optimized coupled with availability of data, then much better responses are possible, thus facilitating the transition to more sustainable energy sources.

6.2 Future Works

Some potential ways of extending the research carried out in this dissertation are as follows:

6.2.1 Theoretical Stability Guarantees for Networks with IBR integration

In literature, the transient stability of power systems and synchronization of non-uniform Kuramoto oscillators have been shown under certain assumptions to be closely related problems [141–143]. These analysis rely on having only synchronous machines in the network with rotor angle and frequency as states, second order oscillator properties of these synchronous machines and a complete graph network topology based on the transmission line interconnections between the generators. Under this framework, some necessary and sufficient conditions for stability are guaranteed based on system parameters such as damping and inertia and network topology [141, 142].

In the present day power systems with renewable energy resources connected to the grid via asynchronous devices - inverters, which do not have inertia and damping components, a new stability analysis is required. Questions to be answered include: stability guarantees in a network with synchronous and asynchronous sources, impact on stability with increased asynchronous sources, stability guarantee under the actions of external controllers such as the (M)IPC. This dissertation shows via simulation that the above question are true but a rigorous theoretical analysis is required to determine the conditions under which stability will hold. In chapter 4 of this dissertation, a mathematical model of the dynamics of a power systems with synchronous and asynchronous sources based on a modified swing equation was derived where the inverter angle is transformed to become the input to the system. This model shows promises of being used as a first step for the required theoretical analysis.

6.2.2 IBR placement

In order for IBRs to participate effectively in providing frequency control response, they have to be placed strategically in the network regardless of the control strategy. Some research effort has gone into trying to solve this problem [2, 80] and chapter 3 of this dissertation by extension attempts to address this problem [79].

These methods typically rely on a Kron reducing a network to only buses with generators and also assumes the IBRs have some form of inertia and damping coefficient such that it can be represented as a synchronous machine, therefore making it amenable to popular optimal placement algorithms based on eigenvalue properties. Realistically though, IBRs do not physically have inertia and damping coefficient and the concept of virtual inertia and damping coefficient only manifest themselves in frequency response conditions. Also, the optimal location to cite the IBR might be at a node without an active component which has already been lost in the Kron reducing process of the network. In this dissertation, the IBRs were arbitrarily placed but a better placement approach that does not make these assumptions and is robust to disturbance location is required to enable the IBR with control to respond to frequency events adequately.

6.2.3 Local Frequency Estimation for Stability Analysis

In traditional power systems stability simulation studies, frequency control actions typically rely on local frequency and rotor angle estimates of the synchronous machines and can be obtained as part of the states from dynamic models of the machines. In a mixed source network, in order for IBRs which are asynchronous in nature to participate in frequency control, they will require an estimate of the grid frequency (or frequency deviation from nominal) from voltage measurements at their point of interconnection to the grid. This is typically done using phase locked loop (PLL). For transient stabilities simulation studies, some works have proposed integrating the full IBR model, which includes the PLL model, in conjunction with the synchronous machine models [124]. The drawback of this strategy is that using the full sixth order state of each IBRs can be computationally cumbersome and the timescale difference between the machines and IBR can also introduce some challenges. Also the use of PLLs introduces errors due to the calculation of numerical derivatives carried out and also introduces a phase delay in the resulting measurements [134,135]. The center of inertia (COI) concept, which was utilized in this dissertation, is a widely used technique [144] because its ease of computation but due its inertia weighted nature, it averages out important trends and also assumes the frequency is the same across all nodes regardless of its location in the system.

Therefore an easier and less computationally intensive process is required to accurately determine the local frequency estimate at different buses in the network from dynamic states of the synchronous machine. Some machine learning algorithms could possibly be applied to determine this relationship, or some mathematical frameworks that rely on the network topology and parameters using either real world measurements or simulation measurements. Some research works have proposed some methods to address this [145] but the results captures the general trend not the exact value.

6.2.4 System Identification from Data

In this dissertation and in most power systems control research, it is typical to use the linearized swing equation with an assumption that the system parameters are time-invariant and the system states remain close to the chosen equilibrium. While the inertia component which relies on the physical presence of the generators might be constant all through the control period, the damping coefficient is typically time varying since it is not a physical quantity but an abstraction that depends on a combination of factors in the system [146]. As the electric grid evolves due to the integration of renewable energy sources, and as such operating at the limits, these assumptions will no longer be tenable.

The increasing availability of phasor measurement unit (PMU) data [147] makes it possible to identify the time-varying parameters in the system and potentially provide an accuracy bound on the uncertainty in the system models. For controllers that capitalize on the structure of the network or utilizes the parameter in the state-space model, extracting the system model in its original basis is required for effective control. While various techniques, typically using singular value decomposition and least squares methods, exist in literature to identify system models and also hybrid models from data [148–151], they often return a model that maps the input-output relationship without considering the physical interpretations of the model and suffer from the non-uniqueness of the identified system model. This then requires some complicated techniques to transform the model to its original basis by finding the appropriate similarity transformation. Also in most identification techniques, input-output data is required to identify the system model but for the power systems case, there is only potential access to output data from the PMU as there is no knowledge in advance of the disturbance input to the system. Therefore, more research work is required to identify the state-space system model in its original basis from output-only data and also estimate some uncertainty bound for robust control applications.

BIBLIOGRAPHY

[1] Linga, Vikram, "Eia expects u.s. electricity generation from renewables to soon surpass nuclear and coal." https://www.eia.gov/todayinenergy/detail.php?id=41533, Jan 2020. [Online; accessed 10-April-2020].

[2] B. K. Poolla, S. Bolognani, and F. Dorfler, "Optimal placement of virtual inertia in power grids," *IEEE Transactions on Automatic Control*, 2017.

[3] Bowman, Michelle, "Eia projects that renewables will provide nearly half of world electricity by 2050." https://www.eia.gov/todayinenergy/detail.php?id=41533, Oct 2019. [Online; accessed 05-April-2020].

[4] N. Mararakanye and B. Bekker, "Renewable energy integration impacts within the context of generator type, penetration level and grid characteristics," *Renewable and Sustainable Energy Reviews*, vol. 108, pp. 441–451, 2019.

[5] I. Dudurych, M. Burke, L. Fisher, M. Eager, and K. Kelly, "Operational security challenges and tools for a synchronous power system with high penetration of non-conventional sources," *CIGRE Science & Engineering*, vol. 7, 2017.

[6] L. Bird, M. Milligan, and D. Lew, "Integrating variable renewable energy: Challenges and solutions," tech. rep., National Renewable Energy Lab.(NREL), Golden, CO (United States), 2013.

[7] P. Meibom, H. V. Larsen, R. Barth, H. Brand, A. Tuohy, and E. Ela, "Advanced unit commitment strategies in the united states eastern interconnection," tech. rep., National Renewable Energy Lab.(NREL), Golden, CO (United States), 2011.

[8] R. Seguin, J. Woyak, D. Costyk, J. Hambrick, and B. Mather, "High-penetration pv integration handbook for distribution engineers," tech. rep., National Renewable Energy Lab.(NREL), Golden, CO (United States), 2016.

[9] Y. Liu, J. Bebic, B. Kroposki, J. De Bedout, and W. Ren, "Distribution system voltage performance analysis for high-penetration pv," in *2008 IEEE Energy 2030 Conference*, pp. 1–8, IEEE, 2008.

[10] A. E. M. Operator, "Black system south australia 28 september 2016," *Report of the Australian Energy Market Operator Limited (AEMO)*, 2017.

[11] J. Schiffer, D. Zonetti, R. Ortega, A. M. Stanković, T. Sezi, and J. Raisch, "A survey

on modeling of microgridsfrom fundamental physics to phasors and voltage sources," *Automatica*, vol. 74, pp. 135–150, 2016.

[12] A. M. Bouzid, J. M. Guerrero, A. Cheriti, M. Bouhamida, P. Sicard, and M. Benghanem, "A survey on control of electric power distributed generation systems for microgrid applications," *Renewable and Sustainable Energy Reviews*, vol. 44, pp. 751–766, 2015.

[13] J. Aho, A. Buckspan, J. Laks, P. Fleming, Y. Jeong, F. Dunne, M. Churchfield, L. Pao, and K. Johnson, "A tutorial of wind turbine control for supporting grid frequency through active power control," in *2012 American Control Conference (ACC)*, pp. 3120–3131, IEEE, 2012.

[14] N. R. Guideline, "Bps-connected inverter-based resource performance," 2018.

[15] J. Machowski, J. Bialek, and J. Bumby, *Power system dynamics: stability and control*. John Wiley & Sons, 2011.

[16] P. Tielens and D. Van Hertem, "The relevance of inertia in power systems," *Renewable and Sustainable Energy Reviews*, vol. 55, pp. 999–1009, 2016.

[17] F. Milano, F. Dörfler, G. Hug, D. J. Hill, and G. Verbič, "Foundations and challenges of low-inertia systems," in *2018 Power Systems Computation Conference (PSCC)*, pp. 1–25, IEEE, 2018.

[18] M. Nedd, C. Booth, and K. Bell, "Potential solutions to the challenges of low inertia power systems with a case study concerning synchronous condensers," in *2017 52nd International Universities Power Engineering Conference (UPEC)*, pp. 1–6, IEEE, 2017.

[19] H. T. Nguyen, G. Yang, A. H. Nielsen, and P. H. Jensen, "Frequency stability improvement of low inertia systems using synchronous condensers," in *2016 IEEE International Conference on Smart Grid Communications (SmartGridComm)*, pp. 650–655, IEEE, 2016.

[20] W. Li, P. Du, and N. Lu, "Design of a new primary frequency control market for hosting frequency response reserve offers from both generators and loads," *IEEE Transactions on Smart Grid*, vol. 9, no. 5, pp. 4883–4892, 2017.

[21] R. Maliszewski, R. Dunlop, and G. Wilson, "Frequency actuated load shedding and restoration part i-philosophy," *IEEE Transactions on power apparatus and systems*, no. 4, pp. 1452–1459, 1971.

[22] F. Mendes, A. Gomes, and A. G. Martins, "The role of demand response in power systems with low inertia," in *2018 International Conference on Smart Energy Systems and Technologies (SEST)*, pp. 1–6, IEEE, 2018.

[23] F. Teng, M. Aunedi, D. Pudjianto, and G. Strbac, "Benefits of demand-side response

in providing frequency response service in the future gb power system," *Frontiers in Energy Research*, vol. 3, p. 36, 2015.

[24] U. Tamrakar, D. Shrestha, M. Maharjan, B. P. Bhattarai, T. M. Hansen, and R. Tonkoski, "Virtual inertia: Current trends and future directions," *Applied Sciences*, vol. 7, no. 7, p. 654, 2017.

[25] M. Dreidy, H. Mokhlis, and S. Mekhilef, "Inertia response and frequency control techniques for renewable energy sources: A review," *Renewable and Sustainable Energy Reviews*, vol. 69, pp. 144–155, 2017.

[26] J. Van de Vyver, J. D. De Kooning, B. Meersman, L. Vandevelde, and T. L. Vandoorn, "Droop control as an alternative inertial response strategy for the synthetic inertia on wind turbines," *IEEE Transactions on Power Systems*, vol. 31, no. 2, pp. 1129–1138, 2015.

[27] J. W. Simpson-Porco, F. Dörfler, and F. Bullo, "Synchronization and power sharing for droop-controlled inverters in islanded microgrids," *Automatica*, vol. 49, no. 9, pp. 2603–2611, 2013.

[28] R. Ofir, U. Markovic, P. Aristidou, and G. Hug, "Droop vs. virtual inertia: Comparison from the perspective of converter operation mode," in *2018 IEEE International Energy Conference (ENERGYCON)*, IEEE, 2018.

[29] R. Majumder, A. Ghosh, G. Ledwich, and F. Zare, "Operation and control of hybrid microgrid with angle droop controller," 2010.

[30] S. Sivaranjani, E. Agarwal, L. Xie, V. Gupta, and P. Antsaklis, "Mixed voltage angle and frequency droop control for transient stability of interconnected microgrids with loss of pmu measurements," *arXiv preprint arXiv:1803.02918*, 2018.

[31] M. Van Wesenbeeck, S. De Haan, P. Varela, and K. Visscher, "Grid tied converter with virtual kinetic storage," in *PowerTech, 2009 IEEE Bucharest*, pp. 1–7, IEEE, 2009.

[32] K. Sakimoto, Y. Miura, and T. Ise, "Stabilization of a power system with a distributed generator by a virtual synchronous generator function," in *Power Electronics and ECCE Asia (ICPE & ECCE), 2011 IEEE 8th International Conference on*, pp. 1498–1505, IEEE, 2011.

[33] H. Bevrani, T. Ise, and Y. Miura, "Virtual synchronous generators: A survey and new perspectives," *International Journal of Electrical Power & Energy Systems*, vol. 54, pp. 244–254, 2014.

[34] J. H. Eto, "Use of frequency response metrics to assess the planning and operating requirements for reliable integration of variable renewable generation," *Lawrence Berkeley National Laboratory*, 2011.

[35] P. Kundur, "Power system control and stability," *New York: McGraw*, 1994.

[36] E. R. C. of Texas (ERCOT), "Future ancillary services in ercot," 2013.

[37] S. EirGrid, "Rocof alternative and complementary solutions project," tech. rep., Technical report March, EIRGRID, 2016.

[38] N. Miller, D. Lew, and R. Piwko, "Technology capabilities for fast frequency response," *GE Energy Consulting, Tech. Rep*, vol. 3, pp. 10–60, 2017.

[39] F. Statnett *et al.*, "Challenges and opportunities for the nordic power system," *Technical Report*, 2016.

[40] C. Corvin, "Slac synchronous condenser," in *Proceedings Particle Accelerator Conference*, vol. 4, pp. 2114–2116, IEEE, 1995.

[41] S. Teleke, T. Abdulahovic, T. Thiringer, and J. Svensson, "Dynamic performance comparison of synchronous condenser and svc," *IEEE Transactions on Power Delivery*, vol. 23, no. 3, pp. 1606–1612, 2008.

[42] P.-L. Nguyen, Q.-C. Zhong, F. Blaabjerg, and J. M. Guerrero, "Synchronverter-based operation of statcom to mimic synchronous condensers," in *2012 7th IEEE Conference on Industrial Electronics and Applications (ICIEA)*, pp. 942–947, IEEE, 2012.

[43] H. Zhang, J.-P. Hasler, N. Johansson, L. Ängquist, and H.-P. Nee, "Frequency response improvement with synchronous condenser and power electronics converters," in *2017 IEEE 3rd International Future Energy Electronics Conference and ECCE Asia (IFEEC 2017-ECCE Asia)*, pp. 1002–1007, IEEE, 2017.

[44] Y. Liu, S. Yang, S. Zhang, and F. Z. Peng, "Comparison of synchronous condenser and statcom for inertial response support," in *2014 IEEE Energy Conversion Congress and Exposition (ECCE)*, pp. 2684–2690, IEEE, 2014.

[45] R. Yan, T. K. Saha, N. Modi, *et al.*, "Frequency response and its enhancement using synchronous condensers in presence of high wind penetration," in *2015 IEEE Power & Energy Society General Meeting*, pp. 1–5, IEEE, 2015.

[46] J. Banks, A. Bruce, and I. MacGill, "Fast frequency response markets for high renewable energy penetrations in the future australian nem," in *Proceedings of the Asia Pacific Solar Research Conference*, 2017.

[47] V. Trovato, I. M. Sanz, B. Chaudhuri, and G. Strbac, "Advanced control of thermostatic loads for rapid frequency response in great britain," *IEEE Transactions on Power Systems*, vol. 32, no. 3, pp. 2106–2117, 2016.

[48] Q. Qdr, "Benefits of demand response in electricity markets and recommendations for achieving them," *US Dept. Energy, Washington, DC, USA, Tech. Rep*, 2006.

[49] M. Donnelly, D. J. Trudnowski, S. Mattix, and J. E. Dagle, “Autonomous demand response for primary frequency regulation,” tech. rep., Pacific Northwest National Lab.(PNNL), Richland, WA (United States), 2012.

[50] P. Daly, H. W. Qazi, and D. Flynn, “Rocof-constrained scheduling incorporating non-synchronous residential demand response,” *IEEE Transactions on Power Systems*, vol. 34, no. 5, pp. 3372–3383, 2019.

[51] V. Trovato, S. H. Tindemans, and G. Strbac, “Demand response contribution to effective inertia for system security in the gb 2020 gone green scenario,” in *IEEE PES ISGT Europe 2013*, pp. 1–5, IEEE, 2013.

[52] A. Saffarian and M. Sanaye-Pasand, “Enhancement of power system stability using adaptive combinational load shedding methods,” *IEEE Transactions on Power Systems*, vol. 26, no. 3, pp. 1010–1020, 2010.

[53] U. Rudez and R. Mihalic, “Wams-based underfrequency load shedding with short-term frequency prediction,” *IEEE Transactions on Power Delivery*, vol. 31, no. 4, pp. 1912–1920, 2015.

[54] S. Li, F. Tang, Y. Shao, and Q. Liao, “Adaptive under-frequency load shedding scheme in system integrated with high wind power penetration: Impacts and improvements,” *Energies*, vol. 10, no. 9, p. 1331, 2017.

[55] A. Drabandsari and T. Amraee, “Optimal setting of under frequency load shedding relays in low inertia networks,” in *2018 Smart Grid Conference (SGC)*, pp. 1–6, IEEE, 2018.

[56] S. Hossain, M. Hossain, E. Fernandez, and M. S. Rahman, “Design and analysis of an ufls scheme for low-inertia based power grid,” in *2018 Australasian Universities Power Engineering Conference (AUPEC)*, pp. 1–6, IEEE, 2018.

[57] M. Donnelly, D. Harvey, R. Munson, and D. Trudnowski, “Frequency and stability control using decentralized intelligent loads: Benefits and pitfalls,” in *IEEE PES general meeting*, pp. 1–6, IEEE, 2010.

[58] B. Kroposki, B. Johnson, Y. Zhang, V. Gevorgian, P. Denholm, B.-M. Hodge, and B. Hannegan, “Achieving a 100% renewable grid: Operating electric power systems with extremely high levels of variable renewable energy,” *IEEE Power and Energy Magazine*, vol. 15, no. 2, pp. 61–73, 2017.

[59] J. Rocabert, A. Luna, F. Blaabjerg, and P. Rodriguez, “Control of power converters in ac microgrids,” *IEEE transactions on power electronics*, vol. 27, no. 11, pp. 4734–4749, 2012.

[60] I. A. Hiskens and E. M. Fleming, “Control of inverter-connected sources in autonomous microgrids,” in *2008 American Control Conference*, pp. 586–590, IEEE, 2008.

[61] A. Yazdani and R. Iravani, *Voltage-sourced converters in power systems*, vol. 34. Wiley Online Library, 2010.

[62] A. Ademola-Idowu and B. Zhang, "Frequency stability using inverter power control in low-inertia power systems," *arXiv preprint arXiv:1909.12810*, 2019.

[63] J. F. Conroy and R. Watson, "Frequency response capability of full converter wind turbine generators in comparison to conventional generation," *IEEE transactions on power systems*, vol. 23, no. 2, pp. 649–656, 2008.

[64] M. Surprenant, I. Hiskens, and G. Venkataramanan, "Phase locked loop control of inverters in a microgrid," in *Energy Conversion Congress and Exposition (ECCE), 2011 IEEE*, pp. 667–672, IEEE, 2011.

[65] Y. Sun, X. Hou, J. Yang, H. Han, M. Su, and J. M. Guerrero, "New perspectives on droop control in ac microgrid," *IEEE Transactions on Industrial Electronics*, vol. 64, no. 7, pp. 5741–5745, 2017.

[66] K. De Brabandere, B. Bolsens, J. Van den Keybus, A. Woyte, J. Driesen, and R. Belmans, "A voltage and frequency droop control method for parallel inverters," *IEEE Transactions on power electronics*, vol. 22, no. 4, pp. 1107–1115, 2007.

[67] R. Majumder, A. Ghosh, G. Ledwich, and F. Zare, "Angle droop versus frequency droop in a voltage source converter based autonomous microgrid," in *Power & Energy Society General Meeting, 2009. PES'09. IEEE*, pp. 1–8, IEEE, 2009.

[68] N. Vazquez, S. S. Yu, T. K. Chau, T. Fernando, and H. H.-C. Iu, "A fully decentralized adaptive droop optimization strategy for power loss minimization in microgrids with pv-bess," *IEEE Transactions on Energy Conversion*, vol. 34, no. 1, pp. 385–395, 2018.

[69] F. Chen, M. Chen, Q. Li, K. Meng, Y. Zheng, J. M. Guerrero, and D. Abbott, "Cost-based droop schemes for economic dispatch in islanded microgrids," *IEEE Transactions on Smart Grid*, vol. 8, no. 1, pp. 63–74, 2016.

[70] S. S. Guggilam, C. Zhao, E. DallAnese, Y. C. Chen, and S. V. Dhople, "Optimizing power–frequency droop characteristics of distributed energy resources," *IEEE Transactions on Power Systems*, vol. 33, no. 3, pp. 3076–3086, 2017.

[71] M. A. Hossain, H. R. Pota, W. Issa, and M. J. Hossain, "Overview of ac microgrid controls with inverter-interfaced generations," *Energies*, vol. 10, no. 9, p. 1300, 2017.

[72] S. D'Arco, J. A. Suul, and O. B. Fosso, "Control system tuning and stability analysis of virtual synchronous machines," in *Energy Conversion Congress and Exposition (ECCE), 2013 IEEE*, pp. 2664–2671, IEEE, 2013.

[73] Q.-C. Zhong, "Virtual synchronous machines: A unified interface for grid integration," *IEEE Power Electronics Magazine*, vol. 3, no. 4, pp. 18–27, 2016.

[74] Q.-C. Zhong and G. Weiss, “Synchronverters: Inverters that mimic synchronous generators,” *IEEE transactions on industrial electronics*, vol. 58, no. 4, pp. 1259–1267, 2010.

[75] J. Alipoor, Y. Miura, and T. Ise, “Power system stabilization using virtual synchronous generator with alternating moment of inertia,” *IEEE Journal of Emerging and Selected Topics in Power Electronics*, vol. 3, no. 2, pp. 451–458, 2015.

[76] H.-P. Beck and R. Hesse, “Virtual synchronous machine,” in *2007 9th International Conference on Electrical Power Quality and Utilisation*, pp. 1–6, IEEE, 2007.

[77] S. D’Arco and J. A. Suul, “Equivalence of virtual synchronous machines and frequency-droops for converter-based microgrids,” *IEEE Transactions on Smart Grid*, vol. 5, no. 1, pp. 394–395, 2013.

[78] K. S. Ratnam, K. Palanisamy, and G. Yang, “Future low-inertia power systems: Requirements, issues, and solutions-a review,” *Renewable and Sustainable Energy Reviews*, vol. 124, p. 109773, 2020.

[79] A. Ademola-Idowu and B. Zhang, “Optimal design of virtual inertia and damping coefficients for virtual synchronous machines,” in *Power and Energy Society General Meeting*, 2018.

[80] T. Borsche and F. Dörfler, “On placement of synthetic inertia with explicit time-domain constraints,” *arXiv preprint arXiv:1705.03244*, 2017.

[81] F. Wang, L. Zhang, X. Feng, and H. Guo, “An adaptive control strategy for virtual synchronous generator,” *IEEE Transactions on Industry Applications*, vol. 54, no. 5, pp. 5124–5133, 2018.

[82] D. Li, Q. Zhu, S. Lin, and X. Bian, “A self-adaptive inertia and damping combination control of vsg to support frequency stability,” *IEEE Transactions on Energy Conversion*, vol. 32, no. 1, pp. 397–398, 2017.

[83] C. Zhang, Y. Yang, H. Miao, and X. Yuan, “An improved adaptive inertia and damping control strategy for virtual synchronous generator,” in *2018 13th IEEE Conference on Industrial Electronics and Applications (ICIEA)*, pp. 322–328, IEEE, 2018.

[84] M. E. Aboul-Ela, A. Sallam, J. D. McCalley, and A. Fouad, “Damping controller design for power system oscillations using global signals,” *IEEE Transactions on Power Systems*, vol. 11, no. 2, pp. 767–773, 1996.

[85] I. Kamwa, R. Grondin, and Y. Hébert, “Wide-area measurement based stabilizing control of large power systems-a decentralized/hierarchical approach,” *IEEE Transactions on power systems*, vol. 16, no. 1, pp. 136–153, 2001.

[86] Y. Zhang and A. Bose, "Design of wide-area damping controllers for interarea oscillations," *IEEE transactions on power systems*, vol. 23, no. 3, pp. 1136–1143, 2008.

[87] A. F. Snyder, N. Hadjsaïd, D. Georges, L. Mili, A. G. Phadke, O. Faucon, and S. Vitet, "Inter-area oscillation damping with power system stabilizers and synchronized phasor measurements," in *POWERCON'98. 1998 International Conference on Power System Technology. Proceedings (Cat. No. 98EX151)*, vol. 2, pp. 790–794, IEEE, 1998.

[88] M. A. Smith, *Improved dynamic stability using FACTS devices with phasor measurement feedback*. PhD thesis, Virginia Tech, 1994.

[89] N. Yang, Q. Liu, and J. D. McCalley, "Tcsc controller design for damping interarea oscillations," *IEEE Transactions on Power Systems*, vol. 13, no. 4, pp. 1304–1310, 1998.

[90] G. Taranto, J. Chow, and H. Othman, "Robust decentralized control design for damping power system oscillations," in *Proceedings of 1994 33rd IEEE Conference on Decision and Control*, vol. 4, pp. 4080–4085, IEEE, 1994.

[91] I. Kamwa, R. Grondin, D. Asber, J. Gingras, and G. Trudel, "Large-scale active-load modulation for angle stability improvement," *IEEE transactions on power systems*, vol. 14, no. 2, pp. 582–590, 1999.

[92] R. B. Bobba, J. Dagle, E. Heine, H. Khurana, W. H. Sanders, P. Sauer, and T. Yardley, "Enhancing grid measurements: Wide area measurement systems, naspinet, and security," *IEEE Power and Energy Magazine*, vol. 10, no. 1, pp. 67–73, 2011.

[93] M. V. Mynam, A. Harikrishna, and V. Singh, "Synchrophasors redefining scada systems," *Journal International Association on Electricity Generation, Transmission and Distribution*, vol. 26, no. 2, pp. 22–28, 2013.

[94] J. De La Ree, V. Centeno, J. S. Thorp, and A. G. Phadke, "Synchronized phasor measurement applications in power systems," *IEEE Transactions on smart grid*, vol. 1, no. 1, pp. 20–27, 2010.

[95] F. Aminifar, M. Fotuhi-Firuzabad, A. Safdarian, A. Davoudi, and M. Shahidehpour, "Synchrophasor measurement technology in power systems: Panorama and state-of-the-art," *IEEE Access*, vol. 2, pp. 1607–1628, 2014.

[96] K. Martin, D. Hamai, M. Adamiak, S. Anderson, M. Begovic, G. Benmouyal, G. Brunello, J. Burger, J. Cai, B. Dickerson, *et al.*, "Exploring the ieee standard c37. 118–2005 synchrophasors for power systems," *IEEE transactions on power delivery*, vol. 23, no. 4, pp. 1805–1811, 2008.

[97] N. C. Seeley, C. Craig, and T. Rainey, "Advances in power generator control: Precise control of power systems islands using time-synchronized measurements," *IEEE Industry Applications Magazine*, vol. 20, no. 2, pp. 44–52, 2013.

[98] F. Dörfler, M. R. Jovanović, M. Chertkov, and F. Bullo, "Sparsity-promoting optimal wide-area control of power networks," *IEEE Transactions on Power Systems*, vol. 29, no. 5, pp. 2281–2291, 2014.

[99] D. Molina, G. K. Venayagamoorthy, J. Liang, and R. G. Harley, "Intelligent local area signals based damping of power system oscillations using virtual generators and approximate dynamic programming," *IEEE Transactions on Smart Grid*, vol. 4, no. 1, pp. 498–508, 2013.

[100] M. Jha, S. Chakrabarti, and E. Kyriakides, "Estimation of the rotor angle of a synchronous generator by using pmu measurements," in *2015 IEEE Eindhoven PowerTech*, pp. 1–6, IEEE, 2015.

[101] V. Venkatasubramanian and R. G. Kavasseri, "Direct computation of generator internal dynamic states from terminal measurements," in *37th Annual Hawaii International Conference on System Sciences, 2004. Proceedings of the*, pp. 6–pp, IEEE, 2004.

[102] G. Rinaldi, P. P. Menon, C. Edwards, and A. Ferrara, "Sliding mode based dynamic state estimation for synchronous generators in power systems," *IEEE control systems letters*, vol. 2, no. 4, pp. 785–790, 2018.

[103] J. Lavenius and L. Vanfretti, "Pmu-based estimation of synchronous machines unknown inputs using a nonlinear extended recursive three-step smoother," *IEEE Access*, vol. 6, pp. 57123–57136, 2018.

[104] A. Del Angel, P. Geurts, D. Ernst, M. Glavic, and L. Wehenkel, "Estimation of rotor angles of synchronous machines using artificial neural networks and local pmu-based quantities," *Neurocomputing*, vol. 70, no. 16-18, pp. 2668–2678, 2007.

[105] Z. Huang, K. Schneider, and J. Nieplocha, "Feasibility studies of applying kalman filter techniques to power system dynamic state estimation," in *2007 International Power Engineering Conference (IPEC 2007)*, pp. 376–382, IEEE, 2007.

[106] K. P. Schneider, Z. Huang, B. Yang, M. Hauer, and Y. Nieplocha, "Dynamic state estimation utilizing high performance computing methods," in *2009 IEEE/PES Power Systems Conference and Exposition*, pp. 1–6, IEEE, 2009.

[107] Z. Huang, P. Du, D. Kosterev, and B. Yang, "Application of extended kalman filter techniques for dynamic model parameter calibration," in *2009 IEEE Power & Energy Society General Meeting*, pp. 1–8, IEEE, 2009.

[108] L. Fan and Y. Wehbe, "Extended kalman filtering based real-time dynamic state and parameter estimation using pmu data," *Electric Power Systems Research*, vol. 103, pp. 168–177, 2013.

[109] E. Ghahremani and I. Kamwa, "Online state estimation of a synchronous generator

using unscented kalman filter from phasor measurements units," *IEEE Transactions on Energy Conversion*, vol. 26, no. 4, pp. 1099–1108, 2011.

[110] A. K. Singh and B. C. Pal, "Decentralized dynamic state estimation in power systems using unscented transformation," *IEEE Transactions on Power Systems*, vol. 29, no. 2, pp. 794–804, 2013.

[111] N. Zhou, D. Meng, and S. Lu, "Estimation of the dynamic states of synchronous machines using an extended particle filter," *IEEE Transactions on Power Systems*, vol. 28, no. 4, pp. 4152–4161, 2013.

[112] F. Milano, A. Ortega, and A. J. Conejo, "Model-agnostic linear estimation of generator rotor speeds based on phasor measurement units," *IEEE Transactions on Power Systems*, vol. 33, no. 6, pp. 7258–7268, 2018.

[113] P. Tielens and D. Van Hertem, "Grid inertia and frequency control in power systems with high penetration of renewables," 2012.

[114] Q.-C. Zhong and G. Weiss, "Synchronverters: Inverters that mimic synchronous generators," *IEEE Transactions on Industrial Electronics*, vol. 58, no. 4, pp. 1259–1267, 2011.

[115] F. Díaz-González, M. Hau, A. Sumper, and O. Gomis-Bellmunt, "Participation of wind power plants in system frequency control: Review of grid code requirements and control methods," *Renewable and Sustainable Energy Reviews*, vol. 34, pp. 551–564, 2014.

[116] J. Morren, S. W. De Haan, W. L. Kling, and J. Ferreira, "Wind turbines emulating inertia and supporting primary frequency control," *IEEE Transactions on power systems*, vol. 21, no. 1, pp. 433–434, 2006.

[117] E. Tegling, B. Bamieh, and D. F. Gayme, "The price of synchrony: Evaluating the resistive losses in synchronizing power networks," *IEEE Transactions on Control of Network Systems*, vol. 2, no. 3, pp. 254–266, 2015.

[118] K. Zhou, J. C. Doyle, K. Glover, *et al.*, *Robust and optimal control*, vol. 40. Prentice hall New Jersey, 1996.

[119] P. Van Dooren, K. A. Gallivan, and P.-A. Absil, "H2-optimal model reduction of mimo systems," *Applied Mathematics Letters*, vol. 21, no. 12, pp. 1267–1273, 2008.

[120] D. Wilson, "Optimum solution of model-reduction problem," in *Proceedings of the Institution of Electrical Engineers*, vol. 117, pp. 1161–1165, IET, 1970.

[121] M. Polycarpou, J. Farrell, and M. Sharma, "On-line approximation control of uncertain nonlinear systems: issues with control input saturation," in *Proceedings of the 2003 American Control Conference, 2003.*, vol. 1, pp. 543–548, IEEE, 2003.

[122] T. Nishikawa and A. E. Motter, “Comparative analysis of existing models for power-grid synchronization,” *New Journal of Physics*, vol. 17, no. 1, p. 015012, 2015.

[123] P. W. Sauer, M. Pai, and J. H. Chow, *Power system dynamics and stability: with synchrophasor measurement and power system toolbox.* John Wiley & Sons, 2017.

[124] H. N. V. Pico and B. B. Johnson, “Transient stability assessment of multi-machine multi-converter power systems,” *IEEE Transactions on Power Systems*, 2019.

[125] B. J. Pierre, H. N. Villegas Pico, R. T. Elliott, J. Flicker, Y. Lin, B. B. Johnson, J. H. Eto, R. H. Lasseter, and A. Ellis, “Bulk power system dynamics with varying levels of synchronous generators and grid-forming power inverters,” tech. rep., National Renewable Energy Lab.(NREL), Golden, CO (United States), 2019.

[126] J. Nocedal and S. Wright, *Numerical optimization.* Springer Science & Business Media, 2006.

[127] G. Pannocchia and J. B. Rawlings, “Disturbance models for offset-free model-predictive control,” *AIChE journal*, vol. 49, no. 2, pp. 426–437, 2003.

[128] A. G. Phadke and B. Tianshu, “Phasor measurement units, wams, and their applications in protection and control of power systems,” *Journal of Modern Power Systems and Clean Energy*, vol. 6, no. 4, pp. 619–629, 2018.

[129] R. Ramos, I. Hiskens, *et al.*, “Benchmark systems for small-signal stability analysis and control,” *IEEE Power and Energy Society*, 2015.

[130] “Ieee/iec international standard - measuring relays and protection equipment - part 118-1: Synchrophasor for power systems - measurements,” *IEC/IEEE 60255-118-1:2018*, pp. 1–78, Dec 2018.

[131] R. Ghiga, K. Martin, Q. Wu, and A. H. Nielsen, “Phasor measurement unit test under interference conditions,” *IEEE Transactions on Power Delivery*, vol. 33, no. 2, pp. 630–639, 2017.

[132] K.-S. Shim, S.-J. Ahn, and J.-H. Choi, “Synchronization of low-frequency oscillation in power systems,” *Energies*, vol. 10, no. 4, p. 558, 2017.

[133] Y. Ma, L. Zhu, F. Wang, and L. M. Tolbert, “Enhancing power system transient stability by virtual synchronous generator control using wide-area measurements,” in *2019 IEEE Energy Conversion Congress and Exposition (ECCE)*, pp. 2546–2551, IEEE.

[134] A. Ortega, F. Milano, A. Musa, L. Toma, and D. Preotescu, “Definition of frequency under high dynamic conditions,” *RESERVE Consortium, Tech. Rep., 2017, deliverable 2.1*, 2017.

[135] E. Rakhshani and P. Rodriguez, “Inertia emulation in ac/dc interconnected power

systems using derivative technique considering frequency measurement effects," *IEEE Transactions on Power Systems*, vol. 32, no. 5, pp. 3338–3351, 2016.

[136] G. Ellis, *Observers in control systems: a practical guide*. Elsevier, 2002.

[137] G. Pannocchia and A. Bemporad, "Combined design of disturbance model and observer for offset-free model predictive control," *IEEE Transactions on Automatic Control*, vol. 52, no. 6, pp. 1048–1053, 2007.

[138] F. Borrelli and M. Morari, "Offset free model predictive control," in *2007 46th IEEE Conference on Decision and Control*, pp. 1245–1250, IEEE, 2007.

[139] E. Camponogara, D. Jia, B. H. Krogh, and S. Talukdar, "Distributed model predictive control," *IEEE control systems magazine*, vol. 22, no. 1, pp. 44–52, 2002.

[140] B. T. Stewart, A. N. Venkat, J. B. Rawlings, S. J. Wright, and G. Pannocchia, "Cooperative distributed model predictive control," *Systems & Control Letters*, vol. 59, no. 8, pp. 460–469, 2010.

[141] F. Dorfler and F. Bullo, "Synchronization and transient stability in power networks and nonuniform kuramoto oscillators," *SIAM Journal on Control and Optimization*, vol. 50, no. 3, pp. 1616–1642, 2012.

[142] L. Zhu and D. J. Hill, "Synchronization of power systems and kuramoto oscillators: A regional stability framework," *arXiv preprint arXiv:1804.01644*, 2018.

[143] G. Filatrella, A. H. Nielsen, and N. F. Pedersen, "Analysis of a power grid using a kuramoto-like model," *The European Physical Journal B*, vol. 61, no. 4, pp. 485–491, 2008.

[144] M. Pavella, D. Ernst, and D. Ruiz-Vega, *Transient stability of power systems: a unified approach to assessment and control*. Springer Science & Business Media, 2012.

[145] F. Milano and A. Ortega, "Frequency divider," *IEEE Transactions on Power Systems*, vol. 32, no. 2, pp. 1493–1501, 2016.

[146] B. Agrawal, P. Anderson, C. Concordia, R. Farmer, A. Fouad, P. Kundur, W. Price, and C. Taylor, "Damping representation for power system stability studies," *IEEE Transactions on Power Systems*, vol. 14, no. 1, pp. 151–157, 1999.

[147] PJM Learning Center, "Synchrophasors." `https://learn.pjm.com/energy-innovations/synchrophasors.aspx`. [Online; accessed 24-September-2019].

[148] S. J. Qin, "An overview of subspace identification," *Computers & chemical engineering*, vol. 30, no. 10-12, pp. 1502–1513, 2006.

[149] S. Paoletti, A. L. Juloski, G. Ferrari-Trecate, and R. Vidal, "Identification of hybrid systems a tutorial," *European journal of control*, vol. 13, no. 2-3, pp. 242–260, 2007.

[150] W. Favoreel, B. De Moor, and P. Van Overschee, "Subspace state space system identification for industrial processes," *Journal of process control*, vol. 10, no. 2-3, pp. 149–155, 2000.

[151] W. Farah, G. Mercère, and T. Poinot, "System identification and uncertainty domain determination: a subspace-based approach," in *Proceedings of the 2010 American Control Conference*, pp. 6501–6506, IEEE, 2010.

Appendix A

GAIN MATRICES AND CONSTRAINT FORMULATION

A.1 Constant Gain Matrix for IPC

The matrices $\boldsymbol{H}$ and $\boldsymbol{F}$ in 5.3.2 can be obtained as follows: writing the linear system model in (4.13) for N time steps ahead in matrix form, we have:

$$\underbrace{\begin{bmatrix} \boldsymbol{x}^0 \\ \boldsymbol{x}^1 \\ \boldsymbol{x}^2 \\ \vdots \\ \boldsymbol{x}^N \end{bmatrix}}_{\boldsymbol{x}} = \underbrace{\begin{bmatrix} 0 & 0 & \dots & 0 \\ \bar{\boldsymbol{B}} & 0 & \dots & 0 \\ \bar{\boldsymbol{A}}\bar{\boldsymbol{B}} & \bar{\boldsymbol{B}} & \dots & 0 \\ \vdots & \vdots & \ddots & \vdots \\ \bar{\boldsymbol{A}}^{N-1}\bar{\boldsymbol{B}} & \bar{\boldsymbol{A}}^{N-2}\bar{\boldsymbol{B}} & \dots & \bar{\boldsymbol{B}} \end{bmatrix}}_{\boldsymbol{S}} \underbrace{\begin{bmatrix} \boldsymbol{u}^0 \\ \boldsymbol{u}^1 \\ \vdots \\ \boldsymbol{u}^{N-1} \end{bmatrix}}_{\boldsymbol{u}} + \underbrace{\begin{bmatrix} \boldsymbol{I} \\ \bar{\boldsymbol{A}} \\ \bar{\boldsymbol{A}}^2 \\ \vdots \\ \bar{\boldsymbol{A}}^N \end{bmatrix}}_{\boldsymbol{M}} \boldsymbol{x}^0 \tag{A.1}$$

The objective function in (5.25) can then be written in terms of the state variable as:

$$\boldsymbol{y}^T\boldsymbol{Q}_1\boldsymbol{y} = (\boldsymbol{C}\boldsymbol{x})^T\boldsymbol{Q}_1(\boldsymbol{C}\boldsymbol{x}) = \boldsymbol{x}^T \underbrace{\boldsymbol{C}^T\boldsymbol{Q}_1\boldsymbol{C}}_{\hat{\boldsymbol{Q}}_1} \boldsymbol{x} \tag{A.2}$$

$$= \begin{bmatrix} \boldsymbol{x}^0 \\ \boldsymbol{x}^1 \\ \boldsymbol{x}^2 \\ \vdots \\ \boldsymbol{x}^N \end{bmatrix} \underbrace{\begin{bmatrix} \hat{\boldsymbol{Q}}_1 & 0 & 0 & \dots & 0 \\ 0 & \hat{\boldsymbol{Q}}_1 & 0 & \dots & 0 \\ 0 & 0 & \hat{\boldsymbol{Q}}_1 & \dots & 0 \\ \vdots & \vdots & \ddots & \vdots & \\ 0 & 0 & 0 & \dots & \hat{\boldsymbol{Q}}_1 \end{bmatrix}}_{\tilde{\boldsymbol{Q}}_1} \begin{bmatrix} \boldsymbol{x}^0 \\ \boldsymbol{x}^1 \\ \boldsymbol{x}^2 \\ \vdots \\ \boldsymbol{x}^N \end{bmatrix}$$

$$= (\boldsymbol{S}\boldsymbol{u} + \boldsymbol{M}\boldsymbol{x}^0)^T\tilde{\boldsymbol{Q}}_1(\boldsymbol{S}\boldsymbol{u} + \boldsymbol{M}\boldsymbol{x}^0) \tag{A.3}$$

Let

$$\begin{aligned} \boldsymbol{\Theta} &= \boldsymbol{S}[\boldsymbol{0}:\boldsymbol{N}-\boldsymbol{1};\boldsymbol{1}:\boldsymbol{N}] - \boldsymbol{S}[\boldsymbol{1}:\boldsymbol{N};\boldsymbol{1}:\boldsymbol{N}] \\ \boldsymbol{\Gamma} &= \boldsymbol{M}[\boldsymbol{0}:\boldsymbol{N}-\boldsymbol{1}] - \boldsymbol{M}[\boldsymbol{1}:\boldsymbol{N}] \\ \triangle\boldsymbol{x} &= \boldsymbol{x}[\boldsymbol{0}:\boldsymbol{N}-\boldsymbol{1}] - \boldsymbol{x}[\boldsymbol{1}:\boldsymbol{N}] \end{aligned} \tag{A.4}$$

such that

$$\begin{aligned} \triangle\boldsymbol{y}^{\boldsymbol{T}}\boldsymbol{Q}_{\boldsymbol{2}}\triangle\boldsymbol{y} &= (\boldsymbol{C}\triangle\boldsymbol{x})^{\boldsymbol{T}}\boldsymbol{Q}_{\boldsymbol{2}}(\boldsymbol{C}\triangle\boldsymbol{x}) \\ &= \triangle\boldsymbol{x}^{\boldsymbol{T}}\underbrace{\boldsymbol{C}^{\boldsymbol{T}}\boldsymbol{Q}_{\boldsymbol{2}}\boldsymbol{C}}_{\tilde{\boldsymbol{Q}}_{\boldsymbol{2}}}\triangle\boldsymbol{x} \\ &= (\boldsymbol{\Theta u}+\boldsymbol{\Gamma x^0})^{\boldsymbol{T}}\tilde{\boldsymbol{Q}}_{\boldsymbol{2}}(\boldsymbol{\Theta u}+\boldsymbol{\Gamma x^0}) \end{aligned} \tag{A.5}$$

Therefore (5.25) becomes:

$$\begin{aligned} J &= \frac{1}{2}\Big((\boldsymbol{Su}+\boldsymbol{Mx^0})^{\boldsymbol{T}}\tilde{\boldsymbol{Q}}_{\boldsymbol{1}}(\boldsymbol{Su}+\boldsymbol{Mx^0}) + (\boldsymbol{\Theta u}+\boldsymbol{\Gamma x^0})^{\boldsymbol{T}}\tilde{\boldsymbol{Q}}_{\boldsymbol{2}}(\boldsymbol{\Theta u}+\boldsymbol{\Gamma x^0})\Big) \\ &= \frac{1}{2}\boldsymbol{x^{0T}}\Big[\underbrace{\boldsymbol{M}^{\boldsymbol{T}}\tilde{\boldsymbol{Q}}_{\boldsymbol{1}}\boldsymbol{M}+\boldsymbol{\Gamma}^{\boldsymbol{T}}\tilde{\boldsymbol{Q}}_{\boldsymbol{2}}\boldsymbol{\Gamma}}_{\boldsymbol{G}}\Big]\boldsymbol{x^0} + \frac{1}{2}\boldsymbol{u}^{\boldsymbol{T}}\Big[\underbrace{\boldsymbol{S}^{\boldsymbol{T}}\tilde{\boldsymbol{Q}}_{\boldsymbol{1}}\boldsymbol{S}+\boldsymbol{\Theta}^{\boldsymbol{T}}\tilde{\boldsymbol{Q}}_{\boldsymbol{2}}\boldsymbol{\Theta}}_{\boldsymbol{H}}\Big]\boldsymbol{u} \\ &\quad + \boldsymbol{x^{0T}}\Big[\underbrace{\boldsymbol{M}^{\boldsymbol{T}}\tilde{\boldsymbol{Q}}_{\boldsymbol{1}}\boldsymbol{S}+\boldsymbol{\Gamma}^{\boldsymbol{T}}\tilde{\boldsymbol{Q}}_{\boldsymbol{2}}\boldsymbol{\Theta}}_{\boldsymbol{F}}\Big]\boldsymbol{u} \\ J &= \frac{1}{2}\boldsymbol{x^{0T}}\boldsymbol{Gx^0} + \frac{1}{2}\boldsymbol{u}^{\boldsymbol{T}}\boldsymbol{Hu} + \boldsymbol{x^{0T}}\boldsymbol{Fu} \end{aligned} \tag{A.6}$$

For optimality, $\boldsymbol{\nabla J_u} = \boldsymbol{Hu}+\boldsymbol{Fx^0} = 0$, such that the optimal control action at a given start point for N time horizon ahead becomes:

$$\boldsymbol{u}^* = -\boldsymbol{H}^{-\boldsymbol{1}}\boldsymbol{F}^{\boldsymbol{T}}\boldsymbol{x^0}. \tag{A.7}$$

A.2 Constant Gain Matrix for MIPC

The matrices $\boldsymbol{H}_{\text{mod}}$ and $\boldsymbol{F}_{\text{mod}}$ in 5.3.2 can be obtained as follows: writing the linear system model in (5.14) for N time steps ahead in matrix form, we have:

$$\underbrace{\begin{bmatrix} \hat{\boldsymbol{z}}^{0} \\ \hat{\boldsymbol{z}}^{1} \\ \hat{\boldsymbol{z}}^{2} \\ \vdots \\ \hat{\boldsymbol{z}}^{N} \end{bmatrix}}_{\hat{\boldsymbol{z}}} = \underbrace{\begin{bmatrix} \boldsymbol{0} & \boldsymbol{0} & \dots & \boldsymbol{0} \\ \boldsymbol{B} & \boldsymbol{0} & \dots & \boldsymbol{0} \\ \boldsymbol{AB} & \boldsymbol{B} & \dots & \boldsymbol{0} \\ \vdots & \vdots & \ddots & \vdots \\ \boldsymbol{A}^{N-1}\boldsymbol{B} & \boldsymbol{A}^{N-2}\boldsymbol{B} & \dots & \boldsymbol{B} \end{bmatrix}}_{\boldsymbol{S}} \underbrace{\begin{bmatrix} \boldsymbol{u}^{0} \\ \boldsymbol{u}^{1} \\ \vdots \\ \boldsymbol{u}^{N-1} \end{bmatrix}}_{\boldsymbol{u}} + \underbrace{\begin{bmatrix} \boldsymbol{I} \\ \boldsymbol{A} \\ \boldsymbol{A}^{2} \\ \vdots \\ \boldsymbol{A}^{N} \end{bmatrix}}_{\boldsymbol{M}} \hat{\boldsymbol{z}}^{0} \tag{A.8}$$

such that

$$\hat{\boldsymbol{z}}^{T}\boldsymbol{Q_R}\hat{\boldsymbol{z}} = (\boldsymbol{S}\boldsymbol{u} + \boldsymbol{M}\hat{\boldsymbol{z}}^{0})^{T}\boldsymbol{Q_R}(\boldsymbol{S}\boldsymbol{u} + \boldsymbol{M}\hat{\boldsymbol{z}}^{0}) \tag{A.9}$$

where $\boldsymbol{Q_R} = \text{blkdiag}[\hat{\boldsymbol{Q}}_{\boldsymbol{R}}]$.

Also, let

$$\begin{aligned} \boldsymbol{\Theta} &= \boldsymbol{S}[\boldsymbol{0} : \boldsymbol{N}-\boldsymbol{1}; \boldsymbol{1} : \boldsymbol{N}] - \boldsymbol{S}[\boldsymbol{1} : \boldsymbol{N}; \boldsymbol{1} : \boldsymbol{N}] \\ \boldsymbol{\Gamma} &= \boldsymbol{M}[\boldsymbol{0} : \boldsymbol{N}-\boldsymbol{1}] - \boldsymbol{M}[\boldsymbol{1} : \boldsymbol{N}] \\ \triangle\hat{\boldsymbol{z}} &= \hat{\boldsymbol{z}}[\boldsymbol{0} : \boldsymbol{N}-\boldsymbol{1}] - \hat{\boldsymbol{z}}[\boldsymbol{1} : \boldsymbol{N}] \end{aligned} \tag{A.10}$$

such that

$$\triangle\hat{\boldsymbol{z}}^{T}\hat{\boldsymbol{Q}}_{\boldsymbol{2}} \triangle \hat{\boldsymbol{z}} = (\boldsymbol{\Theta}\boldsymbol{u} + \boldsymbol{\Gamma}\hat{\boldsymbol{z}}^{0})^{T}\boldsymbol{Q}_{\boldsymbol{2}}(\boldsymbol{\Theta}\boldsymbol{u} + \boldsymbol{\Gamma}\hat{\boldsymbol{z}}^{0}) \tag{A.11}$$

Therefore (5.25) becomes:

$$\begin{aligned} J &= \frac{1}{2}\Big((\boldsymbol{Su} + \boldsymbol{M}\hat{\boldsymbol{z}}^{\boldsymbol{0}})^{\boldsymbol{T}} \boldsymbol{Q_R} (\boldsymbol{Su} + \boldsymbol{M}\hat{\boldsymbol{z}}^{\boldsymbol{0}}) + (\boldsymbol{\Theta u} + \boldsymbol{\Gamma}\hat{\boldsymbol{z}}^{\boldsymbol{0}})^{\boldsymbol{T}} \boldsymbol{Q_2} (\boldsymbol{\Theta u} + \boldsymbol{\Gamma}\hat{\boldsymbol{z}}^{\boldsymbol{0}}) + \boldsymbol{u^T R_{uu} u} \\ &\qquad + (\boldsymbol{Su} + \boldsymbol{M}\hat{\boldsymbol{z}}^{\boldsymbol{0}})^{\boldsymbol{T}} \boldsymbol{R_{zu} u} + \boldsymbol{u^T R_{uz}} (\boldsymbol{Su} + \boldsymbol{M}\hat{\boldsymbol{z}}^{\boldsymbol{0}}) \Big) \\ &= \frac{1}{2}\hat{\boldsymbol{z}}^{\boldsymbol{0T}} \Big[\underbrace{\boldsymbol{M^T Q_R M} + \boldsymbol{\Gamma^T Q_2 \Gamma}}_{\boldsymbol{G}_{\text{mod}}} \Big] \hat{\boldsymbol{z}}^{\boldsymbol{0}} + \frac{1}{2}\boldsymbol{u^T} \Big[\underbrace{\boldsymbol{S^T Q_R S} + \boldsymbol{\Theta^T Q_2 \Theta} + \boldsymbol{R_{uu}} + \boldsymbol{2S^T R_{zu}}}_{\boldsymbol{H}_{\text{mod}}} \Big] \boldsymbol{u} \\ &\qquad + \hat{\boldsymbol{z}}^{\boldsymbol{0T}} \Big[\underbrace{\boldsymbol{M^T Q_R S} + \boldsymbol{\Gamma^T Q_2 \Theta} + \boldsymbol{M^T R_{zu}}}_{\boldsymbol{F}_{\text{mod}}} \Big] \boldsymbol{u} \\ J &= \frac{1}{2}\hat{\boldsymbol{z}}^{\boldsymbol{0T}} \boldsymbol{G}_{\text{mod}} \hat{\boldsymbol{z}}^{\boldsymbol{0}} + \frac{1}{2}\boldsymbol{u^T H}_{\text{mod}} \boldsymbol{u} + \hat{\boldsymbol{z}}^{\boldsymbol{0T}} \boldsymbol{F}_{\text{mod}} \boldsymbol{u} \end{aligned} \tag{A.12}$$

For optimality, $\nabla J_u = \boldsymbol{H}_{\text{mod}}\boldsymbol{u} + \boldsymbol{F}_{\text{mod}}\hat{\boldsymbol{z}}^{\boldsymbol{0}} = 0$, such that the optimal control action at a given start point for N time horizon ahead becomes:

$$\boldsymbol{u}^{*} = -\boldsymbol{H}_{\text{mod}}^{\boldsymbol{-1}} \boldsymbol{F}_{\text{mod}}^{\boldsymbol{T}} \hat{\boldsymbol{z}}^{\boldsymbol{0}}. \tag{A.13}$$

A.3 Power Limit

The linear constraint equation for the IBR power limit in (5.29) can be derived by stacking (5.22) for a N step control horizon as follows:

$$\underbrace{\begin{bmatrix} P_{\text{ibr},k}^{1} \\ P_{\text{ibr},k}^{2} \\ \vdots \\ P_{\text{ibr},k}^{N} \end{bmatrix}}_{\boldsymbol{P}_{\text{ibr},\boldsymbol{k}}} = \underbrace{\begin{bmatrix} \boldsymbol{B_{p1}} & \boldsymbol{0} & \dots & \boldsymbol{0} \\ \boldsymbol{B_{p1}} & \boldsymbol{B_{p1}} & \dots & \boldsymbol{0} \\ \vdots & \vdots & \ddots & \vdots \\ \boldsymbol{B_{p1}} & \boldsymbol{B_{p1}} & \dots & \boldsymbol{B_{p1}} \end{bmatrix}}_{\boldsymbol{B_{p1,N}}} \underbrace{\begin{bmatrix} \hat{\boldsymbol{z}}^{\boldsymbol{1}} \\ \hat{\boldsymbol{z}}^{\boldsymbol{2}} \\ \vdots \\ \hat{\boldsymbol{z}}^{\boldsymbol{N}} \end{bmatrix}}_{\hat{\boldsymbol{z}}} + \underbrace{\begin{bmatrix} \boldsymbol{B_{p2}} & \boldsymbol{0} & \dots & \boldsymbol{0} \\ \boldsymbol{B_{p2}} & \boldsymbol{B_{p2}} & \dots & \boldsymbol{0} \\ \vdots & \vdots & \ddots & \vdots \\ \boldsymbol{B_{p2}} & \boldsymbol{B_{p2}} & \dots & \boldsymbol{B_{p2}} \end{bmatrix}}_{\boldsymbol{B_{p2,N}}} \underbrace{\begin{bmatrix} \boldsymbol{u^0} \\ \boldsymbol{u^1} \\ \vdots \\ \boldsymbol{u^{N-1}} \end{bmatrix}}_{\boldsymbol{u}} . \tag{A.14}$$

From (A.8), we have that $\hat{\boldsymbol{z}} = \boldsymbol{Su} + \boldsymbol{M}\hat{\boldsymbol{z}}^{\boldsymbol{0}}$, therefore (A.14) becomes,

$$\begin{aligned} \boldsymbol{P}_{\text{ibr},\boldsymbol{k}} &= \boldsymbol{B_{p1,N} S u} + \boldsymbol{B_{p1,N} M}\hat{\boldsymbol{z}}^{\boldsymbol{0}} + \boldsymbol{B_{p2,N} u} \\ &= \underbrace{(\boldsymbol{B_{p1,N} S} + \boldsymbol{B_{p2,N}})}_{\tilde{\boldsymbol{B}}_{\boldsymbol{p1}}} \boldsymbol{u} + \underbrace{\boldsymbol{B_{p1,N} M}}_{\tilde{\boldsymbol{B}}_{\boldsymbol{p2}}} \hat{\boldsymbol{z}}^{\boldsymbol{0}}. \end{aligned} \tag{A.15}$$

The lower power limit can then be written as

$$-\tilde{\boldsymbol{B}}_{\boldsymbol{p1}}\boldsymbol{u} \leq -\tilde{\boldsymbol{P}}_{\text{ibr, min}} + \tilde{\boldsymbol{B}}_{\boldsymbol{p2}}\hat{\boldsymbol{z}}^{\boldsymbol{0}} \tag{A.16}$$

and the upper power limit as

$$\tilde{\boldsymbol{B}}_{\boldsymbol{p1}}\boldsymbol{u} \leq \tilde{\boldsymbol{P}}_{\text{ibr, min}} - \tilde{\boldsymbol{B}}_{\boldsymbol{p2}}\hat{\boldsymbol{z}}^{\boldsymbol{0}} \tag{A.17}$$

resulting in a combined form of:

$$\underbrace{\begin{bmatrix} -\tilde{\boldsymbol{B}}_{\text{p2}} \\ \tilde{\boldsymbol{B}}_{\text{p2}} \end{bmatrix}}_{\boldsymbol{L}} \boldsymbol{u} \leq \underbrace{\begin{bmatrix} -\tilde{\boldsymbol{P}}_{\text{ibr, min}} \\ \tilde{\boldsymbol{P}}_{\text{ibr, max}} \end{bmatrix}}_{\boldsymbol{W}} + \underbrace{\begin{bmatrix} \tilde{\boldsymbol{B}}_{\text{p1}} \\ -\tilde{\boldsymbol{B}}_{\text{p1}} \end{bmatrix}}_{\boldsymbol{V}} \hat{\boldsymbol{z}}^{\boldsymbol{0}}\textbf{.} \tag{A.18}$$

where $\tilde{\boldsymbol{P}}_{\text{ibr, min}}$ and $\tilde{\boldsymbol{P}}_{\text{ibr, max}}$ are matrices of $\tilde{\boldsymbol{P}}^{\boldsymbol{t}}_{\text{ibr, min}}$ and $\tilde{\boldsymbol{P}}^{\boldsymbol{t}}_{\text{ibr, max}}$ stacked together for N horizon.

A.4 Total Energy Limit

The linear constraint equation for the IBR power limit in (5.30) can be derived from the power limit in (A.15) by taking the rolling sum such that:

$$[\tilde{\boldsymbol{B}}_{\text{p1}}\boldsymbol{u} + \tilde{\boldsymbol{B}}_{\text{p2}}\hat{\boldsymbol{z}}^{\boldsymbol{0}}]^{\boldsymbol{T}}\boldsymbol{1}_{\boldsymbol{N}} \leq \tilde{\boldsymbol{E}}_{\text{ibr, tot}} \tag{A.19}$$

resulting in

$$\underbrace{\boldsymbol{1}_{\boldsymbol{N}}^{\boldsymbol{T}}\tilde{\boldsymbol{B}}_{\text{p1}}}_{\tilde{\boldsymbol{B}}_{\text{e1}}}\boldsymbol{u} \leq \tilde{\boldsymbol{E}}_{\text{ibr, tot}} - \underbrace{\boldsymbol{1}_{\boldsymbol{N}}^{\boldsymbol{T}}\tilde{\boldsymbol{B}}_{\text{p2}}}_{\tilde{\boldsymbol{B}}_{\text{e2}}}\hat{\boldsymbol{z}}^{\boldsymbol{0}}\textbf{.} \tag{A.20}$$

The rate limit, represented as ϵ in this work, can be incorporated by taking the difference between time steps of the output power in (A.15) such that:

$$[\tilde{\boldsymbol{B}}_{\text{p1}}\boldsymbol{u} + \tilde{\boldsymbol{B}}_{\text{p2}}\hat{\boldsymbol{z}}^{\boldsymbol{0}}]_{[\boldsymbol{1}:\boldsymbol{N}-\boldsymbol{1}]} - [\tilde{\boldsymbol{B}}_{\text{p1}}\boldsymbol{u} + \tilde{\boldsymbol{B}}_{\text{p2}}\hat{\boldsymbol{z}}^{\boldsymbol{0}}]_{[\boldsymbol{2}:\boldsymbol{N}]} \tag{A.21}$$

resulting in

$$\tilde{\boldsymbol{B}}_{\text{p1}}\boldsymbol{u} + \tilde{\boldsymbol{B}}_{\text{p2}}\hat{\boldsymbol{z}}^{\boldsymbol{0}}]_{[\boldsymbol{1}:\boldsymbol{N}-\boldsymbol{1}]} - [\tilde{\boldsymbol{B}}_{\text{p1}}\boldsymbol{u} + \tilde{\boldsymbol{B}}_{\text{p2}}\hat{\boldsymbol{z}}^{\boldsymbol{0}}]_{[\boldsymbol{2}:\boldsymbol{N}]} \tag{A.22}$$

The combined form of these two constraints is:

$$\underbrace{\begin{bmatrix} \tilde{\boldsymbol{B}}_{\text{e2}} \\ \tilde{\boldsymbol{B}}_{\text{r2}} \end{bmatrix}}_{\boldsymbol{L}} \boldsymbol{u} \leq \underbrace{\begin{bmatrix} \tilde{\boldsymbol{E}}_{\text{ibr, tot}} \\ \boldsymbol{\epsilon} \end{bmatrix}}_{\boldsymbol{W}} + \underbrace{\begin{bmatrix} -\tilde{\boldsymbol{B}}_{\text{e1}} \\ -\tilde{\boldsymbol{B}}_{\text{r1}} \end{bmatrix}}_{\boldsymbol{V}} \hat{\boldsymbol{z}}^{\boldsymbol{0}}. \tag{A.23}$$

Appendix B

MODELS

B.1 Droop Equation

B.1.1 Continuous Time Form

$$\triangle P_{m,i} = \left(- \triangle \omega_i - R \triangle P_{m,i}\right) \frac{K}{s} \tag{B.1}$$

$$\triangle \dot{P}_{m,i} = -K \triangle \omega_i - KR \triangle P_{m,i} \tag{B.2}$$

Let $\tau_g = \frac{1}{KR} \implies K = \frac{1}{\tau_g R} = \frac{K_d}{\tau_g}$ where $K_d = \frac{1}{R}$

$$\triangle \dot{P}_{m,i} = -K \triangle \omega_i - \frac{\triangle P_{m,i}}{\tau_g} \tag{B.3}$$

$$\triangle \dot{P}_{m,i} = -\frac{K_d}{\tau_g} \triangle \omega_i - \frac{\triangle P_{m,i}}{\tau_g} \tag{B.4}$$

Let

$$k_1 = \frac{1}{\tau_g} \qquad and \qquad k_2 = \frac{K_d}{\tau_g} \tag{B.5}$$

Then

$$\triangle \dot{P}_{m,i} = -k1 \triangle P_{m,i} - k2 \triangle \omega_i \tag{B.6}$$

B.1.2 Discrete Time Form

From (B.6)

$$\triangle P_{m,i}^{t+1} = \triangle P_{m,i}^{t} - h \left(k1 \triangle P_{m,i}^{t} + k2 \triangle \omega_i^t\right) \tag{B.7}$$

B.2 Automatic Governor Control (AGC) Equation

B.2.1 Continuous Time Form

$$ACE = \triangle P_{tie} + B \triangle \omega \tag{B.8}$$

$$\triangle P_m = \left[\frac{K}{s} ACE - \frac{1}{R} \triangle \omega\right] \frac{1}{1 + s\tau_g} \tag{B.9}$$

$$\triangle P_m = -\frac{K}{s} ACE \left[\frac{1}{1 + s\tau_g}\right] - K_d \triangle \omega \left[\frac{1}{1 + s\tau_g}\right] \tag{B.10}$$

$$\triangle P_m = -\frac{K}{s + s^2\tau_g} ACE - \frac{K_d}{1 + s\tau_g} \triangle \omega \tag{B.11}$$

$$(s + s^2\tau_g) \triangle P_m = -K\ ACE - K_d s \triangle \omega \tag{B.12}$$

$$s \triangle P_m + s^2\tau_g \triangle P_m = -K\ ACE - K_d s \triangle \omega \tag{B.13}$$

$$\tau_g \triangle \ddot{P}_m = - \triangle \dot{P}_m - K[\triangle P_{tie} + B \triangle \omega] - K_d \triangle \dot{\omega} \tag{B.14}$$

$$\triangle \ddot{P}_{m,i} = -\frac{\triangle \dot{P}_{m,i}}{\tau_g} - \frac{K \triangle P_{tie}}{\tau_g} - \frac{KB \triangle \omega_i}{\tau_g} - \frac{K_d \dot{\triangle \omega_i}}{\tau_g} \tag{B.15}$$

Let

$$k_1 = \frac{1}{\tau_g}, \qquad k_2 = \frac{K_d}{\tau_g}, \qquad k3 = \frac{KB}{\tau_g}, and \qquad k4 = \frac{k3}{B} \tag{B.16}$$

Then

$$\triangle \ddot{P}_{m,i} = -k1 \triangle \dot{P}_{m,i} - k2 \triangle \dot{\omega}_i - k3 \triangle \omega_i - k4 \triangle P_{tie} \tag{B.17}$$

From swing equation:

$$\triangle \dot{\omega}_i = \frac{1}{m_i} \left(P_{m,i} - P_{e,i} - d_i \triangle \omega_i\right) \tag{B.18}$$

$$\dot{\delta}_i = \omega_i - \omega_s = \triangle \omega_i$$

Substituting (B.17) with $\triangle\dot{\omega}_i$ from (B.18) results in:

$$\triangle\ddot{P}_{m,i} = -k1 \triangle \dot{P}_{m,i} - \frac{k2}{m_i}\left(\triangle P_{m,i} - \triangle P_{e,i} - \triangle P_{l,i} - d_i \triangle \omega_i\right) - k3 \triangle \omega_i - k4 \triangle P_{tie} \tag{B.19}$$

$$\triangle\ddot{P}_{m,i} = -k1 \triangle \dot{P}_{m,i} - \frac{k_2}{m_i}\left(\triangle P_{m,i} - \triangle P_{e,i} - \triangle P_{l,i}\right) + \left(\frac{k_2 d_i}{m_i} - k3\right) \triangle \omega_i - k4 \triangle P_{tie} \tag{B.20}$$

Since tie-line power is not considered in this scenario, $\triangle P_{tie} = 0$, such that:

$$\triangle\ddot{P}_{m,i} = -k1 \triangle \dot{P}_{m,i} - \frac{k_2}{m_i}\left(\triangle P_{m,i} - \triangle P_{e,i} - \triangle P_{l,i}\right) + \left(\frac{k_2 d_i}{m_i} - k3\right) \triangle \omega_i \tag{B.21}$$

B.2.2 Discrete Time Form

From (B.21), using 2^{nd} order forward difference for $\triangle\ddot{P}_{m,i}$ and 1^{st} order forward difference for $\triangle\dot{P}_{m,i}$, we have that:

$$\triangle\ddot{P}_{m,i} \approx \frac{\triangle P_{m,i}^{t+1} - 2 \triangle P_{m,i}^{t} + \triangle P_{m,i}^{t-1}}{h^2} \tag{B.22}$$

and

$$\triangle\dot{P}_{m,i} \approx \frac{\triangle P_{m,i}^{t+1} - \triangle P_{m,i}^{t}}{h} \tag{B.23}$$

Therefore:

$$\frac{\triangle P_{m,i}^{t+1} - 2 \triangle P_{m,i}^{t} + \triangle P_{m,i}^{t-1}}{h^2} = -k1\left(\frac{\triangle P_{m,i}^{t+1} - \triangle P_{m,i}^{t}}{h}\right) - \frac{k_2}{m_i} \triangle P_{m,i}^{t} + \left[-\frac{k_2}{m_i}\left(- \triangle P_{e,i}^{t} - \triangle P_{l,i}^{t}\right) + \left(\frac{k_2 d_i}{m_i} - k3\right) \triangle \omega_i^t\right] \tag{B.24}$$

$$\triangle P_{m,i}^{t+1} = 2 \triangle P_{m,i}^{t} - \triangle P_{m,i}^{t-1} - h^2 k1\left(\frac{\triangle P_{m,i}^{t+1} - \triangle P_{m,i}^{t}}{h}\right) - \frac{h^2 k_2}{m_i} \triangle P_{m,i}^{t} + h^2\left[-\frac{k_2}{m_i}\left(- \triangle P_{e,i}^{t} - \triangle P_{l,i}^{t}\right) + \left(\frac{k_2 d_i}{m_i} - k3\right) \triangle \omega_i^t\right] \tag{B.25}$$

$$\triangle P_{m,i}^{t+1} = 2 \triangle P_{m,i}^{t} - \triangle P_{m,i}^{t-1} - hk1 \triangle P_{m,i}^{t+1} + hk1 \triangle P_{m,i}^{t} - h^2 \frac{k_2}{m_i} \triangle P_{m,i}^{t} + h^2\left[-\frac{k_2}{m_i}\left(- \triangle P_{e,i}^{t} - \triangle P_{l,i}^{t}\right) + \left(\frac{k_2 d_i}{m_i} - k3\right) \triangle \omega_i^t\right] \tag{B.26}$$

$$(1+hk1)\triangle P_{m,i}^{t+1} = \left[2+hk1-\frac{h^2k_2}{m_i}\right]\triangle P_{m,i}^{t} - \triangle P_{m,i}^{t-1} + \tag{B.27}$$

$$h^2\left[-\frac{k_2}{m_i}\left(-\triangle P_{e,i}^{t} - \triangle P_{l,i}^{t}\right) + \left(\frac{k_2 d_i}{m_i} - k3\right)\triangle \omega_i^{t}\right]$$

$$\triangle P_{m,i}^{t+1} = \frac{\left[2+hk1-\frac{h^2k_2}{m_i}\right]\triangle P_{m,i}^{t} - \triangle P_{m,i}^{t-1} + h^2\left[-\frac{k_2}{m_i}\left(-\triangle P_{e,i}^{t} - \triangle P_{l,i}^{t}\right) + \left(\frac{k_2 d_i}{m_i} - k3\right)\triangle \omega_i^{t}\right]}{1+hk1} \tag{B.28}$$

$$\triangle P_{m,i}^{t+1} = \frac{\left[2+hk1-\frac{h^2k_2}{m_i}\right]\triangle P_{m,i}^{t} - \triangle P_{m,i}^{t-1} + h^2\left[\left(\frac{k_2 d_i}{m_i} - k3\right)\triangle \omega_i^{t} - \frac{k_2}{m_i}\left(\triangle P_{e,i}^{t} + \triangle P_{l,i}^{t}\right)\right]}{1+hk1} \tag{B.29}$$